Metastability, Resets and Large Deviations in Open Quantum Systems

Dominic Charles Rose

A thesis presented for the degree of
Doctor of Philosophy



School of Physics and Astronomy
University of Nottingham
United Kingdom

April 2019

Abstract

In this thesis we apply, and build upon, a comprehensive theory of metastability in open quantum systems. We gain a full understanding of the long time states and the dynamics between them in a 1D open quantum Ising model, and a glassy, dissipative quantum East model: in order to do this, we develop algorithmic approaches to conducting such analyses in generic models exhibiting a metastability which can be considered classical. In addition, we provide an extensive discussion of the use of symmetries in the numerical study of open quantum systems, containing results of substantial use throughout this work. We finish with a general set of results about the spectra of operators describing the evolution of classical or quantum models undergoing stochastic resetting, allowing a precise analysis of the effect of resets on metastability in the 1D open quantum Ising model.

List of Publications

This thesis contains work which has been the subject of several manuscripts either published or in preparation. Here, we list these and the chapters with which they are associated.

Chapter 3:

1. *Weak unitary symmetries of the Lindblad equations simplify quantum trajectories*, Katarzyna Macieszczak, **Dominic C. Rose**, in preparation.

Chapter 4:

2. *Metastability in an open quantum Ising model*, **Dominic C. Rose**, Katarzyna Macieszczak, Igor Lesanovsky, Juan P. Garrahan, Phys. Rev. E 94, 052132 (2016).

3. *Phase transitions in electron spin resonance under continuous microwave driving*, Alexander Karabanov, **Dominic C. Rose**, Walter Köckenberger, Juan P. Garrahan, Igor Lesanovsky, Phys. Rev. Lett. 119, 150402 (2017).

Chapter 5:

4. *Classical metastability in open quantum systems*, **Dominic C. Rose**, Katarzyna Macieszczak, Igor Lesanovsky, Juan P. Garrahan, in preparation.

Chapter 6:

5. *Spectral properties of simplex classical and quantum reset processes*, **Dominic C. Rose**, Hugo Touchette, Igor Lesanovsky, Juan P. Garrahan, Phys. Rev. E 98, 022129 (2018).

To Mum and Dad

Acknowledgements

I would like to thank my supervisors, Juan Garrahan and Igor Lesanovsky, for their extensive guidance and suggestions over the years, both in research and for other aspects of academia; and Katarzyna Macieszczak, for working with me on much of the research presented in this thesis. I would also like to thank Hugo Touchette for hosting me during a visit to Stellenbosch, South Africa, and for his many great suggestions while we collaborated on a project together.

To the PhD students of the condensed matter theory group at Nottingham, I'm grateful for your friendship and support throughout the years; in particular, I would like to mention Tom Oakes, Claire Davis-Tilley and Ben Everest for the guidance they gave me at the beginning of my PhD. For the humour they brought to the later years of my time in Nottingham, and for their help proof reading this thesis, I thank Federica Raimondi, Jemma Needham, Matt Jessop, Maike Ostmann, Gary McCormack, William Morley, Joe Wilkinson, and Ciarán McDonnell.

Finally, to my parents Jayne and Tom Rose: without your support over the years, I would never have made it to where I am today. I love you both, and thank you for everything.

Contents

1 Introduction **1**

2 Theoretical background **4**

2.1 Classical jump processes 4

2.1.1 Spectral theory of stochastic generators 6

2.1.2 Trajectories and Monte Carlo methods 8

2.1.3 Stochastic metastability and the Ising model 10

2.2 Open quantum systems 15

2.2.1 The Lindblad equation 16

2.2.2 Quantum jump Monte Carlo 19

3 Weak symmetries in open quantum systems **24**

3.1 Weak and strong symmetries 25

3.1.1 Discrete symmetries 26

3.1.2 Continuous symmetries 29

3.1.3 Uses of strong symmetries 29

3.2 Weakly symmetric representations 30

3.2.1 Example 1: discrete translations 31

3.2.2 Example 2: spin rotations 31

3.3 Block diagonalizing the Lindblad operator 32

3.4 Symmetry enhanced quantum jump Monte Carlo 34

4 Metastability in an open quantum Ising model **37**

4.1 Metastable manifolds and effective evolution 40

4.1.1 Metastable manifold 41

4.1.2 Effective dynamics within metastable manifold 42

4.1.3 Observation of metastability 42

4.2 Open quantum Ising model 43

4.2.1 Time dependent mean-field approximation 44

4.2.2 Spectral analysis of the master operator 47
4.2.3 Characterization of the metastable manifold 48
4.2.4 Expectations, correlations and effective low-dimensional dynamics 50
4.2.5 Intermittent dynamics of quantum trajectories 52
4.3 An aside: phases of dynamical nuclear polarization 56
4.3.1 Model 57
4.3.2 Fluctuations in numerical simulations 58
4.4 Summary 61

5 Classical metastable manifolds in open quantum systems 63
5.1 Classical metastable manifolds 66
5.1.1 Constructing classical manifolds 67
5.1.2 Disjointness of metastable phases in classical MM 76
5.1.3 Effective classical dynamics and intermittence 77
5.2 Dissipative quantum East model 80
5.2.1 Accuracy of the simplex approximation 84
5.2.2 Metastable phases 86
5.2.3 Effective dynamics and comparison to the classical East model 89
5.2.4 Effective lifetimes and dynamical heterogeneity 93
5.3 Thermodynamics of trajectories 99
5.4 Summary 104

6 Spectral properties of classical and quantum reset processes 106
6.1 Classical reset Markov processes 108
6.1.1 Eigenvalues and eigenvectors 108
6.1.2 Stationary state 109
6.1.3 Stationary current 110
6.1.4 Metastability 111
6.2 Classical applications 113
6.2.1 Totally asymmetric random walk 113
6.2.2 Brownian motion 115
6.3 Open quantum systems with resets 116
6.3.1 Coherent hopping on a chain 118
6.3.2 Open quantum Ising model 120
6.4 Summary 123

7 Conclusion **124**

Chapter 1

Introduction

Scale is a ubiquitous concept in physics. Commonly associated with the spatial distances we are considering, from quantum field theories for microscopic physics, up to general relativity for cosmology, scale plays an equally important role temporally. The existence of processes occuring on distinct time-scales is a basic assumption in many areas of science, allowing approximations that hide so-called "fast" dynamics, in order to focus on the effects of dominant "slow" dynamics relevant to the problem we wish to consider. These slower processes may be obvious, for example, a weak interaction between two systems with strong internal interactions; they may also be emergent, a result of the collective behaviour of a system composed of many individual elements. Exploring new avenues leading to this second, non-trivial situation acts as the focus of this thesis.

Emergence of separate epochs in a systems evolution is associated with the existence of states, or regions of states, which remain stable for long periods of time: one can imagine snow landing on the top of a mountain, where it remains until a perturbation triggers an avalanche. Such states, refered to as metastable, are often present in models of many-body physics. A prototypical example is that of the 2D Ising model, where interactions cause areas of aligned spins to become extremely long lived at low temperatures. Metastability is deeply understood in this classical context, with its mathematical origin and tools for its analysis provided by a well established theory [1]. Recently, an adaptation of this approach to the quantum regime has given insights into emergent time-scales in open systems: those influenced by interactions with an external environment [2].

Initially applied to small systems where metastability was a result of clear,

weak processes in the evolution, an analysis of time-scales emerging as a result of collective dynamics remained open. We provide the first such study in Chap. 4, an open quantum version of the 1D Ising model [3]: here, metastable states resulted from competition between an applied magnetic field and nearest neighbour couplings, each favouring states whose stabilities were amplified by distinct environmental interactions [4]. Analysing this model required the use of symmetry properties to extend numerical limitations. While symmetries are common in open classical or quantum systems, they possess some subtleties when compared with closed cases: for example, the presence of a symmetry need not imply the existence of a conserved quantity. Numerical application of symmetries in this context thus require modifications of the approaches used in closed systems, which we discuss in Chap. 3.

A symmetry based approach again proved vital in developing techniques for understanding metastability in a much more complex situation, an open quantum generalization of a classical glass model [5]. Glasses provide the most extreme example of non-trivial emergent time-scales, with the lifetimes of metastable states at low temperatures stretching beyond the lifetime of the universe. Metastability is thus no surprise in a quantum extension of glassy physics; the particular model we consider consists of spins evolving according to a uniform, "kinetically constrained" dynamics. These constraints cause isolated, excited spins to live for extended times, providing a large number of metastable states related by translations, one for each site. A comprehensive numerical approach to constructing metastable states, and checking their accuracy, in models with a complex long-time dynamics such as this, are discussed in Chap. 5, with and without symmetries. This is accompanied by an extensive analysis of the resulting states for our example glassy system, demonstrating how these techniques may be used to gain a strong understanding of the long-time dynamics for a given metastable model.

When a system with multiple metastable states is viewed on large time-scales, the evolution will consist of periods in which the state will remain within individual metastable regions, interspersed by sharp transitions between them. This intermittence results in a large, non-trivial variance in the value of observables integrated over long, but finite, times: statistical results in such situations are the realm of large deviation theory [6]. In Chap. 5, we expose the connection between large deviations and metastability in open quantum systems explicitly, demonstrating the potential for studying metastability in

these models through the use of path sampling techniques [7, 8].

We finish by considering how systems with metastability behave under the effect of resets: transitions from any state to a specific state, occurring at random times. Unsurprisingly, resets which happen infrequently enough for the metastable dynamics to be distinguishable between them leave the system metastable, but bias the stationary state towards the metastable phase which the reset state relaxes to. This is shown very precisely as a consequence of a much more surprising result: a completely general and exact relation between the spectral properties of the master operators representing a model with, and without, resets. Moreover, this result applies both to generic classical stochastic processes, and arbitrary open quantum systems. We derive the spectral relationship and discuss several results which follow in Chap. 6, demonstrating its application to a variety of classical and quantum models, including the metastable Ising model of Chap. 4.

Chapter 2

Theoretical background

In this section we introduce the theoretical background common among later chapters, beginning with an introduction to classical jump processes in Sec. 2.1. This provides an opportune setting to introduce a central concept of our work, metastability, in a more intuitive setting; namely the thermal dynamics of the 2D Ising model near a transition. While classical processes are only directly relevant to Chap. 6, these provide a useful stepping stone towards open quantum systems, where a decomposition of the dynamics into deterministic coherent evolution separated by dissipative jumps occurs naturally.

The concept of open quantum systems is introduced in Sec. 2.2, from the perspective of reducing a system-environment model to a description of the system we are interested in. A commonly occurring form of evolution resulting from this reduction, the Lindblad master equation, is then introduced as the only possible equation possessing several desirable mathematical properties. This exact description can be limiting computationally for large Hilbert space dimensions, so we conclude this section by introducing quantum jump Monte Carlo simulations, which provide both a useful intuitive picture and a powerful dimensional reduction for numerical studies.

2.1 Classical jump processes

We begin by describing a classical jump process evolving according to a continuous-time Markov chain. Such processes are necessary for the study of stochastic evolution in systems with discrete state spaces, for example in thermal dynamics of Ising spin models, but can also be relevant for dynamics in continuous state spaces. Put simply, a jump refers to a substantial random

change to the system's state which happens infrequently. This stands in contrast to diffusion, where the random changes to the state are small relative to length-scales of interest, but constantly occurring.

We refer to the literature for a first principles derivation from the Markovian property [9] (i.e. the Chapman-Kolmogorov equation), introducing this class of models through the resulting master equation. We additionally focus on discrete spaces for clarity, however the equations below can be adapted to the continuous case by replacing probability distributions with densities and sums by integrals. The evolution of the probability $P(C,t)$ for the process to be in the state or configuration C at time t is thus given by

$$\partial_t P(C,t) = \sum_{C' \neq C} W(C' \to C) P(C',t) - R(C) P(C,t), \tag{2.1}$$

where $W(C' \to C)$ is the transition rate from C' to C and

$$R(C) = \sum_{C' \neq C} W(C \to C') \tag{2.2}$$

is the escape rate from C. Following the notation commonly used in physics [10], this can be written more compactly as

$$\partial_t \left| P(t) \right\rangle = \mathcal{L} \left| P(t) \right\rangle, \tag{2.3}$$

where

$$\left| P(t) \right\rangle = \sum_C P(C,t) \left| C \right\rangle \tag{2.4}$$

is the probability vector expressed in terms of ket states $|C\rangle$, such that $\langle C|C'\rangle = \delta_{CC'}$, and

$$\mathcal{L} = \sum_{C,C' \neq C} W(C \to C') \left| C' \right\rangle \left\langle C \right| - \sum_C R(C) \left| C \right\rangle \left\langle C \right| \tag{2.5}$$

is the master operator, the generator of time evolution in the space of probability distributions. Since Eq. (2.3) is linear in the probability distribution we may write the time evolved probability distribution as

$$\left| P(t + \Delta t) \right\rangle = e^{\Delta t \mathcal{L}} \left| P(t) \right\rangle. \tag{2.6}$$

An additional piece of notation we will make regular use of is the so called flat state

$$\langle - | = \sum_c \langle C | . \tag{2.7}$$

The action of this dual vector is the 1-norm, $\langle -|V\rangle = ||V||_1$, and provides a simple way of expressing probability normalization, $\langle -|P\rangle = 1$.

Using the definition of the escape rate in Eq. (2.2) we see that $\langle -|\,\mathcal{L} = 0$. This is the operator representation of probability conservation, as it implies

$$\langle -|P(t+\Delta t)\rangle = \langle -|P(t)\rangle\,. \tag{2.8}$$

From the perspective of linear algebra this also shows us that the flat state is a left eigenvector of the master operator with eigenvalue 0. Much of our later work will involve studying the spectra of master operators, so we take the time now to discuss this in more detail.

2.1.1 Spectral theory of stochastic generators

In general, the master operator of a stochastic process is non-Hermitian, making it more difficult to handle than the Hamiltonians considered in closed quantum systems. Despite this, there is enough structure to stochastic generators for several useful results to hold generically for their spectra.

A general non-hermitian operator need not be fully diagonalizable: instead, it may only being reducible to a Jordan normal form in a basis of generalized eigenvectors. For our later purposes it is sufficient to assume Jordan blocks are not present, so we simply consider two sets of eigenvectors, right and left, given by

$$\mathcal{L}\,|r_i\rangle = \lambda_i\,|r_i\rangle\,, \tag{2.9}$$

and

$$\langle l_i|\,\mathcal{L} = \lambda_i\,\langle l_i|\,, \tag{2.10}$$

respectively. Here eigenvectors with the same index i share their eigenvalue λ_i. These two sets of eigenvectors form a complete basis, are dual to each other, and can be normalised in a such a way that $\langle l_i|r_j\rangle = \delta_{ij}$.

Any vector can be expanded in a basis of either the left or right eigenmodes, for example

$$|P\rangle = \sum_i \langle l_i|P\rangle\,|r_i\rangle\,. \tag{2.11}$$

The time evolution can then be expanded as

$$|P(t+\Delta t)\rangle = \sum_i \langle l_i|P(t)\rangle\,e^{\Delta t\lambda_i}\,|r_i\rangle\,. \tag{2.12}$$

The general properties of stochastic generators relevant to their spectra are as follows

1. The sum of each column is equal to 0.

2. All off-diagonal elements are non-negative real numbers.

3. All diagonal elements are negative real numbers (implied by 1 and 2).

As discussed in the previous section, property 1 corresponds to probability conservation, implying the existence of at least one left eigenvector with eigenvalue 0, the flat state $\langle -|$.

The first significant result for the spectrum follows from the Gershgorin circle theorem [11], which combined with the above properties implies that all eigenvalues of stochastic generators must have a non-positive real part. This indicates that all coefficients in Eq. (2.12) either decay or remain constant.

Secondly, the exponent of a matrix with these properties has non-negative elements, which combined with probability conservation implies the evolution necessarily maps probability distributions to probability distributions. Since the space of probability distributions is convex, the Brouwer fixed point theorem thus implies the matrix exponential has at least one stationary probability distribution with eigenvalue 1. We label this vector $|P_{\text{ss}}\rangle$.

As this is true for all magnitudes of time evolution, linearisation thus implies that this stationary state must also be an eigenvector of the generator with eigenvalue 0. Further, since $\langle -|P_{\text{ss}}\rangle = 1$, orthogonality of the left and right basis implies all other right eigenvectors must have zero 1-norm, i.e. they don't contribute to probability normalization.

We thus gain an interpretation of right eigenmodes aside from $|P_{\text{ss}}\rangle$ as dynamical modes which contribute to modifying the probability distribution, without changing its norm, encoding a memory of the initial probability distribution. These modifications then either decay at late times ($\text{Re}(\lambda_i) < 0$) or contribute to an initial state dependent stationary distribution at infinite time ($\text{Re}(\lambda_i) = 0$). The time-scales on which these decaying modes are relevant is given by their lifetime $\tau_i = 1/|\text{Re}(\lambda_i)|$, with the largest of these scales being referred to as the relaxation time.

The stochastic generator may be a reducible matrix (equivalently, the Markov chain may be reducible), in which case the $\lambda_i = 0$ eigenspace may be degenerate. If irreducible, there is a guaranteed unique stationary state, and the above results follow from the Perron-Frobenius theorem [12].

2.1.2 Trajectories and Monte Carlo methods

While the spectrum of a stochastic generator contains information which answers many questions about the stationary states and dynamics of a given model, it is often inaccessible to analytical or numerical study in regimes of interest. A prime example is many-body problems, where a system composed of many identical subsystems results in configuration space exponentially large in the number of subsystems. Even if some or all of the spectrum is accessible in such a problem, a great deal of intuition can be gained from a consideration of the individual trajectories of the system's evolution: it is thus desirable to have a way of generating trajectories. This generation is often achieved through the use of methods based on random numbers, compared to conditional probabilities calculated from the model, allowing generation of the stochastic changes comprising a trajectory.

The class of models introduced at the start of this section describe the evolution of a system against continuous time; jumps occur instantaneously after varying periods of time. One standard algorithm to simulate classical continuous time systems, commonly referred to as kinetic Monte Carlo, bares a strong similarity to the approach we will use for simulating open quantum systems discussed in Sec. 2.2.2. We introduce this algorithm here as a stepping stone towards that discussion.

Kinetic Monte Carlo splits the evolution into two steps: first, the time at which the next jump occurs is determined by comparing a random number with the probability distribution $P_C(t) = R(C)e^{-tR(C)}$, depending on the current configuration; secondly, the new configuration is determined by comparing another random number to a partitioning of the interval $[0, 1]$, given by $W(C \to C')/R(C)$. This approach can be seen to replicate the dynamics of the master equation by considering all trajectories of a given length T generated from configurations sampled from some initial distribution. The total probability for states at the ends of these trajectories are given by sums over the probabilities of all trajectories ending in those states: the corresponding distribution then takes the form of a Dyson series for the evolution operator over a time T with respect to its off-diagonal elements (the transitions), acting on the initial distribution.

The above procedure describes a so-called rejection free algorithm, where a change of configuration occurs whenever the time is updated. However, determining both the change in time and configuration relies on the ability to

calculate the escape rate every update: if there are too many configurations to store – or too many distinct transition rates to efficiently calculate – the escape rate at each step, this process can become infeasible. Requiring the precise value of the escape rate (or other normalizing factors) can be avoided through the use of algorithms that incorporate rejection. These methods rely on generating changes of time and configuration without consideration of the probabilities defining the system of interest: the correct statistical distributions are reproduced by appropriate chances of accepting or rejecting the proposed change. For example, acceptance can usually be related to a comparison of probabilities or rates, evading the need to normalize the distributions, as we will see next.

In the next section we introduce the concept of metastability, central to much of our work, using dynamics generated by a rejection based approach – the Metropolis-Hastings algorithm – as an example. Here an artificial discrete time evolution is constructed to sample a chosen probability distribution $P(C)$, guaranteed by changing configuration in a way that satisfies detailed balance; that is, $P(C'|C)P(C) = P(C|C')P(C')$, ensuring $P(C)$ is the stationary state of the dynamics defined by $P(C'|C)$.

A step begins by generating a new configuration C' from the current configuration C with generation probability $G(C'|C)$. In principle, if this probability satisfies detailed balance, we may simply run a simulation generating changes according to this distribution; in practice, such a generator would be difficult to find and may provide poor sampling of the configuration space. For the general case we must therefore correct this generating probability by accepting the generated configuration according to an acceptance rate $A(C'|C)$, such that the combined transition probability $P(C'|C) = A(C'|C)G(C'|C)$ satisfies detailed balance; when a change is rejected, the configuration remains unchanged.

Substituting this decomposition into the detailed balance equation for a given generating function G, we find the following condition for the acceptance ratio

$$\frac{A(C'|C)}{A(C|C')} = \frac{P(C')G(C|C')}{P(C)G(C'|C)}. \tag{2.13}$$

Any acceptance ratio satisfying this condition is valid; here we consider the Metropolis choice

$$A(C'|C) = \min\left(1, \frac{P(C')G(C|C')}{P(C)G(C'|C)}\right). \tag{2.14}$$

As mentioned earlier, a common advantage of rejection-full algorithms is the removal of the need to calculate normalization factors, highlighted here in the acceptance rate by the ratio of the probability distribution we seek to sample; we merely need a function $f(C) \propto P(C)$ for all C.

The algorithm defined by these generation and acceptance rates defines a master operator on the configuration space, and by construction we know the stationary state at infinite time. On finite time-scales the dynamics this algorithm generates may possess interesting properties, which can be understood through the master operator spectrum as discussed in Sec. 2.1.1. An example of a phenomenon which can be understood through the master operator's spectral structure, metastability, is discussed next.

2.1.3 Stochastic metastability and the Ising model

Generally in physical systems involving some form of dissipation removing energy over time, the state will relax into a small region of the configuration space, where it will remain for a substantial period of time. In a generic model the time-scale for remaining in this region can be effectively infinite, and this area of the configuration space can be associated with a stable stationary state. Despite this, many models may appear to have achieved stationarity for a significant time, only to eventually transfer to a new region and spend a comparable time located there; such regions are referred to as metastable.

An easy regime to observe and understand metastability is that of equilibrium statistical mechanics: consider an energy landscape on the configuration space which consists of two minima, seperated by a substantially higher energy barrier. When the dynamics has difficulty overcoming this barrier – such as the small local changes induced by thermal fluctuations at low temperatures – the system will remain close to these local minima on short time-scales. The regions around these minima can then be viewed as metastable, with transitions between these regions regulated by the height of the barrier: trajectories possess an intermittence of evolution within these regions, separated by occasional sharp transitions between them.

A classic example of metastability – as with many phenomena – is the 2D Ising model [13]. Here we have a simple energy given by the classical Hamiltonian

$$H(C) = -J \sum_{\langle i,j \rangle} s_i s_j - h \sum_i s_i, \tag{2.15}$$

where: h is the strength of an applied magnetic field; J is the strength of the spin-spin coupling, with $\langle i, j \rangle$ indicating this interaction is between nearest neighbours; and C here denotes the configuration of spins $s_i \in \{-1, 1\}$, i.e. down and up spins, on a square lattice. The configurations favoured by these spins are determined by the relative values of the coupling, magnetic field and the temperature T, according to how they influence the probabilities given by the Gibbs distribution

$$P(C) = \frac{e^{-\beta H(C)}}{\sum_C e^{-\beta H(C)}}, \tag{2.16}$$

where $\beta = 1/T$ is the inverse temperature. In the thermodynamic limit, at zero field there exists a phase transition at $T = 1$, distinguished by the average value of the magnetisation $M = \sum_i s_i$: for $T > 1$ the relevant configurations are paramagnetic, with a mix of spin values giving an average of zero magnetisation, while for $T < 1$ the state favours all spins aligning up or down. Reintroducing the field at $T < 1$ then results in one of these two states becoming uniquely present in the stationary state of thermal dynamics, depending on the alignment of the spins.

Phase transitions are often accompanied by metastability when we instead consider a finite system size. At infinite size, when changes to the state are local, i.e. single spin flips, it is improbable for the system to transition between the all up and all down configurations most relevant at low temperatures. In contrast, for finite systems it is feasible that enough correct spin flips could occur to allow such a transition: the height of the barrier suppressing such an event is governed by the system size, due to the distance (in spin flips) between the states. These two metastable regions – the all up and all down states and the configurations close to them – are no longer singled out by the application of a small field: instead, the state aligned with it becomes more favourable, while the overall energy landscape remains dominated by interactions. We thus arrive at the picture described above: two metastable regions corresponding to the all up and all down states, separated by a barrier over states of intermediate magnetisation, with transitions influenced by the system size and applied field. This is pictured in Fig. 2.1, using configurations generated by the Metropolis-Hastings algorithm described in Sec. 2.1.2 as a demonstration.

The understanding of metastability as intermittence in trajectories is accompanied by a corresponding behaviour in the statistics. Considering many trajectories initiated at a local minimum, short time dynamics will produce

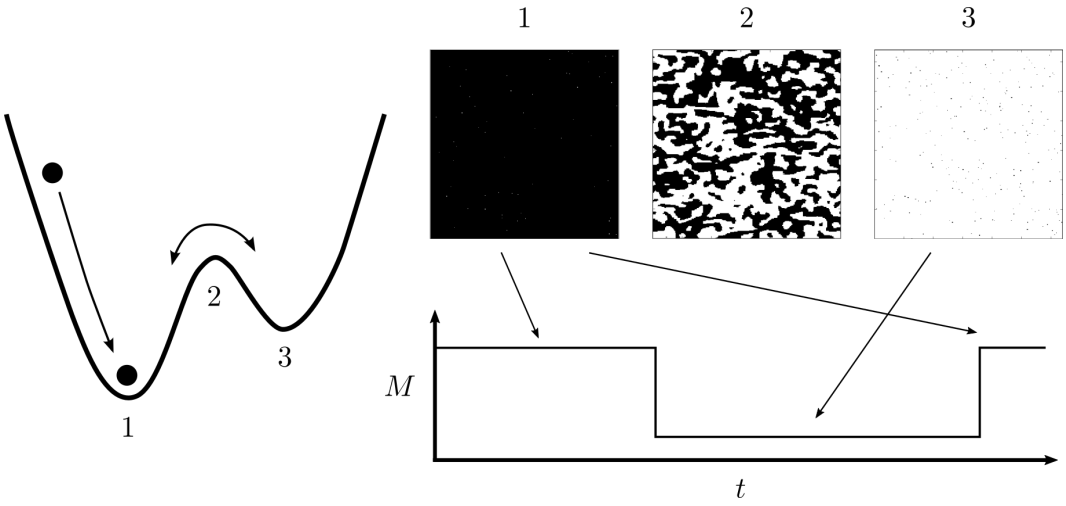


Figure 2.1: Left: A sketch of the energy landscape for the 2D Ising model at a non-zero applied field. The two wells, labelled 1 and 3, correspond to regions where most spins are aligned up or down. The mostly up configurations are less energetically favorable due to anti-alignment with the applied field. On short times a trajectory will approach the closest minima; longer time-scales allow transitions between these minima, via states such as configuration 2. **Top right**: Sample configurations of the 2D Ising model at low temperatures as described in the text, representative of states at minimal (1, 2) and intermediate (3) energies. **Bottom right**: A sketch of the magnetisation over a trajectory evolving according to thermal fluctuations. Time-scales for remaining within a minima are vast compared to the average time for transitions between them, resulting in a sharp jumps when the system moves to a different phase.

a probability distribution focused on the corresponding metastable region, invariant under small changes in time; such a distribution is referred to as a metastable state or phase. These phases are mixed on longer time-scales determined by the barrier, resulting in an eventual stationarity consisting of a probabilistic mixture of the metastable states. In the above example of the 2D Ising model, the states consist of probability distributions over the configurations close to the all up and all down states; the stationary state is a mixture of these determined by the strength of the applied field, cf. Fig. 2.2.

From the discussion above, evolution in models exhibiting metastability is clearly separated into distinct timescales: firstly, the system evolves towards a local minima and remains nearby for a substantial time; secondly, these metastable regions are mixed by transitions that are unlikely to occur relative to those within a region. In Sec. 2.1.1 we demonstrated that time-scales in the evolution of a system's probabilistic description are related to eigenvalues of the

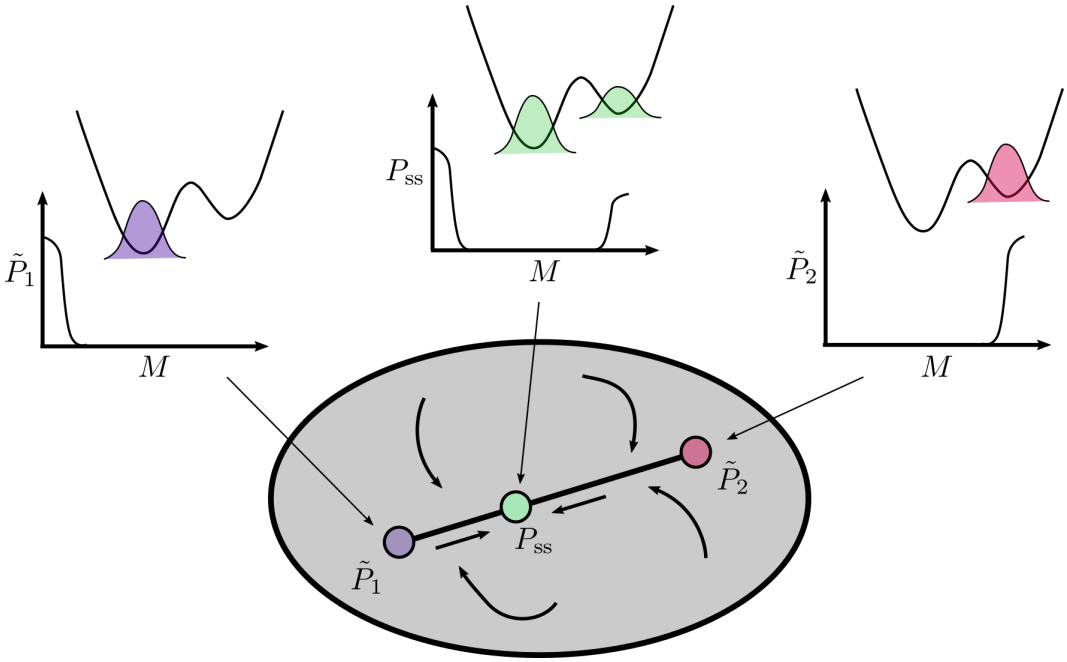


Figure 2.2: **Top**: Illustrations of magnetisation probability distributions for the two extreme metastable states $\tilde{P}_1$ and $\tilde{P}_2$, and the stationary state $P_{\rm ss}$, for the 2D Ising model. These distributions are accompanied by their supports on the phenomenological picture of the energy landscape. **Bottom**: The space of probability distributions, represented by the grey oval, contracts down to a low-dimensional metastable manifold after sufficient evolution. On much longer time-scales, states on this manifold evolve towards the stationary state, consisting of a mixture of the extreme states bounding this manifold.

master operator. It is therefore no surprise that the spectra of master operators form the basis for a theoretical description of metastability, introduced by Gaveau and Schulman [1, 14–18].

To illustrate this theory in the simplest way possible, let us consider a Markov process with a unique stationary state and a large gap between the second and third eigenvalues, i.e., $|\mathrm{Re}(\lambda_2)| \ll |\mathrm{Re}(\lambda_3)|$. This gap results in a simplification for the long time evolution of a probability $|P(0)\rangle$: for times t such that $1/|\mathrm{Re}(\lambda_3)| \ll t \ll 1/|\mathrm{Re}(\lambda_2)|$, we may approximate Eq. (2.12) as

$$|P(t)\rangle \approx |P_{\rm ss}\rangle + e^{t\lambda_2}\langle l_2|P_0\rangle\,|r_2\rangle\,. \tag{2.17}$$

These long-time states exist on a one dimensional *metastable manifold* (MM), parameterized by $\langle l_2|P_0\rangle$: the values of this coefficient are bounded by the maximum and minimum values of $\langle l_2|$ on the space of probability distributions: i.e., the maximum and minimum components of this vector in the configuration basis $c_2^{\max}$ and $c_2^{\min}$. These two values define the so-called *extreme metastable*

states (eMSs) on the boundary of the manifold:

$$\begin{aligned} |\tilde{P}_1\rangle &= |P_{\rm ss}\rangle + c_2^{\max} |r_2\rangle \\ |\tilde{P}_2\rangle &= |P_{\rm ss}\rangle + c_2^{\min} |r_2\rangle \,, \end{aligned} \tag{2.18}$$

which play the role of our metastable phases. We may rewrite Eq. (2.17) in terms of these phases, $|P(t)\rangle = p_1(t)\,|\tilde{P}_1\rangle + p_2(t)\,|\tilde{P}_2\rangle$. The long time distribution can therefore be understood as a time-dependent mixture of these two eMSs, with eventual relaxation towards the stationary state at times $t > 1/|\mathrm{Re}(\lambda_2)|$, given by a pair of probabilities $p_1^{\rm ss}$ and $p_2^{\rm ss}$ defined by

$$\begin{aligned} |P_{\rm ss}\rangle &= \frac{1}{\Delta c_2}\left(-c_2^{\min}\,|\tilde{P}_1\rangle + c_2^{\max}\,|\tilde{P}_2\rangle\right) \\ &= p_1^{\rm ss}\,|\tilde{P}_1\rangle + p_2^{\rm ss}\,|\tilde{P}_2\rangle \,, \end{aligned} \tag{2.19}$$

where $\Delta c_2 = c_2^{\max} - c_2^{\min}$. Note that $c_2^{\min} \leq 0$ as $\langle l_2|$ is orthogonal to the stationary state, which has purely positive components, so that the coefficients $p_1^{\rm ss}$ and $p_2^{\rm ss}$ (and the time evolving coefficients $p_1(t)$ and $p_2(t)$ leading to it) can be correctly interpreted as the probability weight of the two eMSs; the chance for a system being observed to be in each metastable region at long times.

Transitions between these regions inducing relaxation can be understood by constructing an effective evolution on this subspace: we project the master operator onto the eMS, finding an effective master operator given in terms of λ_2 and the maximum and minimum components of $\langle l_2|$

$$\mathcal{L}_{\rm eff} = \frac{-\lambda_2}{\Delta c_2}\begin{pmatrix} -c_2^{\max} & -c_2^{\min} \\ c_2^{\max} & c_2^{\min} \end{pmatrix}. \tag{2.20}$$

The off-diagonal elements correspond to the transition rates between the two metastable regions; this emulates the barrier separating our long-lived states. Lifetimes for these states are given by the negative inverse of the diagonal elements, which in this simple case directly relate to the transition rates.

In Chap. 4 we will see that the adaptation of this theory to the case of metastability between two phases in open quantum systems is nearly identical, with the same principles applied instead to the spectra of quantum master equations. The setup required to reach this spectral description, the theory of open quantum systems, is introduced next.

2.2 Open quantum systems

Consider a quantum system whose state space consists of a product of two Hilbert spaces, corresponding to a subsystem of interest and an environment, $\mathcal{H} = \mathcal{H}_S \times \mathcal{H}_E$ [19, 20]. Evolution on such a Hilbert space can be decomposed into parts which act non-trivially on only one of either state space, denoted by Hamiltonians H_S and H_E respectively, and an interaction term H_I which has a non-trivial action on both state spaces

$$H = H_S \otimes I + I \otimes H_E + H_I : \tag{2.21}$$

for simplicity we will absorb the identities into H_S and H_E

Given a density matrix ρ for this overall system we can extract the state ρ_S of the subsystem through a partial trace over the environment

$$\rho_S = \mathrm{Tr}_E(\rho) = \sum_{ijk} \langle e_i, s_j | \, \rho \, | e_i, s_k \rangle \, | s_j \rangle \langle s_k | \, , \tag{2.22}$$

where $|e_i, s_j\rangle = |e_i\rangle \otimes |s_j\rangle$ and $|e_i\rangle$, $|s_i\rangle$ are a basis of the environment and subsystem Hilbert spaces respectively.

An open quantum system consists of the evolution of a statistical description of the subsystem, taking into account its interaction with the environment without explicit consideration of the environments state. The time dependence of these statistical properties, encoded in the density matrix, follows from the Schrödinger equation and Eq. (2.22) as

$$\dot{\rho}_S = \mathrm{Tr}_E(-i[H, \rho]) =: \mathcal{O}(\rho), \tag{2.23}$$

where $\mathcal{O}$ represents the map from the full density matrix to the time derivative of the subsystem density matrix.

For an open quantum description we would require an equation equal to the right side of Eq. (2.23) which only depends on the state of the subsystem, so that its time evolution could be studied without knowledge of the environment. Unfortunately there are few situations where such an equation can be found exactly, and at best it in principle depends on the initial state of the environment. In general an exact equation for the right hand side in terms of the subsystems state would also be non-local in time, taking into account past states of the subsystem, making analytical or numerical analysis difficult if not impossible.

In order to make progress on studying such systems, several approximations can be made under assumptions on the properties of the environment and its interaction with the subsystem [19, 20].

Firstly, it is common to take the interaction between the subsystem and environment to be weak, i.e. small relative to the intrinsic energies of the subsystem and environment. We also take the environment to be "large" relative to the subsystem, i.e. the total energy of the bath is effectively infinite. These assumptions allow us to make two approximations to the overall state; we assume the effect of the interactions on the state of the environment is negligible on the timescales appropriate for the subsystem evolution (i.e. $\mathrm{Tr}_E(\rho)$ is time independent), and we assume the state of the system is separable. We thus take $\rho(t) = \rho_S(t) \otimes \rho_E$, with the above approximations commonly referred to as the Born approximation.

Secondly, while we have assumed that the state of the environment is invariant over time on average, the two-time correlations may be time dependent. Therefore interactions of the subsystem with the environment may leave a signature in the bath which influences future interactions. This would result in the time evolution for the current state of the subsystem depending on its past state, as opposed to solely its current state, in which case the system is referred to as non-Markovian. We therefore assume that the timescale on which the two-time correlations of the environment decay is small relative to the timescale of substantial changes in the state of the subsystem, and approximate the subsystem evolution as time-local. This is often called the Markov approximation, in reference to the environment being considered memoryless.

When we attempt to integrate out the environment degrees of freedom for a given microscopic model, the above approximations can be applied to reach an evolution equation for the subsystem density matrix which is a special case of a general equation. Much of our later work starts from this equation, without explicit derivation from a specific microscopic model. We therefore take the time to introduce it mathematically next.

2.2.1 The Lindblad equation

We now consider the subsystem alone, using the term system for simplicity. Suppose we desire a general form of evolution for a density matrix which maintains the the properties expected of a state by quantum mechanics, namely that the density matrix is hermitian, positive and has trace one. Further suppose we require it to be Markovian. Then it can be shown that the most general evolution obeying these requirements is of the form

$$\frac{d\rho}{dt} = \mathcal{L}(\rho), \tag{2.24}$$

where

$$\mathcal{L}(\rho) = -i[H, \rho] + \sum_j \left[J_j \rho J_j^\dagger - \frac{1}{2}\{J_j^\dagger J_j, \rho\} \right], \tag{2.25}$$

is the Lindblad master operator, or Lindbladian [21, 22]. Here H is a modified Hamiltonian containing the original subsystem Hamiltonian and a Lamb shift term of coherent effects resulting from environment interactions. The operators J_j mediate the dissipative effects of the system-environment interaction, inducing an eventual relaxation to a stationary density matrix. As we will see next in Sec. 2.2.2, the real time effects of these operators can be viewed as jumps, reminiscent of Sec. 2.1, with deterministic coherent evolution due to the Hamiltonian occuring inbetween. We will therefore refer to the operators J_i as jump operators.

Similar to the classical case previously discussed in Sec. 2.1.1, since $\mathcal{L}$ acts linearly on the density matrix, the evolution Eq. (2.24) can be understood in terms of its eigenvalues and eigenmatrices. Many of the results in later chapters are based on this spectral analysis, so we will discuss this in detail now.

Let us denote the eigenvalues of $\mathcal{L}$ by λ_k and order them such that $\mathrm{Re}(\lambda_k) \geq \mathrm{Re}(\lambda_{k+1})$. As $\mathcal{L}$ is in general not Hermitian, it has right and left eigenmatrices denoted by

$$\mathcal{L}(R_k) = \lambda_k R_k \tag{2.26}$$

and

$$\mathcal{L}^\dagger(L_k) = \lambda_k^* L_k, \tag{2.27}$$

respectively, where $\mathcal{L}^\dagger$ denotes the adjoint operator of the Lindblad operator defined by $\mathrm{Tr}[O\mathcal{L}(\rho)] = \mathrm{Tr}[\mathcal{L}^\dagger(O)\rho]$ for arbitrary operators O and ρ. We choose to normalise these such that

$$\mathrm{Tr}(L_k^\dagger R_{k'}) = \delta_{kk'}. \tag{2.28}$$

We note that, similar to the flat state in the classical case, the identity matrix plays the roll of an obvious left eigenmatrix with eigenvalue 0. To see this we note that it is simple to see from Eq. 2.25 that $\mathrm{Tr}[\mathcal{L}(\rho)] = 0$, corresponding to the equation's trace preservation under evolution. This can be rewritten as $\mathrm{Tr}[\mathcal{L}^\dagger(I)\rho]$. Since this holds for any ρ it therefore follows that $\mathcal{L}^\dagger(I) = 0$.

We now introduce a representation of density matrices in the form of stacking their rows one after another in a column, i.e. vectorizing the density matrix. Useful numerically for exact evolution and diagonalization, it also

provides a way to prove linear algebraic properties of the Lindblad equation. By mapping the action of linear operators on an arbitrary density matrix into this representation, we can construct the induced matrix representation of such maps acting on the vectorized density matrices. It can be shown that this induced representation takes the simple form

$$A\rho B \to A \otimes B^T \underline{\rho}, \tag{2.29}$$

for generic operators A and B, where in a D dimensional Hilbert space $\underline{\rho}_i = \rho_{(i \mod D),(i-i \mod D)}$, for $i = 1, ..., D^2$. Applied to the Lindblad operator, this mapping gives us the matrix

$$\begin{aligned} \mathcal{L}_M &= -i\left(H \otimes I - I \otimes H^T\right) \\ &\quad + \sum_j \left[J_j \otimes J_j^* - \frac{1}{2}\left(J_j^\dagger J_j \otimes I + I \otimes J_j^T J_j^*\right)\right]. \end{aligned} \tag{2.30}$$

Unlike the classical case, the Gershgorin circle theorem [11] does not prove $\mathrm{Re}(\lambda_k) \leq 0$. Instead, this can be proven by first noting that evolution of the magnitude of coefficients in an expansion of a density matrix in the right eigenmodes (see below) is determined by the real part of the eigenvalue. Since a hermitian basis of the eigenmatrices can be chosen, these coefficients must lie between the maximum and minimum eigenvalues of the left eigenmatrices, which must be finite if the Hilbert space is finite. For these upper and lower bounds on the coefficients to hold for the time evolved density matrix, the real part of the eigenvalues must therefore be non-positive, to induce a decay in the magnitude of the coefficients. For infinite size systems, we assume this holds as a limiting behaviour of finite systems.

The time evolution of the density matrix can now be written as

$$\underline{\rho}(t) = e^{it\mathcal{L}_M}\underline{\rho}(0). \tag{2.31}$$

The Brouwer fixed point theorem, now on the convex space of density matrices, then again implies we have at least one stationary density matrix of this exponentiated operator, with eigenvalue 1. Since this holds for all times this density matrix is thus also a right eigenmatrix of the Lindblad operator itself with eigenvalue 0. As this stationary state is the dual matrix to the identity, it follows from orthonormality that all other right eigenmatrices must have zero trace, i.e. they don't contribute to the total normalization of a density matrix but merely modify its components, analogous to the classical case.

Given all left and right eigenmatrices we can therefore perform a decomposition of a given density matrix. Defining

$$c_k = \mathrm{Tr}[L_k^\dagger \rho(0)] \tag{2.32}$$

for an initial state $\rho(0)$, the system's state at time t is then given by

$$\rho(t) = e^{t\mathcal{L}}[\rho(0)] = \sum_k c_k e^{t\lambda_k} R_k. \tag{2.33}$$

As in the classical case, the non-positivity of the real part of the eigenvalues corresponds to the decay of dynamical modes over lifetimes of $\tau_i = 1/|\mathrm{Re}(\lambda_i)|$. If there is a single eigenvalue with zero real part, all states evolve to a unique density matrix at infinite time, while multiple eigenvalues with zero real part results in initial state dependent stationary states.

The Lindblad equation provides a complete description of the evolution for the system's statistics, i.e. the time dependence of its density matrix, in the same way a classical master operator provides a complete description of time dependence for a probability distribution. In classical systems we can alternatively perform stochastic simulations in which a specific configuration of the system is evolved randomly, in such a way that the statistics of these trajectories replicates the probability distribution.

Along with being numerically efficient, such an approach is often closer to what is observed in experimental situations, thus providing a physical perspective of the system's dynamics. It is therefore desirable to construct stochastic dynamics in the Hilbert space of pure states which reproduces the statistical evolution of the Lindblad equation.

There are two approaches most commonly taken which correspond to different experimental procedures; simulations based on continual diffusion, and simulations based on coherent evolution interspersed with stochastic jumps. This second approach, referred to as Quantum jump Monte Carlo (QJMC), is introduced next.

2.2.2 Quantum jump Monte Carlo

Suppose we have an open quantum system coupled to the vacuum electromagnetic field, with continual measurements taken of the field degrees of freedom. Whenever the system interacts with the environment through the coupling, a photon will be emitted into the electromagnetic field, and detected by the measurement. This detection corresponds to the gain of information about the

state of the system. Since we haven't measured the system directly the state has not collapsed to a classical state, however we are aware it has interacted with the environment, and as such know the pure state of the system must have changed from the alternative result of its internal dynamics.

This concept can be used to derive a simulation scheme for the evolution of the pure state of the system in a specific trajectory, in which coherent evolution proceeds for a random time, before an emission is detected and the pure state is updated accordingly. We refer to the literature for a detailed derivation of this scheme's validity [19,20,23], and discussion of its application to many-body systems [24], and here simply outline the simulation procedure as used in our research.

A simulation begins on the assumption that the system is in a pure state $|\psi(0)\rangle$. We adopt the statistical interpretation of the density matrix, i.e. we consider a full density matrix to consist of a probability distribution (the eigenvalues) over a basis of pure states (the eigenstates). As such if we wish to find the evolution of statistics for a general density matrix, we initialize trajectories from the different eigenstates in proportion with the eigenvalues.

Evolution between jumps is described by a modified, non-hermitian effective Hamiltonian, given by

$$H_{\text{eff}} = H - \frac{i}{2}\sum_{j=1}^{N} J_j^\dagger J_j, \tag{2.34}$$

where N is the number of jump operators, with time evolution then given by $|\psi(t)\rangle = e^{-itH_{\text{eff}}}|\psi(0)\rangle$. For a microscopically derived Hamiltonian, this would modify the coefficient of the Lamb-shift term induced by interaction with the environment, adding an imaginary part.

The non-hermiticity of this operator means that the evolution is not norm conserving. Indeed by considering the time derivative of $\langle\psi(t)|\psi(t)\rangle$ we can show that the norm squared is monotonically decreasing. We can further show that the integral of the norm squared to infinity is 1.

This squared norm serves as a probability density for the time at which a jump occurs from a given initial state. To decide when a jump occurs, we thus draw a random number between 0 and 1, then evolve until the norm drops below this value.

After a jump has occurred a decision must be made as to which jump was applied to the state. The correct choice of probability distribution to recover

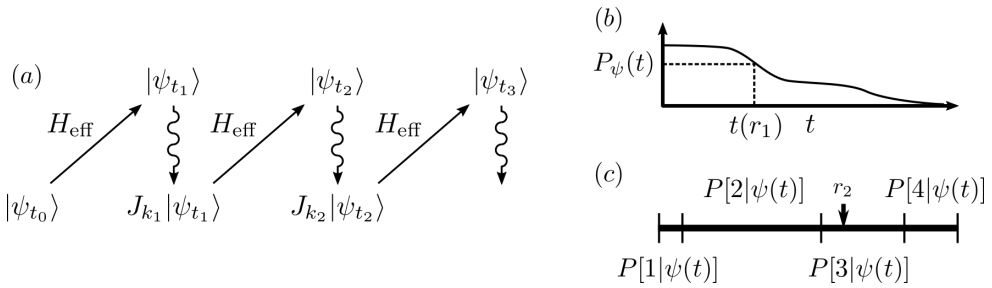


Figure 2.3: An outline of the basic quantum jump Monte Carlo algorithm. The overall procedure is sketched in (a): periods of evolution mediated by H_{eff}, interspersed with jumps due to the action of the operators J_k. The period of evolution is calculated as in (b), by comparison of a random number r_1 with the function $P_\psi(t) = ||\,|\psi_t\rangle\,||^2$, resulting in a time $t(r_1)$ at which a jump occurs. When the system jumps, a second random number r_2 is compared with the probability distribution $P[i|\psi]$ specified by Eq. (2.35), as shown in (c).

the statistical evolution of the Lindblad equation is given by

$$P[i|\psi(t)] = \frac{\langle\psi(t)|\, J_i^\dagger J_i\, |\psi(t)\rangle}{\sum_j \langle\psi(t)|\, J_j^\dagger J_j\, |\psi(t)\rangle}. \tag{2.35}$$

When a jump occurs we thus calculate these normalized probabilities, use them to partition the interval $[0, 1]$, then draw another random number to choose which jump to apply. This jump is then applied to the evolved state, which is then normalized so the process can be repeated

$$|\psi(t)\rangle \to \frac{J_i\,|\psi(t)\rangle}{\sqrt{\langle\psi(t)|\, J_i^\dagger J_i\, |\psi(t)\rangle}}. \tag{2.36}$$

After many runs of these trajectories, statistical properties of the evolved density matrix can then be calculated from stochastic averages over these trajectories. For example, the expectation value of an operator O at a time t can be calculated as

$$\langle O\rangle_t = \frac{1}{N}\sum_{i=1}^{N} \langle\psi_i(t)|\, O\,|\psi_i(t)\rangle\,, \tag{2.37}$$

where N is the number of trajectories and $|\psi_i(t)\rangle$ is the normalised state of the ith trajectory at time t.

The full simulation procedure, illustrated by Fig. 2.3, is then

1. Given an initial density matrix $\rho(0)$ with eigenvalues p_i and eigenvectors $|\phi_i\rangle$, we draw an initial state $|\psi(0)\rangle$ from these eigenvectors with probabilities equal to the corresponding eigenvalues.

2. Draw a random number $r_1 \in [0,1]$. Given a current state $|\psi(t_i)\rangle$ determine when a jump occurs by solving $|| \, |\tilde{\psi}(t_{i+1})\rangle \, ||^2 = r_1$ for t_{i+1}, where $|\tilde{\psi}(t_{i+1})\rangle$ is the unnormalized state

$$|\tilde{\psi}(t_{i+1})\rangle = e^{i(t_{i+1}-t_i)H_{\text{eff}}} \, |\psi(t_i)\rangle \, . \tag{2.38}$$

3. Draw another random number $r_2 \in [0,1]$. Given the time t_{i+1} at which the next jump occurs from step 2, determine which jump occurs from Eq. (2.35) by finding the minimum value of l such that

$$\frac{\sum_{k=1}^{l} \langle\tilde{\psi}(t_{i+1})| \, J_k^\dagger J_k \, |\tilde{\psi}(t_{i+1})\rangle}{\sum_j \langle\tilde{\psi}(t_{i+1})| \, J_j^\dagger J_j \, |\tilde{\psi}(t_{i+1})\rangle} > r_2. \tag{2.39}$$

4. Given the index l of the applied jump from step 3, apply the jump to the state and normalise to find the post-jump state

$$|\psi(t_{i+1})\rangle = \frac{J_l \, |\tilde{\psi}(t_{i+1})\rangle}{\sqrt{\langle\tilde{\psi}(t_{i+1})| \, J_l^\dagger J_l \, |\tilde{\psi}(t_{i+1})\rangle}}. \tag{2.40}$$

5. Given each new state $|\psi(t_{i+1})\rangle$ we then repeat from step 2 until the desired condition to end a trajectory is reached.

The bulk of the numerical processing in this procedure is contained in steps 2 and 3, as calculations for step 4 can be removed by storing the unnormalized jumped states and expectations during step 3. Often the determination of the jump applied in step 3 can be made more efficient by exploiting algebraic relationships between the jump operators, an example of which will be seen in Chap. 4.

Step 2 is usually the most demanding. The most precise approach, exact calculation of the jump time using a root finder and matrix exponentiation, is extremely computationally expensive. In contrast, approximate evolution such as Runge-Kutta introduces both numerical error to the evolved state and potential discretization error to the jump time. We instead consider a middle ground where the evolution is kept exact, while the jump time is restricted to a discrete set. Our approach requires some additional initialization relative to integrators like Runge-Kutta: however, this is compensated by a reduction in runtime for each trajectory, along with a reduced error.

We begin by exponentiating the effective Hamiltonian for some small time-step Δt, getting a non-unitary evolution matrix U_{N_U}, where N_U is the number of unitaries we will create. We construct a set of unitary evolvers for larger

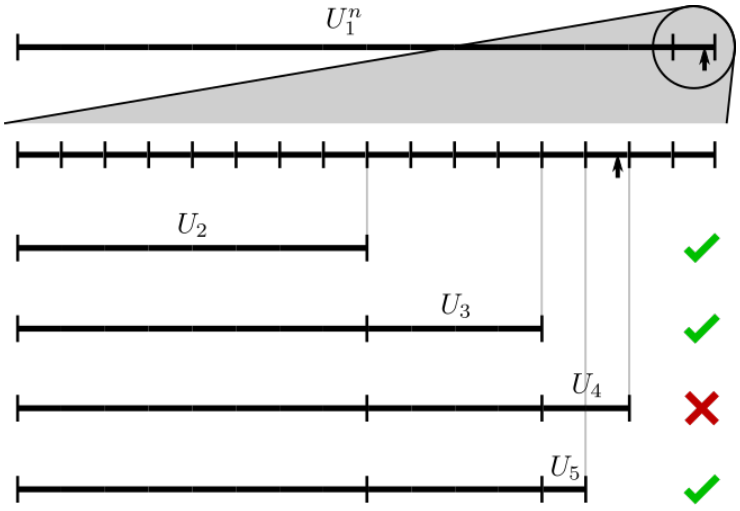


Figure 2.4: The binary search procedure used to locate the jump time. First, the maximum number of the largest step-size evolver, U_1, is applied such that the norm remains above the random number (the exact time corresponding to this random number is indicated by the arrow). Next, a sequence of evolvers corresponding to half the step size of the previous are applied one after another, comparing the norm to the random number at each step: if the norm drops below the random number, the evolution is rejected and the previous state is used, otherwise the state is accepted.

time-steps using even powers of each successive matrix, $U_k = U_{k+1}^2$, for $k \in \{1, ..., N_U\}$. This set of evolvers allows us to break down step 2 of the above algorithm into a binary search, as follows

1. Draw a random number $r_1 \in [0, 1]$. Given the current state $|\psi(t_i)\rangle$ following the ith jump, we evolve repeatedly with the largest unitary matrix, finding the first value of n such that

$$||U_1^n |\psi(t_i)\rangle|| < r_1. \tag{2.41}$$

2. Beginning from the state $|\phi_1\rangle = U_1^{n-1} |\psi(t_i)\rangle$ at time $\tilde{t}_1 = t_i + 2^{N_U - 1}(n-1)\Delta t$, with $k = 2$:

   i. Calculate $U_k |\phi_{k-1}\rangle$.

   ii. If $||U_k |\phi_{k-1}\rangle|| < r_1$ set $|\phi_k\rangle = |\phi_{k-1}\rangle$ and $\tilde{t}_k = \tilde{t}_{k-1}$. Else set $|\phi_k\rangle = U_k |\phi_{k-1}\rangle$ and $\tilde{t}_k = \tilde{t}_{k-1} + 2^{N_U - k}\Delta t$.

   iii. If $k = N_U$, set $|\tilde{\psi}(t_{i+1})\rangle = |\phi_k\rangle$ and $t_{i+1} = \tilde{t}_k$. Else increment k and return to step i.

This process, demonstrated in Fig. 2.4, consistently underestimates the time at which the jump occurs; however, the smallest step can be tuned to minimize this error. The largest step size should ideally be chosen to be slightly smaller than one or two standard deviations below the average time between jumps: this minimizes the number of times the evolvers need to be applied to the state between jumps. These choices for largest and smallest step size ensure the minimum average number of matrix multiplications in a trajectory, for a desired accuracy of the time at which jumps occur.

Chapter 3

Weak symmetries in open quantum systems

One of the most common themes in physics is the use of symmetries: a transformation under which the dynamics of a system is invariant. Understanding such symmetries not only provides a deeper intuition for the system of interest, but additionally acts as a powerful technical tool in their analysis; such transformations indicate a redundancy in the description of the system. Removal of this redundancy often results in simplifications that leave the model more amenable to analytical or numerical study.

Symmetries in closed classical and quantum systems, where evolution of the state is deterministic, are accompanied by a conserved quantity: a physical observable which remains constant over time. These conserved quantities partition the state space into subspaces, which evolution can not transition between, with a reduced description applicable in each subspace. While a similar reduction exists in open systems, such as those introduced in Chap. 2, the mathematical structure is more complex: the presence of a symmetry may not correspond to a conserved quantity; this is referred to as a weak symmetry. Strong symmetries then refer to those with a corresponding conserved quantity.

In this chapter we discuss a particular representation of the Lindblad equation which is tailored to its weak symmetries, and its use in numerical or analytical studies. We begin with an introduction to the mathematics of weak and strong symmetries in Sec. 3.1 [25, 26], before introducing our weakly symmetric representation of the Lindblad equation with examples in Sec. 3.2. We then discuss two immediate applications of this representation: the block diagonalization of the Lindbladian in Sec. 3.3, and the symmetry reduction of

QJMC simulations in Sec. 3.4.

3.1 Weak and strong symmetries

In closed quantum mechanics, any physical transformation of a state must leave its norm invariant for probability conservation; transformations such as symmetries are therefore represented by unitary matrices, $|\psi\rangle \to U|\psi\rangle$. For a symmetry this transformation must leave the dynamics unchanged: the process of transforming the state, calculating its time derivative, then reversing the transformation, must be the same as simply calculating its time derivative. Stating this process mathematically, we find the following condition for a unitary transformation to represent a symmetry

$$U^\dagger H U = H \Leftrightarrow [H, U] = 0. \tag{3.1}$$

This in turn implies that the expectation value of all functions of this operator are invariant under time, i.e. U is conserved.

There are two distinct classes of symmetry which can obey the above condition,

- *Discrete* symmetries consist of a discrete base set of unitary operators $\{U_1, U_2, ...\}$. The system is then invariant under the application of any powers of these operators in any order. The simplest example is a representation of the cyclic group of order n, defined by a single base unitary U with the property $U^n = I$. This group commonly occurs in the description of translation invariant systems with periodic boundary conditions.

- *Continuous* symmetries consist of parametrized families of unitary transformations $U(\theta)$. For simplicity we consider one dimensional symmetries, i.e. θ is a real number. It can be shown that such a family of transformations can in general be understood by the properties of a single hermitian operator, known as the generator G, related to the unitaries by $U(\theta) = e^{-i\theta G}$. Since the system is by definition invariant for all θ, we find $[H, G] = 0$; G is hermitian and conserved, thus providing a physical observable with a time independent expectation value, referred to as a conserved quantity. A trivial conserved quantity in quantum mechanics is the identity matrix I, the conservation of which is simply the statement

of probability conservation. The corresponding continuous symmetry is the global phase invariance of quantum states, $U(\theta) = e^{-i\theta I}$.

Since operators related to symmetries are conserved, the system evolution can only transition between states which have the same expectation value of these operators. From a linear algebraic perspective, this corresponds to the Hamiltonian being block diagonal in the eigenbasis of the symmetry. Taking $|\psi_i\rangle$ to be an eigenvector of a symmetry U with eigenvalue λ_i, the block diagonalization of H follows from

$$UH|\psi_i\rangle = HU|\psi_i\rangle = \lambda_i H|\psi_i\rangle, \tag{3.2}$$

i.e. $H|\psi_i\rangle$ is also an eigenvector of the symmetry U with eigenvalue λ_i. Studying the spectra of a the set of base unitaries or generators defining a symmetry in the discrete or continuous cases, respectively, thus allows us to partition the state space.

In the open context we instead consider unitary transformations of the density matrix $\rho \to U\rho U^\dagger$. If we again consider a symmetry to leave the system dynamics invariant, we have

$$\mathcal{U}^\dagger \mathcal{L} \mathcal{U} = \mathcal{L} \to [\mathcal{L}, \mathcal{U}] = 0, \tag{3.3}$$

where the symmetry superoperator $\mathcal{U}$ satisfies $\mathcal{U}(\rho) = U\rho U^\dagger$, and U may belong to a discrete or continuous symmetry. In the later case we also have the more fundamental result $[\mathcal{L}, \mathcal{G}] = 0$ where $\mathcal{G}(\rho) = -i[G, \rho]$ and G is the generator superoperator of the symmetry. For clarity we first discuss weak and strong symmetries in the discrete case, before introducing the adaptation to continuous symmetries.

3.1.1 Discrete symmetries

For open systems, time independence of an operator's expectations is a consequence of $\mathcal{L}^\dagger(U) = 0$, however Eq. (3.3) does not imply the existence of any operator satisfying this condition. In turn, a conserved quantity as defined above does not imply the existence of a symmetry as defined in Eq. (3.3). As such for open systems there is a general disconnect between symmetries and conserved quantities of the dynamics. Symmetries defined by Eq. (3.3), or by commutation with the generator superoperator for the continuous case, without a corresponding conserved operator are referred to as weak symmetries. Strong symmetries thus refer to those for which a symmetry group has

a corresponding conserved quantity. Such transformations possess a general definition which implies both Eq. (3.3) and a conserved quantity: a group of symmetry transformations satisfying the conditions $[H, U] = 0$ and $[J_i, U] = 0$.

Intuition for the effects of these two types of symmetry can be gained from considering their implications for the dynamical flow in the space of density matrices, similar to the block diagonalization of the Hamiltonian above. This will be based on the Hilbert subspaces given by the symmetry eigenspaces $\mathcal{H}_k$; for convenience we define I_k to be the identity matrix restricted to the kth eigenspace of the unitary matrix U, acting as a projection operator onto this space.

Strong symmetries. Here the Lindblad operator is invariant not only under the application of the symmetry superoperator $\mathcal{U}$, but under the independent left and right action of the state space unitary U. In other words, defining $\mathcal{U}_L(\rho) = U\rho$ and $\mathcal{U}_R(\rho) = \rho U^\dagger$, we have two commuting symmetries $[\mathcal{L}, \mathcal{U}_L] = [\mathcal{L}, \mathcal{U}_R] = [\mathcal{U}_L, \mathcal{U}_R] = 0$. We therefore see that if $M_{j,k}$ is an eigenmatrix of $\mathcal{U}_L$ and $\mathcal{U}_R$, $\mathcal{L}(M_{j,k})$ remains an eigenmatrix of these superoperators with the same eigenvalues. These eigenvalues belong to the same set as those of U, with different multiplicity: this follows from the matrix representation Eq. (2.29). The Lindblad operator thus has the block diagonalization $\mathcal{L}_{j,k}(\rho) = I_j \mathcal{L}(I_j \rho I_k) I_k$ such that $\mathcal{L} = \sum_{j,k} \mathcal{L}_{j,k}$, with eigenmatrices of each block $\mathcal{L}_{j,k}$ restricted to the subspace $\mathcal{H}_j \times \mathcal{H}_k$

Dynamically, the Lindblad equation is thus restricted to mixing each block $I_j \rho I_k$ of the density matrix within itself. The diagonal blocks must each possess at least one stationary state, while off-diagonal blocks may also contain stationary coherences. The eigenmatrices of these off-diagonal blocks are correlated, due to hermiticity preservation: $\mathcal{L}_{j,k}(R^\dagger) = \mathcal{L}_{k,j}(R)^\dagger$. This is illustrated in Fig. 3.1(a).

Weak symmetries. We must now instead consider the spectrum of the superoperator symmetry transformation $\mathcal{U}$. The spectra of the unitary $\mathcal{U}$ follow from that of U by using the matrix representation Eq. (2.29): the eigenvalues of $\mathcal{U}$ belong to the same set as U, with different multiplicity, as in the strong case. Specifically, given eigenvalues λ_i of U, we find the eigenvalues of $\mathcal{U}$ are of the form $\lambda_{i,j} = \lambda_i \lambda_j^*$; let Λ_m represent the set of distinct eigenvalues of $\mathcal{U}$.

Suppose now we have an eigenmatrix $M_{j,k} \in \mathcal{H}_j \times \mathcal{H}_k$ of $\mathcal{U}$ with eigenvalue $\lambda_{j,k}$. The matrix $\mathcal{L}(M_{j,k})$ remains an eigenmatrix with the same eigenvalue $\lambda_{j,k}$, however we may have $\mathcal{L}(M_{j,k}) \notin \mathcal{H}_j \times \mathcal{H}_k$: there may be other combinations of

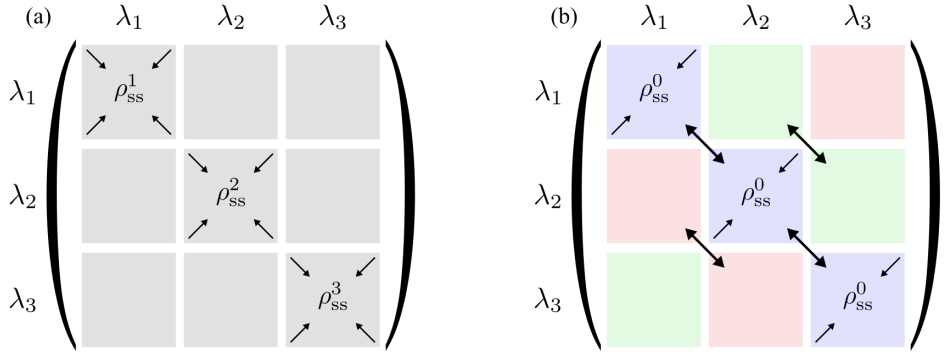


Figure 3.1: Diagrammatic representations of the flow induced on the blocks of the density matrices in the symmetry eigenbasis, for (a) strong and (b) weak symmetries with three distinct eigenvalues. (a) All 9 blocks of the density matrix evolve independently, with the diagonal blocks each possessing their own stationary density matrix. (b) Here a weak symmetry associated to a superoperator with three distinct eignevalues disconnects the dynamics of the density matrix into three independent sets of blocks, indicated by different colors. The final stationary state is split between the diagonal blocks. The specific structure considered here occurs in translation invariance for a model with three sites.

λ_j and λ_k which provide the same superoperator eigenvalue $\lambda_{j,k}$, thus $\mathcal{L}(M_{j,k})$ may not even reside in a single pair of symmetry eigenspaces. We thus find that a Lindblad operator with a weak symmetry has the block structure

$$\mathcal{L}_m(\rho) = \sum_{\substack{l,\ n,\\ \lambda_{l,n}=\Lambda_m}} \sum_{\substack{j,\ k,\\ \lambda_{j,k}=\Lambda_m}} I_l \mathcal{L}(I_j \rho I_k) I_n, \tag{3.4}$$

where $\mathcal{L} = \sum_m \mathcal{L}_m$ and $\mathcal{L}_m$ is restricted to the direct sum space

$$\mathcal{B}_m = \bigoplus_{\substack{j,\ k,\\ \lambda_{j,k}=\Lambda_m}} \mathcal{H}_j \times \mathcal{H}_k. \tag{3.5}$$

This structure results in a flow induced by the Lindblad equation on density matrices distinct to that of a strong symmetry. Instead of every block in the symmetry eigenbasis evolving independently, blocks associated with the same eigenvalue of the superoperator are mixed together, cf. Fig. 3.1(b). For example, the diagonal blocks are connected to each other but disconnected from all others, with $\Lambda_0 = 1$: physically we can imagine a system in a state with a particular value of the conserved quantity, remaining constant until a jump occurs, causing a transfer of that particular quantity with the environment and changing its value in the system. This can be viewed as the origin of the

lack of a corresponding conserved quantity. Therefore, we generically (in the absence of any other strong symmetries) have a unique stationary state spread across the whole eigenspace of the unitary U.

3.1.2 Continuous symmetries

For continuous symmetries the above discussion is modified by considering the spectra of the generator G and its superoperator counterparts: in the strong case, we make use of left and right generator superoperators defined by $\mathcal{G}_L(\rho) = -iG\rho$ and $\mathcal{G}_R(\rho) = i\rho G$ respectively; in the weak case, we consider the generator superoperator $\mathcal{G}(\rho) = -i[G, \rho]$. The eigenvalues of $\mathcal{G}_L$ and $\mathcal{G}_R$ are the same as that of the generator G; for $\mathcal{G}$, eigenvalues are of the form $\lambda_{i,j} = -i(\lambda_i - \lambda_j)$, where λ_i here represent eigenvalues of G.

Decomposition of the Lindblad operator into blocks is then conducted according to the eigenspaces of G and eigenvalues of the above superoperators, with the same resulting structure for the flow in the space of density matrices, shown in Fig. 3.1.

3.1.3 Uses of strong symmetries

Beyond the block structure of the Lindblad operator as a whole, strong symmetries further imply that the Hamiltonian and jump operators are themselves block diagonal in the symmetry eigenbasis. Labeling the blocks $H_k = I_k H I_k$ and $J_{i,k} = I_k J_i I_k$, we find there is a simple relationship between these and the blocks of the Lindblad operator: written in the matrix representation of Eq. (2.29) we have

$$\begin{aligned} \mathcal{L}^M_{j,k} &= -i\left(H_j \otimes I_k - I_j \otimes H_k^T\right) \\ &\quad + \sum_i \left[J_{i,j} \otimes J^*_{i,k} - \frac{1}{2}\left(J^\dagger_{i,j} J_{i,j} \otimes I_k + I_j \otimes J^T_{i,k} J^*_{i,k}\right)\right]. \end{aligned} \tag{3.6}$$

In this form it is transparent that $\mathcal{L}_{k,k}$ are themselves Lindblad operators, simply on a reduced Hilbert space.

The above form allows for efficient numerical construction of the Lindblad operator blocks, and opens up the potential for algebraic techniques to be applied to these reduced operators. Considering the diagonal blocks, it is further clear that for simulations based on QJMC we need only consider the state restricted to a single eigenspace at any given time, run using the relevant blocks of the Hamiltonian and jump operators. It is therefore desirable to find

a similar construction in the case of weak symmetries. Unfortunately, while the presence of a weak symmetry might be clear, the Hamiltonian and jump operators of many models may not transform in any sensible way under this symmetry: a simple example is a translation symmetry, as we will see in the next section. This problem is resolved by the existence of a transformation which renders the Hamiltonian and jump operators respectful of weak symmetries, allowing the construction of an equation similar to Eq. (3.6) in Sec. 3.3, and providing an enhanced QJMC algorithm covered in Sec. 3.4.

3.2 Weakly symmetric representations

For a generic Lindblad operator with a weak symmetry, there need not be any useful relationship between the Hamiltonian and jump operators defining the model, and the discrete unitary transformation U or continuous symmetry generator G. Despite this, it has recently been shown [27] that if a weak symmetry exists, there exists a non-unique transformation to a representation of these operators which in some sense respects this symmetry. We refer to this as a weakly symmetric representation of the Lindblad operator. Specifically, we define this as any representation in which the Hamiltonian and jump operators satisfy $\mathcal{U}^\dagger(H) = H$ and $\mathcal{U}^\dagger(J_m) = \Lambda_m J_m$ for the discrete case, or $\mathcal{G}^\dagger(H) = 0$ and $\mathcal{G}^\dagger(J_m) = i\Lambda_m J_m$ for the continuous case: the Hamiltonian and jump operators are eigenmatrices of the relevant symmetry superoperator.

The general proof of existence for such representations and their construction in specific situations relies on the use of two invariance properties of the Lindblad equation: allowing us to transform to an alternative Hamiltonian and set of jump operators which describe the same statistical evolution. These transformations are basis independent, i.e. they are distinct from a simple change of basis in a given representation of the Hamiltonian and jump operators. The first of these relates to unitary transformations of the set of jump operators, such that the Lindblad equation is invariant under any transformation

$$J_i \to J_i' = \sum_i u_{ij} J_j, \tag{3.7}$$

where u_{ij} is a unitary matrix. The second transformation relates to a shift in the trace of each jump operator or the Hamiltonian, i.e. $J_i \to J_i' = J_i + c_i I$ and

$$H \to H' = H + \frac{1}{2i} \sum_i \left(c_i^* J_i - c_i J_i^\dagger \right) + bI, \tag{3.8}$$

where the c_i are complex and b is real.

We refer to Ref. [27] for the general proof and construction scheme, along with some fundamental results that follow from its existence, here considering some simple examples.

3.2.1 Example 1: discrete translations

Consider a general model with a Hamiltonian of the form $H = \sum_i H_i$ and jump operators labelled J_i, with $i \in \{0, ..., N-1\}$ and a unitary transformation U such that $U^\dagger H_i U = H_{i-1}$ and $U^\dagger J_i U = J_{i-1}$. A simple example of such a system would be a periodic chain of N particles, with nearest neighbour interactions in the Hamiltonian and a set of single site jump operators; the symmetry transformation corresponds to translations along the chain.

It is clear that the Lindbladian given by these operators would be invariant under the superoperator transformation $\mathcal{U}$, however, the jump operators stated here are not eigenmatrices of this transformation. To reach a weakly symmetric representation, in this case we can simply apply a discrete Fourier transform to the set of jump operators. Defining

$$J'_k = \sum_{m=0}^{N-1} e^{2\pi i \frac{km}{N}} J_m, \tag{3.9}$$

for $k \in \{0, ..., N-1\}$, we find $\mathcal{U}^\dagger(J'_k) = e^{2\pi i \frac{k}{N}} J'_k$ as required for a weakly symmetric representation, where the index k can be interpreted as a quasi-momentum.

3.2.2 Example 2: spin rotations

As a second example consider a simple single spin model described by a Hamiltonian $H = \Delta\sigma_z$, with jump operators $J_1 = \sqrt{\gamma}\sigma_x$ and $J_2 = \sqrt{\gamma}\sigma_y$, with Δ and γ some parametrization of the dynamics. While neither jump operator is invariant under the one-parameter family of unitaries $U(\theta) = e^{-i\theta\sigma_z}$, where the generator $G = \sigma_z$, the superoperator $\mathcal{G}$ commutes with the Lindblad operator. Here the unitary transformation on the jump operators is simply

$$\begin{pmatrix} J'_1 \\ J'_2 \end{pmatrix} = \frac{1}{2} \begin{pmatrix} 1 & i \\ 1 & -i \end{pmatrix} \begin{pmatrix} J_1 \\ J_2 \end{pmatrix} = \sqrt{\gamma} \begin{pmatrix} \sigma_+ \\ \sigma_- \end{pmatrix}, \tag{3.10}$$

resulting in $\mathcal{G}^\dagger(\sigma_\pm) = \pm i\sigma_\pm$, with eigenvalues $\Lambda_\pm = \pm 1$.

3.3 Block diagonalizing the Lindblad operator

Once a model has been transformed into the weakly symmetric representation as demonstrated above, the symmetry properties of the Hamiltonian and jump operators can be used to efficiently construct blocks of the Lindblad operator, similar to Eq. (3.6); we now use the weak representation to derive an analogous formula for weak symmetries.

Let us assume we have a Lindblad equation which is already in the weakly symmetric representation, with respect to some symmetry with eigenvalues λ_i, labeling the superoperator eigenvalues Λ_i. These may correspond to eigenvalues of base unitary transformations for the discrete case, or of a generator for the continuous case. As in the strong case, the Hamiltonian is simply block diagonal, with blocks denoted by $H_j = I_j H I_j$.

For the jumps, the definition of the weak representation tells us that, given a symmetry eigenvector $|\psi_j\rangle \in \mathcal{H}_j$ with eigenvalue λ_j, $J_i |\psi_j\rangle$ remains an eigenvector with a modified eigenvalue. A single eigenspace is thus mapped to a single other – potentially different – eigenspace by the action of a given jump operator. These operators can therefore be reduced to a single block per eigenspace, like the Hamiltonian, with the distinction that these blocks may be off-diagonal, c.f. Fig. 3.2. We denote those blocks $J_{i,j} = I_{f_i(j)} J_i I_j$, where the $f_i(j)$ are a set of functions which provide the index of the eigenspace that $\mathcal{H}_j$ is mapped to by a jump operator with eigenvalue Λ_i: these are defined by $\lambda_{f_i(j)} = \Lambda_i^* \lambda_j$ in the discrete case, and $\lambda_{f_i(j)} = \Lambda_i^* + \lambda_j$ in the continuous case. This block structure further implies that $J_i^\dagger J_i$ are block diagonal, and can be written as

$$J_i^\dagger J_i = \sum_j J_{i,j}^\dagger J_{i,j}. \tag{3.11}$$

Given these properties and Eq. (3.4), we obtain the matrix representation

$$\begin{aligned} \mathcal{L}_m^M &= -i \sum_i \left(H_i \otimes I_{f_m(i)} - I_i \otimes H_{f_m(i)}^T \right) + \sum_{i,j} J_{i,j} \otimes J_{i,f_m(j)}^* \\ &\quad - \frac{1}{2} \sum_{i,j} \left[J_{i,j}^\dagger J_{i,j} \otimes I_{f_m(j)} + I_j \otimes J_{i,f_m(j)}^T J_{i,f_m(j)}^* \right], \end{aligned} \tag{3.12}$$

which can be used to efficiently construct blocks of the Lindblad operator after first constructing blocks for the Hamiltonian and jump operators.

Let us demonstrate this for the example of 1D translation invariance discussed above. Supposing we have some initial state with quasi-momentum k

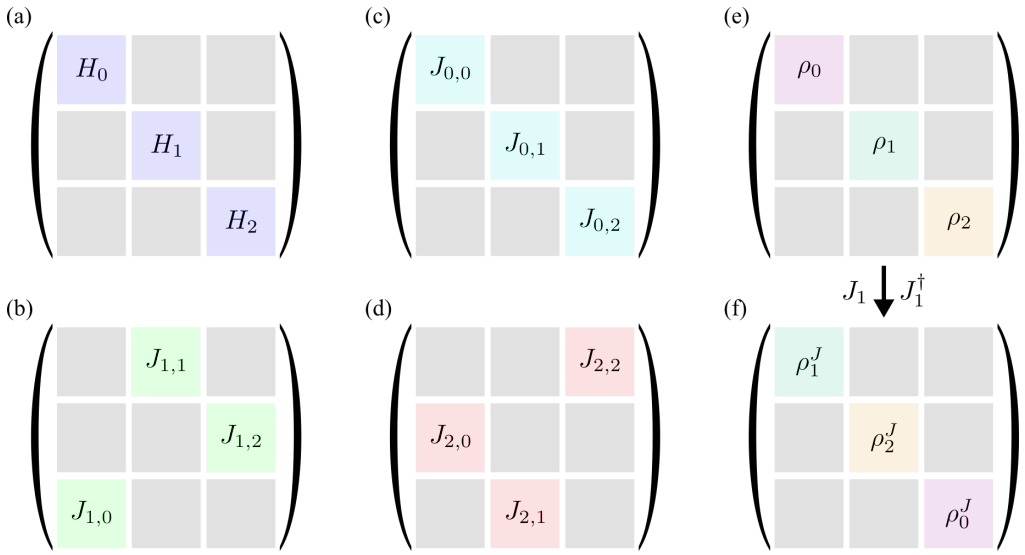


Figure 3.2: (a-d) Sketch of the block structure of the Hamiltonian and jump operators, representative of a three site system with translation invariance. In this case, there is one diagonal jump operator, and two operators which cycle the quasi-momentum up or down by 1. (e,f) A diagonal density matrix ρ (e) is acted on by the jump operator J_1, resulting in a diagonal matrix with blocks $\rho_i^J = J_{1,i}\rho_i J_{1,i}^\dagger$ (f): colours represent which blocks in the original matrix contribute to those in the jumped matrix.

and we act with the jump operator $J_{k'}$, we find simply that

$$\lambda_{f_{k'}(k)} = e^{-2\pi i \frac{k'}{N}} e^{2\pi i \frac{k}{N}} = e^{2\pi i \frac{k-k'}{N}} \tag{3.13}$$

and therefore have $f_{k'}(k) = k - k' \mod N$, i.e. each jump operator shifts the quasi-momentum of the state by an amount indicated by its index. We can then rewrite Eq. (3.12) in terms of the momentum eigenspaces

$$\begin{aligned} \mathcal{L}_m^M &= -i \sum_k \left(H_k \otimes I_{k-m} - I_k \otimes H_{k-m}^T \right) + \sum_{k,k'} J_{k,k'} \otimes J_{k,k'-m}^* \\ &\quad -\frac{1}{2} \sum_{k,k'} \left[J_{k,k'}^\dagger J_{k,k'} \otimes I_{k'-m} + I_{k'} \otimes J_{k,k'-m}^T J_{k,k'-m}^* \right], \end{aligned} \tag{3.14}$$

where the subtractions in the indices are implicitly modulo N.

The effect of the jump terms, those of the form $J_{k,k'} \otimes J_{k,k'-m}^*$, now become transparent: the action of a given term in the sum changes the left quasi-momentum of the density matrix from k' to $k' - k \mod N$, while the right quasi-momentum is changed from $k' - m \mod N$ to $k' - m + k \mod N$, leaving the overall eigenvalue given by the action of $\mathcal{U}$ invariant. Physically, the implication of this is most clear for the block acting on the diagonal of the

density matrix, $m = 0$: given a state with support in a single quasi-momentum eigenspace, action of the jump term shifts the state to a single different quasi-momentum with each application. Quasi-momentum is therefore not conserved, as expected, with time evolution mixing between blocks of the density matrix associated to a given eigenspace of the unitary superoperator, while other terms in Eq. (3.14) mix within each block of the density matrix (see Fig. 3.2 for illustration).

While time evolution of the density matrix, involving a continuously repeated application of this jump term, causes a spread across all diagonal blocks, QJMC only considers single isolated jumps. Consequently, weak symmetries impose almost the same dimensional reduction on QJMC simulations as their counterpart strong versions.

3.4 Symmetry enhanced quantum jump Monte Carlo

As mentioned previously, for a strong symmetry the conserved quantity must not only be constant at the level of a statistical description like the density matrix, but must be conserved within individual trajectories of the system's evolution. In the context of QJMC, given an initial pure state restricted to a single eigenspace of the strong symmetry, we therefore need only ever consider states in this eigenspace. This provides a substantial reduction in the processing and memory requirements of QJMC simulations.

While less straightforward than the case of a strong symmetry, it turns out that an equivalent dimensionality reduction can be achieved for weak symmetries by using the weakly symmetric representation. Due to the block structure of the Hamiltonian and jump operators, any pure initial state with support on a single eigenspace will evolve within that space until a jump occurs. After a jump the state again maintains support on a single eigenspace, however, the state may have transitioned between eigenspaces, analogous to the mixing of density matrices described above. This reduces the maximum Hilbert space dimension required for trajectory simulations to that of the largest eigenspace, providing a substantial computational improvement [27].

More precisely, recall that $J_i^\dagger J_i$ is block diagonal in the weakly symmetric representation. It follows that in this representation the effective Hamiltonian

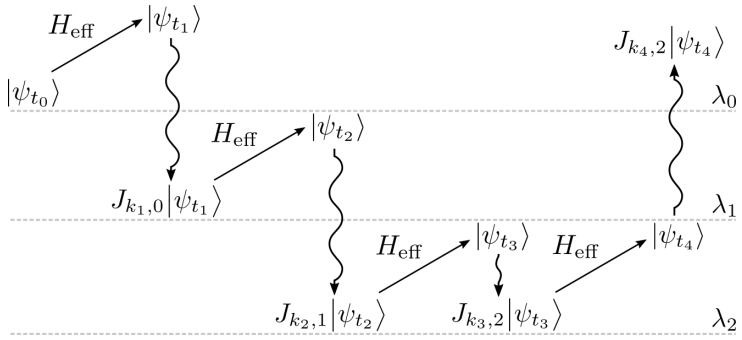


Figure 3.3: Sketch of the symmetrized QJMC algorithm. Jumps between or within eigenspaces are seperated by periods of non-unitary evolution according to blocks of the effective Hamiltonian.

is also block diagonal, with blocks simply given by

$$H_{\text{eff}}^{j} = H_j - \frac{i}{2}\sum_{i=1}^{N} J_{i,j}^{\dagger} J_{i,j}, \tag{3.15}$$

and as such, the non-unitary evolution matrix is also block diagonal. Once the time of the next jump has been determined using these blocks, we must decide which type of jump occurs by calculating the expectation values of operators $J_i^{\dagger} J_i$. Since these are block diagonal, if the pure state $|\psi\rangle$ is restricted to a single eigenspace $\mathcal{H}_j$, the expectations reduce to the expectation of the block $\langle\psi| J_{i,j}^{\dagger} J_{i,j} |\psi\rangle$. Finally, once the jump type i is determined, application of the jump operator J_i results in the mapping of a state in $\mathcal{H}_j$ to a state in $\mathcal{H}_{f_i(j)}$, as discussed earlier.

For clarity, the full modified version of the QJMC algorithm is given below, illustrated in Fig. 3.3. This modification amounts simply to keeping track of the current eigenspace and transitions between eigenspaces when jumps occur.

We initialize by first constructing a set of evolution operators, for the desired time steps and for each subspace

$$U_{k,j} = e^{-i2^{N_U-k}\Delta t H_{\text{eff}}^{j}},\ k \in \{1, ..., N_U\}, \tag{3.16}$$

where N_U is the number of evolution matrices (per eigenspace) and Δt is the smallest step size. Starting from an initial pure state $|\psi(t_0 = 0)\rangle \in \mathcal{H}_{j_0}$ with $i = 0$ we then generate trajectories as follows.

1. Draw a random number r_1 uniformly from $[0, 1]$. Given the current state $|\psi(t_i)\rangle$ following the ith jump, we evolve repeatedly with the largest unitary matrix, finding the first integer value of n such that

$$||U_{1,j_i}^{n} |\psi(t_i)\rangle|| < r_1. \tag{3.17}$$

2. Beginning from the state $|\phi_1\rangle = U_{1,j_i}^{n-1} |\psi(t_i)\rangle$ at time $\tilde{t}_1 = t_i + 2^{N_U-1}(n-1)\Delta t$, with $k = 2$:

   i. Calculate $U_{k,j_i} |\phi_{k-1}\rangle$.

   ii. If $||U_{k,j_i} |\phi_{k-1}\rangle|| < r_1$ set $|\phi_k\rangle = |\phi_{k-1}\rangle$ and $\tilde{t}_k = \tilde{t}_{k-1}$. Else set $|\phi_k\rangle = U_{k,j_i} |\phi_{k-1}\rangle$ and $\tilde{t}_k = \tilde{t}_{k-1} + 2^{N_U-k}\Delta t$.

   iii. If $k = N_U$, set $|\tilde{\psi}(t_{i+1})\rangle = |\phi_k\rangle$ and $t_{i+1} = \tilde{t}_k$. Else increment k and return to step i.

3. Draw another random number $r_2 \in [0, 1]$. Given the time t_{i+1} at which the next jump occurs from step 2, determine the type of the jump by finding the minimum integer value of l such that

$$\frac{\sum_{k=1}^{l} \langle\tilde{\psi}(t_{i+1})| J_{k,j_i}^\dagger J_{k,j_i} |\tilde{\psi}(t_{i+1})\rangle}{\sum_k \langle\tilde{\psi}(t_{i+1})| J_{k,j_i}^\dagger J_{k,j_i} |\tilde{\psi}(t_{i+1})\rangle} > r_2. \tag{3.18}$$

4. Given the index l of the applied jump from step 3, apply the jump to the state and normalize to find the post-jump state

$$|\psi(t_{i+1})\rangle = \frac{J_{l,j_0} |\tilde{\psi}(t_{i+1})\rangle}{\sqrt{\langle\tilde{\psi}(t_{i+1})| J_{l,j_0}^\dagger J_{l,j_0} |\tilde{\psi}(t_{i+1})\rangle}}, \tag{3.19}$$

   and update the eigenspace index to $j_{i+1} = f_l(j_i)$.

5. Return to step 1 until the desired condition to end a trajectory is reached.

Chapter 4

Metastability in an open quantum Ising model

With continuing advances in the control of experimental platforms used as quantum simulators, such as ultracold atomic gases, Rydberg atoms and circuit quantum-electrodynamics [28–34], a plethora of nonequilibrium phenomena of open many-body quantum systems have been observed. Theoretical studies have been achieved via the union of techniques developed for atomic-optics and condensed matter systems, giving rise to many-body adaptations of quantum jump Monte Carlo simulations [24], field theoretical methods [35–37], tensor network simulations [38], and many others.

One question of interest addressed by theoretical studies of non-equilibrium open many-body quantum systems has been the understanding of the phase structure of the stationary state, given the possibility that these systems display phase transitions—singular changes in the stationary state in the limit of large system size—which may be distinct from those of equilibrium systems. The aim of many such studies has been to characterise the phase structure of non-equilibrium steady states via static order parameters, such as the magnetisation in spin systems, and spatial correlation functions more generally, see e.g. [35–37]. However, even in the case where such transitions are not present, the dynamics of these systems can be very rich and cooperative. One way to uncover this dynamical complexity is via large-deviation methods (such as the so-called "thermodynamics of trajectories", see e.g. [39, 40], or the related full-counting statistics, see e.g. [41]), which allow to define and characterise dynamical phases where order parameters are dynamic time-integrated observables, such as the total count of emissions into the environment.

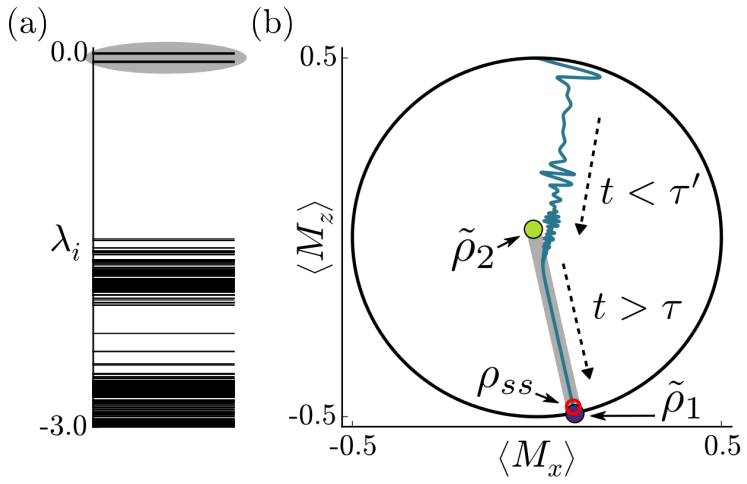


Figure 4.1: (a) Real part of the spectrum of the master operator of the open quantum Ising model defined in Sec. 4.2, for size $N = 7$, with spin interaction $V/\kappa = 250$ and transverse field $\Omega/\kappa = 50$, where κ is decay rate. Spectrum is plotted in units of κ. The two eigenvalues with largest real parts, $\lambda_{1,2}$, highlighted in grey, correspond to the only eigenmodes that contribute to the dynamics at long times. The large gap to the next eigenvalue, λ_3, causes metastability in the dynamics. (b) The metastable manifold (MM) induced by the spectral structure of (a). System states are represented by the average total magnetisation per spin in the x and z directions. The MM (grey line) is bounded by two extreme metastable states $\tilde{\rho}_1$ (purple dot) and $\tilde{\rho}_2$ (green dot). The evolution from an initial state $\rho_\uparrow$ of all spins up (blue curve), undergoes a fast evolution for $t \ll \tau' = -1/\lambda_3$ onto the MM. After a long period of apparent stationarity ($\tau' \ll t \ll \tau = -1/\lambda_2$), the states on the MM evolve towards the true stationary state $\rho_{\rm ss}$ (red circle) for $t \gg \tau$.

In this chapter we focus on a different aspect of open quantum many-body systems, that of *metastability* of the dynamics. As discussed in Sec. 2.1.3, metastability is a characteristic feature of the dynamics of slow relaxing systems, namely, the partial relaxation into long-lived states before eventual decay to the true stationary state: a consequence of separate timescales in the dynamics. In such systems the transient dynamics will appear non-ergodic, in the sense that different initial conditions will relax to different metastable states, before ergodicity is eventually restored. Recall that in classical systems, metastable behaviour typically occurs in two distinct situations: one is in the dynamics near a (usually first-order) static phase transition [13], as discussed in Sec. 2.1.3, where metastable dynamics is intimately related to the existence of static phases; the second one is in glass forming systems [42] where metastable

behaviour is not obviously related to any static features, an example of which we will see in Chap. 5 (see e.g. [43] for various viewpoints on this issue).

Here we focus on the first instance above for the case of a many-body quantum system subject to dissipation where metastability can be traced back to distinct features of its stationary properties, a transverse field Ising model with on-site dissipative decay [3, 37, 38, 44–49]. We study the dynamics of this model by means of a recent theory for metastability in open quantum systems [2]. This new approach is a generalisation to open quantum systems, evolving according to a Lindblad master equation [20, 21], of the method of Refs. [1, 14–16, 50] for classical Markovian systems. This approach relies on the fact that metastable behaviour necessarily results from a separation of eigenmodes in the spectrum of the master operator generating the dynamics, as demonstrated classically in Sec. 2.1.3, thus allowing one to investigate both the structure of the metastable states and the long-time dynamics of the system using a reduced number of parameters [2, 51]. The metastable states form a metastable manifold (MM), a convex subset of the system states (see Fig. 4.1, details in Sec. 4.1) on which the long-time dynamics takes place [2]. In Ref. [2] this approach was applied to few-body models more related to problems in quantum information; here, we demonstrate the effectiveness of this approach for a many-body system where metastability emerges cooperatively with increasing system size. At moderate system sizes, the dissipative Ising model we consider is also of particular interest as it can be realised experimentally through the use of Rydberg atoms in optical lattices [3, 44]. Another realization may be possible using circuit QED [45], systems which are intrinsically open, however, it may be difficult to control the exact nature of the interaction with the environment.

Previous work [3] on the dissipative quantum Ising model suggested a bistable character to the stationary state of this system. Within a mean-field approximation [3] this model has a region of its parameter space in which it exhibits a strict first-order coexistence, terminating at a critical point, between ferromagnetic and paramagnetic steady states. Related to this, dynamics of this model in one dimension for finite size was shown to display pronounced intermittency between periods of photon emission activity and inactivity in quantum jump trajectories [3]. While the mean-field approximation is not necessarily expected to be accurate even in the thermodynamic limit in one-dimension [37, 46, 47], it does provide an idea of the basic phase structure of the model. Mean field bistability often provides a signature for metastability, with

eventual relaxation amongst the mean field stationary states lost as a result of discarding noise in the approximations; as discussed in Sec. 2.1.3, the presence of intermittence is also a typical signature of metastability. Using the methods of [2] we demonstrate the relation between the ferromagnetic/paramagnetic states that mean-field suggests are the metastable states of the dynamics of the dissipative quantum Ising model at finite size. We show that these metastable states are reached by short time dynamics in a way that is dependent on the initial state (i.e., apparent but transient non-ergodicity). We further show that the long-time, ergodicity restoring evolution within the MM is that of an effective classical stochastic dynamics, even though the underlying many-body system features quantum effects. This is in line with recent field-theoretic studies of open spin lattices, which show the long time properties of similar models are often classical [36, 37].

The chapter is organized as follows. In Sec. 4.1 we briefly review the spectral approach to metastability in open quantum systems, along with the effective long-time description, giving a particular focus to the case when the MM is one-dimensional as is the case for the dissipative quantum Ising model. Section 4.2 is the central, providing an in-depth analysis of metastability in the model. We begin in Subsec. 4.2.1 by returning to the mean-field approach used in [3], but focusing on time-evolution instead of only steady state(s), and discussing the effect of neglecting fluctuations from spatial correlations. We then apply the spectral approach of Ref. [2] to the exact model of $N = 7$ spins, and find a parameter regime where the system is metastable (Subsec. 4.2.2). This is followed by characterisation of the MM in terms of the properties of metastable phases (Subsec. 4.2.3). In Subsec. 4.2.4 we show how metastability can be observed in the behaviour of expectation values and autocorrelations of system observables. Finally, we demonstrate how the metastability in the spin magnetisation and the effective dynamics within the MM manifests in individual realisations of the system evolution through intermittency in activity of quantum trajectories (Subsec. 4.2.5).

4.1 Metastable manifolds and effective evolution

In this section we review the theory for metastability in open quantum systems with Markovian dynamics introduced recently in Ref. [2]. This theory is a

natural extension of the spectral approach described in Sec. 2.1.3 for systems determined by the classical Markov generators introduced in Sec. 2.1.1, to systems evolving according to the Lindblad equation discussed in Sec. 2.2.1.

Recall the Lindblad equation Eq. (2.24), and the spectral theory of its generator Eq. (2.25) in terms of left and right eigenmatrices. We assume there is a large separation in the values of the real parts of the eigenvalues, $|\mathrm{Re}(\lambda_m)| \ll |\mathrm{Re}(\lambda_{m+1})|$, cf. Fig. 4.1, and denote the corresponding time scales by $\tau = -1/\mathrm{Re}(\lambda_m)$ and $\tau' = -1/\mathrm{Re}(\lambda_{m+1})$. If we consider times $t \gg \tau'$ then we may neglect terms beyond the m-th in the sum in Eq. (2.33), and for $t \ll \tau$, we also have $e^{t\lambda_k} \approx 1$ for $k \leq m$; this reduced expansion defines the metastable states of the system, see Fig. 4.1. Thus, the projection $\mathcal{P}$ onto the MM is given by $\mathcal{P}\rho = \mathrm{Tr}(\rho)\rho_{\mathrm{ss}} + \sum_{k=2}^{m} c_k R_k$, with $c_k = \mathrm{Tr}(L_k^\dagger \rho)$. This MM is determined by a subset in $\mathbb{R}^{m-1}$ given by the coefficients $\{c_k\}_{k=1}^m$, whose values are bounded by the maximum and minimum eigenvalues of the relevant left eigenmatrices; long time dynamics essentially takes place only inside this bounded, $m-1$ dimensional space, and is effectively generated by projection of the master operator on the MM, $\mathcal{L}_{\mathrm{eff}} = \mathcal{P}\mathcal{L}\mathcal{P}$.

4.1.1 Metastable manifold

The general structure for MMs is discussed in [2]. We will see in Sec. 4.2.2 that for the open quantum Ising model the MM is 1-dimensional, that is, $m = 2$, which is the case we now restrict to. The basis for the MM is given by ρ_{ss} and R_2, but R_2 lacks interpretation as a state of the system since $\mathrm{Tr}(R_2) = 0$ due to trace-preserving dynamics. Instead, we can make use of the convexity of the MM (inherited from the convexity of the full space of density matrices) to consider metastable states as a linear combination of the states at either end of the MM, which we call *extreme metastable states* (eMSs) [2],

$$\tilde{\rho}_1 = \rho_{\mathrm{ss}} + c_2^{\max} R_2, \tag{4.1}$$

$$\tilde{\rho}_2 = \rho_{\mathrm{ss}} + c_2^{\min} R_2, \tag{4.2}$$

where $c_2^{\max}$ and $c_2^{\min}$ are the maximum and minimum eigenvalues of the hermitian L_2, respectively.

Expanding the projection in this basis, $\mathcal{P}\rho = p_1\tilde{\rho}_1 + p_2\tilde{\rho}_2$, and using $p_1 = 1 - p_2$ (from convexity of the MM), the coeffcients $p_{1,2}$ are given by the

expectation values of the observables

$$\tilde{P}_1 = (L_2 - c_2^{\min} I)/\Delta c_2, \tag{4.3}$$

$$\tilde{P}_2 = (-L_2 + c_2^{\max} I)/\Delta c_2, \tag{4.4}$$

where $\Delta c_2 = c_2^{\max} - c_2^{\min}$. These expectations are positive by construction, $p_{1,2} \geq 0$, leading to the interpretation of any state on the MM as a probabilistic mixture of the two eMSs. Thus, all metastable states can be understood by analysing the properties of the two metastable phases $\tilde{\rho}_1$ and $\tilde{\rho}_2$, as done in Sec. 4.2.3.

4.1.2 Effective dynamics within metastable manifold

The evolution for times $t \gg \tau$ effectively takes place on the metastable manifold towards the steady state [2]. The generator of this evolution, $\mathcal{L}_{\text{eff}} = \mathcal{P}\mathcal{L}\mathcal{P}$, can be now expressed in the basis of the eMSs, cf. Eqs. (4.1-4.4), as

$$\mathcal{L}_{\text{eff}} = \frac{-\lambda_2}{\Delta c_2} \begin{pmatrix} -c_2^{\max} & -c_2^{\min} \\ c_2^{\max} & c_2^{\min} \end{pmatrix}, \tag{4.5}$$

yielding the dynamics of the probabilites p_1, p_2 as $d\mathbf{p}/dt = \mathcal{L}_{\text{eff}}\,\mathbf{p}$, where $\mathbf{p}^T = (p_1, p_2)$. Note that the entries in each column of $\mathcal{L}_{\text{eff}}$ add to 0, as expected for probability conservation. Moreover, since $\lambda_2 < 0$ and $c_2^{\max} > 0$, $c_2^{\min} \leq 0$ [as $\text{Tr}(L_2^\dagger \rho_{\text{ss}}) = 0$ by orthogonality of eigenmodes], the diagonal elements are negative and the off-diagonal positive, which ensures positivity of the dynamics. Thus, $\mathcal{L}_{\text{eff}}$ is a generator of classical stochastic dynamics between two metastable phases, $\tilde{\rho}_1$ and $\tilde{\rho}_2$.

Note that the dynamics induced by $\mathcal{L}_{\text{eff}}$ between $\tilde{\rho}_1$ and $\tilde{\rho}_2$ satisfies detailed balance: this suggests the coarse grained dynamics viewed on large timescales appears to be in equilibrium, despite an underlying non-equilibrium dynamics. The transition time from a metastable phase is given by the inverse of the diagonal entry, e.g. $(-c_2^{\max}\lambda_2)^{-1} = \tau\,(c_2^{\max})^{-1}$ for $\tilde{\rho}_1$; the ratio of stationary probabilities is determined by the ratio of the off-diagonal terms, $-c_2^{\min}/c_2^{\max}$, independent from τ, as expected since transition rates between phases are given relative to the metastable timescale.

4.1.3 Observation of metastability

Metastability of the system dynamics can be seen in the behaviour of expectation values and autocorrelations of system observables [2, 52]; in Sec. 4.2.4 we

focus on measuring a given spin magnetisation (or equivalently the probability distribution of the magnetisation). The long-time statistics of these observables should be effectively captured by the effective long-time description of Eq. (4.5): for the expectation value of an observable O we arrive at

$$\langle O(t)\rangle \approx \mathbf{o}^T\,\mathbf{p}(t), \tag{4.6}$$

in terms of the expectations of the observable in each metastable phase, $\mathbf{o}_i = \mathrm{Tr}(O\tilde{\rho}_i)$.

Observation of metastability in the expectation value requires preparation of an initial system state different from the steady state. When this is difficult to achieve experimentally, metastability can be found in the time-autocorrelation of measurements for a system observable initiated in the stationary state. When time between measurements is greater than τ', the state conditioned on the initial measurement relaxes into the MM and

$$\begin{aligned} C(t) &= \langle O(t)O(0)\rangle = \mathrm{Tr}(Oe^{t\mathcal{L}}\mathcal{O}\rho_{\mathrm{ss}}) \\ &\approx \mathrm{Tr}(Oe^{t\mathcal{L}_{\mathrm{eff}}}\mathcal{P}\mathcal{O}\rho_{\mathrm{ss}}), \end{aligned} \tag{4.7}$$

where $\mathcal{O}$ is the superoperator representing measurement of the observable O. As $\mathcal{P}\rho_{\mathrm{ss}} = \rho_{\mathrm{ss}}$, we have

$$C(t) \approx \mathbf{o}^T\, e^{t\mathcal{L}_{\mathrm{eff}}}\,\mathbf{O}\,\mathbf{p}_{\mathrm{ss}}, \tag{4.8}$$

where $\mathbf{O}_{ij} = (\mathcal{P}\mathcal{O}\mathcal{P})_{ij} = \mathrm{Tr}[\tilde{P}_i\mathcal{O}(\tilde{\rho}_j)]$ and $\mathbf{p}_{\mathrm{ss}}^T = (-c_2^{\min}/\Delta c_2, c_2^{\max}/\Delta c_2)$ is the stationary probability of ρ_{ss} between the metastable phases. The components $\mathbf{O}_{ij}$ may be interpreted as the observable expectation in the phase $\tilde{\rho}_j$, multiplied by the probability of being in the phase $\tilde{\rho}_i$ at much later times.

4.2 Open quantum Ising model

We now apply the theory [2] reviewed in the previous section to a dissipative quantum many-body system, an open version of the 1D transverse field Ising model, consisting of a chain of N spin-1/2 particles with periodic boundary conditions coupled to a external bath. The Hamiltonian is given by

$$H = \Omega\sum_{j=1}^{N} S_x^{(j)} + V\sum_{j=1}^{N} S_z^{(j)}S_z^{(j+1)}, \tag{4.9}$$

where Ω describes the transverse magnetic field and V the interaction between neighbouring spins. The spin operators $S_\alpha^{(j)} = \frac{1}{2}\sigma_\alpha^{(j)}$, where $\alpha = \{x, y, z\}$. The

jump operators mediating interactions between the bath and individual spins are

$$J_j = \sqrt{\kappa}\, S_-^{(j)} = \sqrt{\kappa}\,(S_x^{(j)} - iS_y^{(j)}), \tag{4.10}$$

where the decay rate κ is determined by strength of system-bath coupling, and $j = 1, ..., N$. This system can be realized using Rydberg atoms [44, 53], in which case the jumps can be seen to be photon emissions from individual spins into the environment. The properties of these jump operators imply that the system dynamics are irreducible and the stationary state unique for all finite N [54].

The order parameters we will consider are the magnetisations along each axis,

$$M_\alpha = \frac{1}{N}\sum_{j=1}^{N} S_\alpha^{(j)}. \tag{4.11}$$

We will find in Sec. 4.2.4 and Sec. 4.2.5 that the z component of the magnetisation in particular is sufficient to highlight metastable dynamics in this system.

4.2.1 Time dependent mean-field approximation

We start our analysis by returning to the mean-field approximation studied previously in [3], this time however focusing on the dynamics rather than just the steady state. From the study of classical systems it is common for such an approach to qualitatively give the short time dynamics leading to the MM, since often long-time relaxation is non-perturbative and triggered by spatial fluctuations that are dismissed at the mean-field level, see e.g. [42]. We therefore expect this approximation to uncover properties of the exact dynamics for the approach to the metastable regime ($t \ll \tau$). In later subsections we consider the whole dynamical regime by analysing the full spectral properties of the exact problem.

In this subsection we proceed as follows: we consider an approximation of the density matrix in the form of an arbitrary product state, i.e $\rho_N = {\rho_1}^{\otimes N}$, where $\rho_1 = \frac{1}{2}\mathbb{1} + xS_x + yS_y + zS_z$. Note that here $x, y, z = \langle M_x\rangle, \langle M_y\rangle, \langle M_z\rangle$. These coefficients are time dependent, and we substitute this into the master operator, proceeding to trace out all but one spin, i.e. $d\rho_1/dt = \mathrm{Tr}_{2,...,N}[\mathcal{L}(\rho)]$. This process gives a set of three non-linear differential equations on the coefficients

given by

$$\begin{aligned} \dot{x} &= -\frac{\kappa}{2}x - 2Vyz, \\ \dot{y} &= -\frac{\kappa}{2}y + 2Vxz - \Omega z, \\ \dot{z} &= -\frac{\kappa}{2}(1+2z) + \Omega y. \end{aligned} \tag{4.12}$$

The dynamics induced by these equations is highly oscillatory, with rotations about the x-axis induced by the transverse field Ω, see Fig. 4.2(a), and rotations about the z-axis—weighted by the magnetisation $\langle M_z \rangle$, thus no rotation in the $z = 0$ plane, Fig. 4.2(c)—due to the spin-spin interaction with potential V. These oscillations are eventually damped by the decaying terms proportional to κ.

Stationary solutions. The steady states of this system of equations are found from the solution of $\dot{x} = 0$, $\dot{y} = 0$ and $\dot{z} = 0$, which gives rise to a 3rd order polynomial in z, see [3]. There is either one or two stable real solutions depending on the parameters chosen, with the set of parameters giving bistable dynamics lying between two "spinodal" lines, see Fig. 4.2(g). Outside this region the unique stationary state is ferromagnetic ($z \approx -0.5$) for small Ω and close to paramagnetic (x, y, z small) for large Ω; inside, one of the two stationary states corresponds to a paramagnetic state while the other transitions smoothly from ferromagnetic to paramagnetic with increasing Ω. The two steady states for specific parameters are shown on the flow diagrams in Fig. 4.2(a-c).

Asymptotic evolution. Since the mean-field approach is expected to capture the short time evolution we anticipate the two steady states to be qualitatively similar in properties to the eMS of the exact model. In order to compare the mean-field approximation with the exact dynamics during the metastable regime, we investigate the average asymptotic magnetisation, $\overline{m}_\infty$, reached from pure initial states ρ_1 sampled uniformly from the Bloch sphere, Fig. 4.2(g): i.e., the average magnetisation of the steady state reached according to Eq. (4.12) (see also [55]). Outside of the bistable regime this is simply the magnetisation of the unique mean-field steady state, m_{ss}. Within the bistable regime, $\overline{m}_\infty$ is the linear combination obtained from adding up the area of the basins of attraction for the two mean-field steady states, Figs. 4.2(d-f), multiplied by their respective magnetisations.

For low Ω the basins are fairly even in size, giving a sharp transition at the left spinoidal line from $m_{\text{ss}} \approx -0.5$ of the unique ferromagnetic steady state

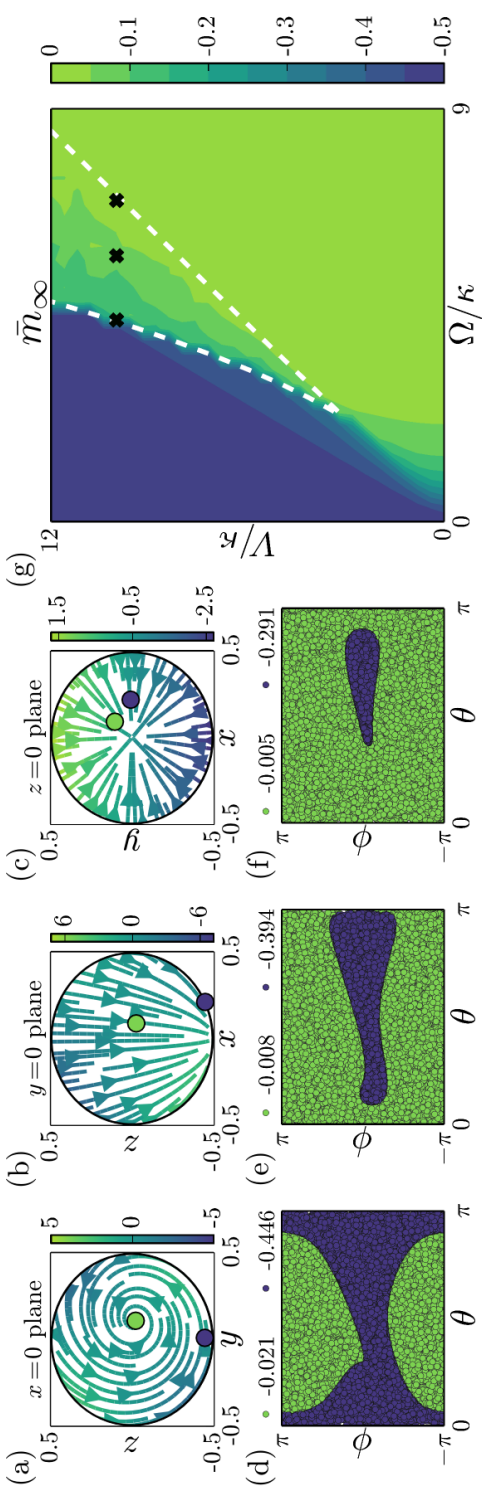


Figure 4.2: (a-c) Flow induced on cross sections of the Bloch ball by the dynamics in Eq. (4.12), for parameters $V/\kappa = 10$, $\Omega/\kappa = 4.4$ where the system is bistable. The colour of the line indicates the magnitude of the component perpendicular to the plane. The green and purple dots correspond to the two stationary solutions of the mean-field approximation projected onto the planes through the Bloch sphere. (d-f) Basins of attraction of the two mean-field stationary solutions, with the indicated values of $\langle M_z \rangle$, at three points in the bistable regime with parameters $V/\kappa = 10$ and $\Omega/\kappa = 4.4, 5.8, 7.0$, respectively, marked by black crosses in panel (g). (g) Mean-field phase diagram: $\bar{m}_\infty$, as a function of model parameters. Spinodal lines separating one-solution from two-solution regions are indicated by white dashed lines.

to $\overline{m}_\infty \approx -0.25$, cf. Fig. 4.2(d-f). As Ω increases the area of the basin for the steady state with a lower magnetisation shrinks continuously, along with the magnetisation of this state increasing, with the area of the basin vanishing at the right spinoidal line, leading to a smooth increase of $\overline{m}_\infty$ to $m_{\rm ss} \approx 0$. Confirming the relation between the mean field dynamics and the exact evolution, we will later see that the magnetisation, averaged over a uniform distribution of initial density matrices, behaves during the metastable regime in a similar way to the mean-field results above.

4.2.2 Spectral analysis of the master operator

Next we explore how the features of the mean-field treatment manifest in the exact master equation dynamics. To this end, consider numerically a system with $N = 7$ spins: we make use of translation invariance to first block diagonalize the master operator, as discussed in Sec. 3.3, specifically (3.14). Note we find both λ_2 and λ_3 to be real and thus drop the use of $\mathrm{Re}(\lambda_i)$.

For metastability we require separation in the real part of the spectrum of the Lindbladian, and we find that for this system that a large gap occurs between the second and third eigenvalues, so that $m = 2$ and the metastable manifold is 1D, see Figs. 4.1(a) and 4.3(b). The parameter region of metastable dynamics—light yellow wedge in Fig. 4.3(a)—is suggestive of identification with the bistable region of the mean-field approximation, cf. Fig. 4.2(g), with a stretching to lower values of the transverse field. The separation in the spectrum is mainly due to the the spectral gap, $-\lambda_2$, shrinking, Fig. 4.3(b,c), while the third eigenvalue remains approximately constant. Metastability in the dissipative Ising model is a collective phenomenon, since the ratio λ_3/λ_2 increases with size, as does the inverse of the gap $-1/\lambda_2$, see Fig. 4.3(d).

It remains an open question whether the gap strictly closes for some combination of parameters in the thermodynamic limit, as in the mean-field approximation. This would correspond to a phase transition in the stationary state of the system. What the mean-field approximation predicts is that this would be a transition between phases of different magnetisation, cf. the states at either side of the bistable region, Fig. 4.2(g). Irrespective of whether there is a true transition in the thermodynamic limit, or a smooth but sharp crossover, the decrease of the gap with increasing size, Fig. 4.3(d), indicates that metastability is a consequence of the proximity to this transition/crossover point; the system sizes accessible to numerics are far from large, therefore precluding a

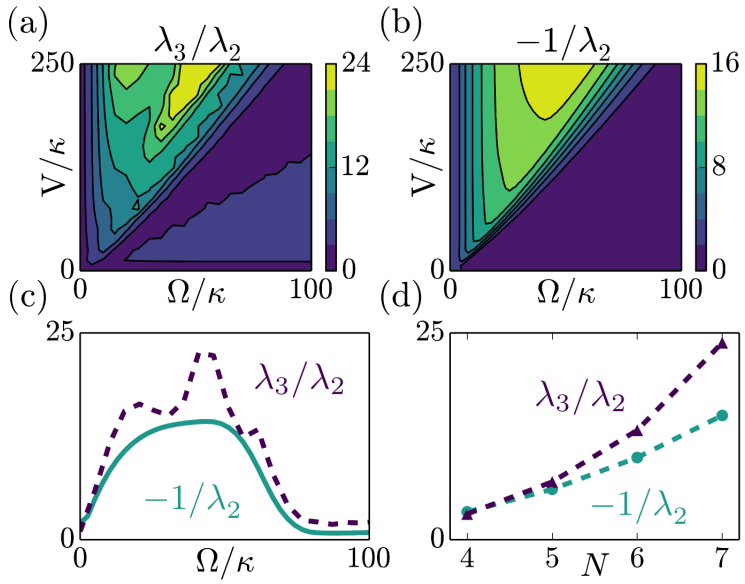


Figure 4.3: (a) The ratio of the real parts of the second and third eigenvalues λ_3/λ_2, plotted over a region of the parameter space $0 \leq V \leq 250$ and $0 \leq \Omega \leq 100$. (b) The inverse gap $-1/\lambda_2$ plotted over the same region. (c) A cross section of plots (a) and (b) for $V = 200$. The dashed (purple) line is the ratio while the solid (blue) line is the inverse gap. (d) The scaling of the maximum value of the ratio (purple triangles) and inverse gap (blue circles) in this range of parameters with system size.

singular transition. Dependence on size, however, indicates that such a change (whether a transition or sharp crossover) in the steady state magnetisation, $m_{\text{ss}} = \text{Tr}(M_z\rho_{\text{ss}})$, from the ferromagnetic state at small Ω, $m_{\text{ss}} \approx -1/2$, to the paramagnetic one at large Ω, $m_{\text{ss}} \approx \text{Tr}(M_x\rho_{\text{ss}}) \approx \text{Tr}(M_y\rho_{\text{ss}}) \approx 0$, should become very pronounced at large sizes. See Fig. 4.4(a).

4.2.3 Characterization of the metastable manifold

The metastable manifold in this region can be characterised by the properties of two eMSs defined by Eqs. (4.1,4.2), which we investigate below. These two eMSs correspond to ferromagnetic ($m_1 \approx -0.5$) and paramagnetic ($m_2 \approx 0$) states, see Fig. 4.4(c-d). Note that the values of m_1 and m_2 resemble the magnetisations of two stationary states in the mean-field approximation, cf. Fig. 4.2(d-f).

We consider now the behaviour of the magnetisation in z-direction, $\langle M_z\rangle$, during the metastable regime taken on average by pure initial states $|\psi\rangle$, see Fig. 4.4(b), i.e. $\overline{m} = \overline{\text{Tr}(M_z\mathcal{P}|\psi\rangle\langle\psi|)}$, where the bar denotes average w.r.t.

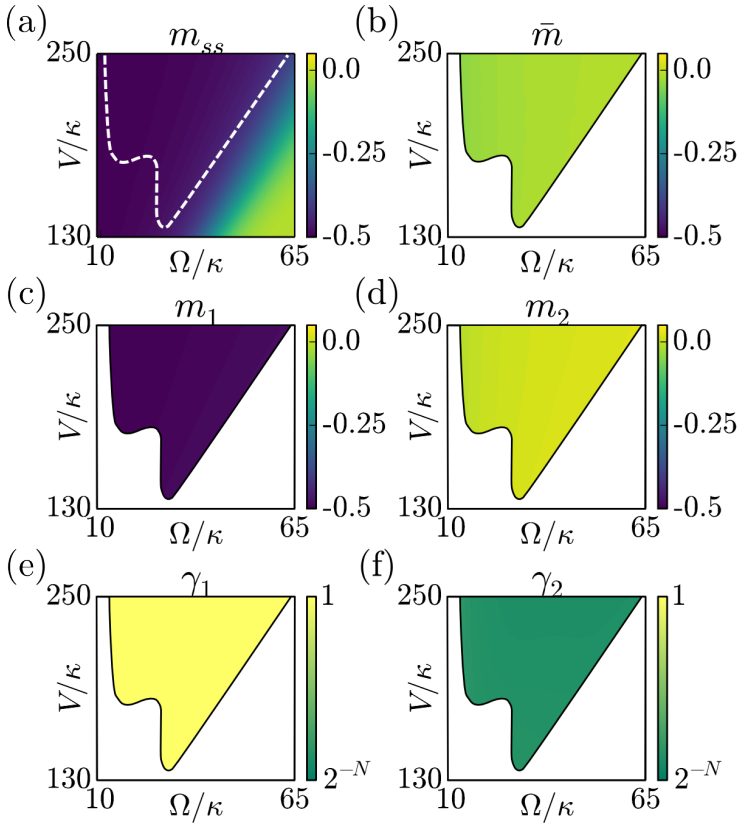


Figure 4.4: (a) Magnetisation of the steady state m_{ss}. The approximate boundary of the metastable region is indicated by the dashed white line. (b) The average z magnetisation $\overline{m}$ in the metastable regime. In this and the following panels we only show the area where metastability holds. (c-d) Expected z magnetisations $m_i = \text{Tr}(M_z\tilde{\rho}_i)$ and (e-f) purities $\gamma_i = \text{Tr}(\tilde{\rho}_i^2)$ of the two metastable phases.

uniform sampling of $|\psi\rangle$. For most of the parameter regime where metastability is present we have $\overline{m} \approx 0$, with a transition at small Ω; this is analogous to $\overline{m}_\infty$ in the mean-field case, cf. Fig. 4.2(g). Here the size of the basins of attraction (given by $\frac{1}{N}\text{Tr}\tilde{P}_1$ and $\frac{1}{N}\text{Tr}\tilde{P}_2$, respectively) are imbalanced towards the paramagnetic phase for almost all of the metastable region, with a slight increase in area of the ferromagnetic phase at smaller fields: this behaviour is the same as that of the mean-field, suggesting the approximation captures the phenomenology of both the metastable phases and their basins of attraction.

Note the contrast between the transition in $\overline{m}$ to the behaviour of the magnetisation m_{ss} of the steady state, cf. Fig. 4.4(a), which takes place for large Ω, outside the metastable parameter region. For the parameters where metastability is present, ρ_{ss} consists mostly of the ferromagnetic phase, $p_1^{\text{ss}} \approx 1$. This shows that the short time evolution leads on average to the vast majority

of initial states evolving to the paramagnetic metastable phase on short time scales, while at longer times they decay into the mostly ferromagnetic stationary state.

The two metastable phases differ also in purity $\gamma = \mathrm{Tr}(\rho^2)$, see Fig. 4.4(e-f), with the ferromagnetic phase being almost pure ($\gamma_1 \approx 1$), in contrast the paramagnetic one almost completely mixed ($\gamma_2 \approx 1/2^N$). This is a consequence of the two phases corresponding respectively to inactive and active periods in the photon emission records [3]. The fluctuations in photon emissions per unit time for the system in the paramagnetic phase cause it to be a mixture of many different pure states: the large number of jumps causes these periods in the trajectories to consist of many different states; in contrast, the relative inactivity of the ferromagnetic phases leaves the state approximately pure. The relation of the metastable phases to activity in quantum trajectories is further studied in Sec. 4.2.5.

4.2.4 Expectations, correlations and effective low-dimensional dynamics

After the initial relaxation, the system state is approximately stationary during the metastable regime, before eventual relaxation into the steady state. As discussed in Sec. 4.1.3, metastability can be observed in the two-step decay of the expectation value $\langle O(t)\rangle$ and two-time correlation function $\langle O(t)O(0)\rangle$ of an observable O measured on the system; here, we demonstrate that this is indeed the case when the observable is the magnetisation M_z, Eq. (4.11).

Expectation. We consider dynamics of two initial states: the "all up" state $\rho_\uparrow = (|\uparrow\rangle\langle\uparrow|)^{\otimes N}$, where $\sigma_z|\uparrow\rangle = |\uparrow\rangle$, and the "all right" state $\rho_\rightarrow = (|\rightarrow\rangle\langle\rightarrow|)^{\otimes N}$, where $\sigma_x|\rightarrow\rangle = |\rightarrow\rangle$. The expected values of the z-magnetisation, $\langle M_z(t)\rangle$, show a plateau in the metastable regime ($\tau' < t < \tau$), see Fig. 4.5(a-b), when the initial states evolve into mixtures of metastable phases, Fig. 4.5(e). Subsequent evolution takes the magnetisation to that of the mostly ferromagnetic stationary state at later times ($t > \tau$). Meanwhile, the expected value of the x-magnetisation, $\langle M_x\rangle$, Fig. 4.5(c-d), displays oscillations for times $t < \tau'$ suggestive of those present in mean-field model, cf. Fig. 4.2(a-c), which is expected to qualitatively represent the short time dynamics. The long-time behaviour is accurately captured by the effective dynamics $\mathcal{L}_{\text{eff}}$, cf. Eq. (5.18). Both states evolve mostly into a paramagnetic metastable phase $\langle M\rangle \approx 0$, despite being very different initially, $\mathrm{Tr}(\rho_\uparrow\rho_\rightarrow) = 1/2^N$: this demonstrates the

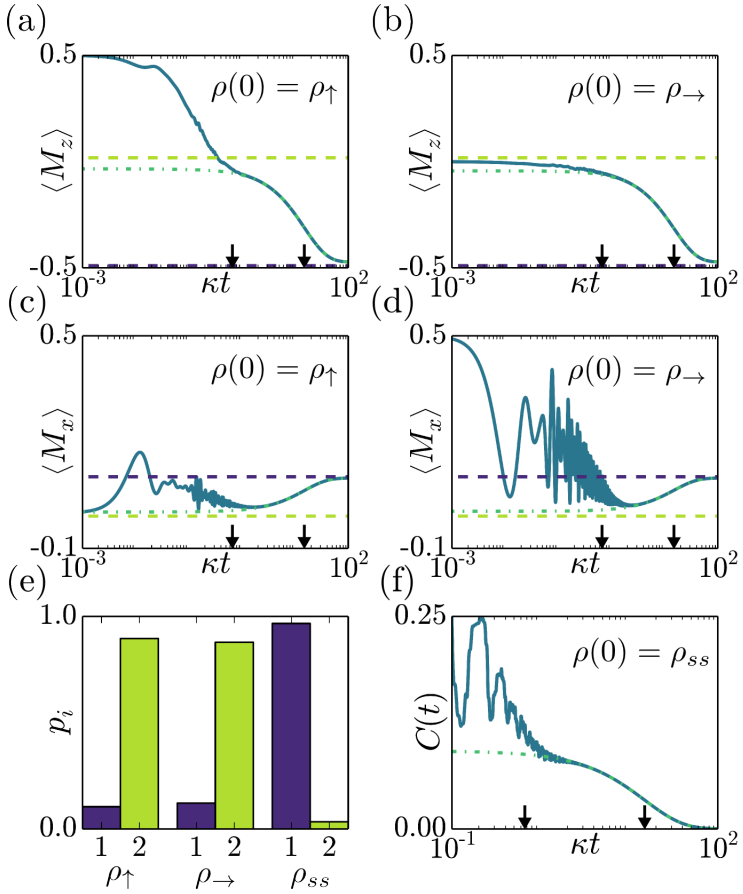


Figure 4.5: Results calculated for parameters of $V/\kappa = 250$ and $\Omega/\kappa = 50$. (a) Time evolution of the average z-magnetisation, $\langle M_z \rangle$ for the initial state $\rho_\uparrow$. The z-magnetisations of the metastable phases $\tilde{\rho}_{1,2}$ are represented by the dashed lines. (b) Same but for the initial state $\rho_\rightarrow$. (c,d) Time evolution of the average x magnetisation, $\langle M_x \rangle$, for $\rho_\uparrow$ and $\rho_\rightarrow$. The average metastable values are given by dashed lines. (e) Histogram of the probability of finding $\rho_\uparrow$, $\rho_\rightarrow$ and ρ_{ss} in each eMS during the metastable regime, see Eq. (4.3), (4.4). (f) Time-averaged autocorrelation function $C(t)$ of the projective measurement related to M_z in ρ_{ss} (see the main text). In panels (a-d,f) the time is in log scale, with the two arrows indicating the time scales τ' and τ. The exact dynamics is plotted as solid curves, and the effective dynamics as dash-dotted lines.

dominance of this metastable phase in the short time evolution, highlighted by the initial state average magnetisation of $\bar{m}$ in Fig. 4.4.

Autocorrelation. Preparing specific initial states can be difficult experimentally; in Fig. 4.5(f) we show how metastability is also observed in the autocorrelation $C(t)$ of a measurement conducted on the steady state ρ_{ss}, see Eq. (4.7). We consider the observable $O = O_1 - O_2$, where O_1 is the sum of projections onto the $M_z = \pm 1/2N$ eigenspaces and $O_2 = |M_z = -1/2\rangle \langle M_z = -1/2|$, so that the average of this observable gives the difference of probabilities of $P(M_z = \pm 1/2N)$ and $P(M = -1/2)$. Non-zero values of the magnetisation are used as N is odd. We choose the correlations of O, which can be obtained from correlations of M_z by post-selection, as they more clearly demonstrate the metastability: these probabilities are each significant in only one of the two eMS. The initial measurement of O perturbs the stationary state out of the metastable manifold; the relaxation towards the MM features large oscillations in the autocorrelation $C(t)$, while relaxation at later times is well described by $\mathcal{L}_{\text{eff}}$ and $C(t)$ is given by Eq. (5.19).

4.2.5 Intermittent dynamics of quantum trajectories

So far we have discussed the dynamics of the system described statistically by the density matrix $\rho(t)$, which is governed by the master operator (2.25), and the related dynamics of observables on the system, such as the spin magnetisation (4.11). We saw in Sec. 2.1.3 that classical metastability in a statistical description is accompanied by intermittence in the model's stochastic trajectories. As in the classical case, one can instead consider quantum trajectories given by an unravelling of the master equation, such as that discussed in Sec. 2.2.2, which corresponds to a particular experimental realisation of system dynamics and a continuous measurement of the environment it is coupled to. In this case, a quantum jump occurs when, say, the system jump operator J_k flips the k-th spin from up-to down, cf. Eq. (4.10), which is accompanied by the emission of a photon into the environment, which can be detected. In this case, a measurement record up to time t consists of information about which spins emitted photons and the emission times, see Fig. 4.6(b-c).

The total number of photons emitted up to time t for dynamics with a unique steady state obeys the Central Limit theorem [56, 57]. Moreover, both the mean and the variance of the total number of emissions asymptotically ($t \gg \tau$) scale linearly in with time t, (for the case of the dissipative Ising

model see [3]); we argue that this also holds in the metastable regime for each of the metastable phases. For times t well inside the metastable regime, the statistics of an observable integrated over time such as the total emission number $\Lambda(t)$ is dominated by the contribution when the system state (averaged over trajectories) is metastable. The total emission number can then be approximated by the instantaneous rate μ of photon emissions from the system in its metastable phases, related to the magnetisation, $\mu = \sum_{j=1}^{N} \mathrm{Tr}(J_j^\dagger J_j \rho) = N\kappa \left(\mathrm{Tr}(M_z \rho) + \frac{1}{2}\right)$ [3]: the mean number of photons emitted in time $\tau' \ll t \ll \tau$ can thus be approximated by $\langle \Lambda(t) \rangle \approx t\, N\, \kappa\, (p_1 m_1 + p_2 m_2 + \frac{1}{2})$.

Consider the case of an initial state evolving into just one of the metastable phases: the mean activity, $k(t) = \Lambda(t)/t$, of trajectories is given by the magnetisation in the corresponding eMS, $\langle k(t) \rangle \approx N\kappa(m_1 + \frac{1}{2})$ or $N\kappa(m_2 + \frac{1}{2})$. To understand the variance of the activity, $\Delta^2 k(t)$, we first look at the variance of the total emissions, $\Delta^2 \Lambda(t)$: this must scale linearly for times t in the metastable regime, since the correlations of dynamics inside a metastable phase can decay at most at times of order τ'. The variance $\Delta^2 k(t)$ is thus inversely proportional to t at metastable timescales. If the metastable regime is long enough, the fluctuations of activity around its mean value, $N\kappa \left(m_{1,2} + \frac{1}{2}\right)$, are small and trajectories can be classified as "active" (large k) or "inactive" (small k). Emission record statistics for many initial states will be a mixture of these active and inactive phases, since they would evolve exactly into a mixture of the two eMSs, $p_1 \tilde{\rho}_1 + p_2 \tilde{\rho}_2$.

Now consider a *coarse graining* in time of the photon emission records, where an emission record is divided into time bins of size t_{bin} and the emission record is replaced by the activity of time bins; it is known that the time-bin activity distribution can be bimodal for intermittent dynamics [3]. From the arguments above it follows that for a t_{bin} well inside a metastable regime that is long enough, the probability distribution of activity is indeed bimodal with inactive dynamics corresponding to magnetisation of the ferromagnetic phase $m_1 \approx -0.5$ and the active dynamics corresponding to the paramagnetic phase $m_2 \approx 0$, which is visible in Fig. 4.6(a). This demonstrates that the periods of active and inactive dynamics (so called dynamical phases [39]) correspond directly to the two metastable phases.

We now discuss the relation between intermittency and the effective dynamics. For times after initial relaxation $t \gg \tau'$ the system dynamics $\rho(t)$ can be obtained as an average over classical trajectories generated by $\mathcal{L}_{\mathrm{eff}}$, (4.5),

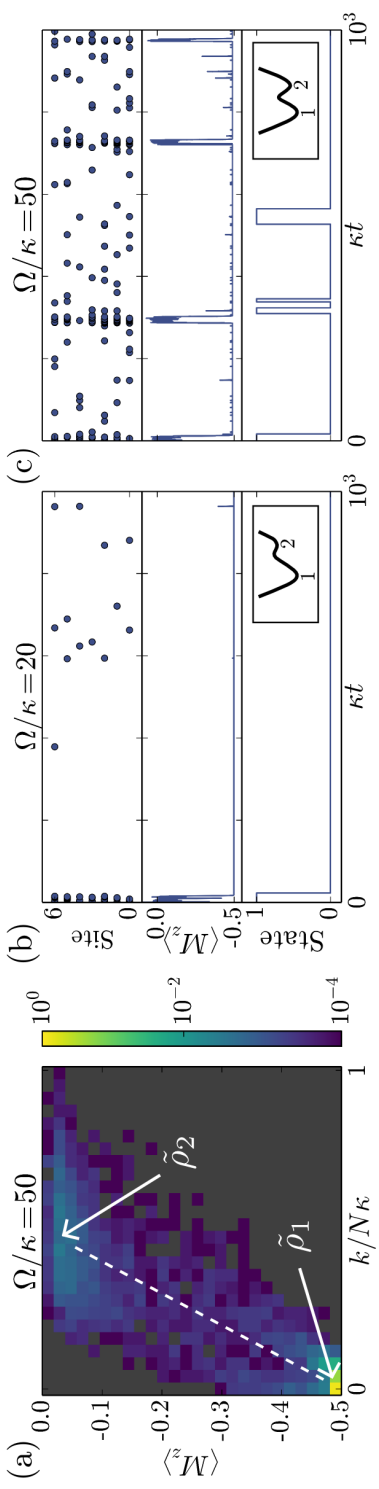


Figure 4.6: (a) A 2d histogram of the average magnetisation m and activity k of time bins of length $t_{\text{bin}} = 6\tau'$, for parameters $V/\kappa = 250$, $\Omega/\kappa = 50$ and $N = 7$. The arrows indicate the expectation values for $\tilde{\rho}_1$ and $\tilde{\rho}_2$ respectively, with the decay $e^{t_{\text{bin}}\lambda_2}$ of R_2 taken into account. The white dashed line indicates the relation $\langle k \rangle / N\kappa = \langle M_z \rangle + \frac{1}{2}$. (b-c) Sample trajectories for two different sets of parameters in the metastable region, $V/\kappa = 250$ with $\Omega/\kappa = 20$, 50, for N=7 and time in linear scale. The first and seconds rows show the space and time resolved photon emissions and the corresponding magnetisation of the state over time respectively, for a sample QJMC trajectory. The third row shows a sample classical trajectory, jumping between the two metastable phases. The insets on the third row show sketches of the double well potentials of free energy leading to analogous classical evolution between the metastable states of two wells.

between two metastable phases. Those classical trajectories are ergodic, i.e. time-averaged state in a trajectory approaches the steady state ρ_{ss} for $t \to \infty$, which requires the ratio of time spent in each of the metastable phases to be given by $p_1^{\mathrm{ss}}/p_2^{\mathrm{ss}} = -c_2^{\mathrm{min}}/c_2^{\mathrm{max}}$, cf. Eq. (4.5). On the other hand, we know that the emission record coarse-grained in time consists of active and inactive periods with small fluctuations. As the activity of a long record approaches the emission rate of the steady state, $\langle k \rangle_{\mathrm{ss}} = \mu_{\mathrm{ss}} = N\kappa(m_{\mathrm{ss}} + \frac{1}{2})$, the probabilities of the inactive and active dynamics are again given (approximately) by p_1^{ss} and p_2^{ss} (see Fig. 4.6(a)). Finally, the average length of active/inactive dynamics in coarse-grained records cannot exceed the longest timescale τ of the model. This yields a direct relation between the classical trajectories and the coarse-grained intermittent emission records, see Fig. 4.6(b-c).

The classical dynamics generated by $\mathcal{L}_{\mathrm{eff}}$ can be related back to the double-well model discussed in Sec. 2.1.3, with the sketches of the relevant double well potential shown in the insets of Fig. 4.6(b-c). The smaller spectral gap $-\lambda_2$ for (c), leads to longer periods spent in two phases, analogous to a higher barrier between the wells, and results in a longer equilibration time. When the difference in probabilities between the metastable phases in ρ_{ss}, $|p_1^{\mathrm{ss}} - p_2^{\mathrm{ss}}| = |c_2^{\mathrm{max}} + c_2^{\mathrm{min}}|/\Delta c_2$, is larger (b) the times spent in the two states differ more, analogously to how the bigger difference in free energies of the two wells makes time spent in the well of higher free energy shorter and hence less of the equilibrium state is supported there.

The average over the ensemble of quantum trajectories also gives the dynamics of the system state $\rho(t)$. It is not generally known, if those trajectories are ergodic, i.e. whether each time-averaged trajectory asymptotically gives the steady state. If that was the case, as the supports of metastable phases are approximately disjoint [2], one could expect the quantum trajectories to be ergodic also inside those supports for $\tau' \ll t \ll \tau$, which would lead to the classical trajectories being coarse-graining of quantum ones. Indeed, one recovers the effective dynamics up to fluctuations within the τ' timescale when considering the magnetisation of quantum trajectories, due to its relation to the photon emission activity, see Fig. 4.6(b-c).

4.3 An aside: phases of dynamical nuclear polarization

Intermittence results in a large variance in the value of observables integrated over long but finite times, a common signature of a phase transition. Here we take a moment to discuss the results of Ref. [58], which used this relationship to justify the existence of a phase transition in a model of dynamical nuclear polarization predicted by mean field theory, through the analysis of the variance of its time-integrated magnetisation across a range of parameters.

The control and detection of magnetization arising from a polarized ensemble of unpaired electron spins forms the basis of electron spin, or paramagnetic, resonance (ESR/EPR): a powerful spectroscopy tool for studying paramagnetic materials placed in a static external magnetic field. The underpinning key principle for this technique is the application of oscillating magnetic fields close to or at the electronic Larmor frequency (usually in the microwave regime) to generate non-equilibrium distributions of populations and coherences between quantum states that lead to detectable signals [59,60]. The evolution of systems of isolated or only weakly coupled paramagnetic centres under the effect of these fields is well understood. A more challenging problem is to predict the response of strongly coupled electron ensembles to such perturbations, particularly in samples in the solid state in which anisotropic components of the electronic interactions are not averaged out by thermal motion. Insight into the dynamics of strongly coupled, microwave driven electronic ensembles is also needed in order to improve our understanding of dynamic nuclear polarization (DNP), which is an out-of-equilibrium technique to enhance the sensitivity of nuclear magnetic resonance (NMR) applications by orders of magnitude (see, e.g., Ref. [61–63]) — in particular, this concerns the cross effect and thermal mixing DNP mechanisms [64–68].

Recently, a strongly interacting electronic ensemble under continuous microwave driving, subject to dissipation to the environment, has been studied using a mean field theory based on a model of its dynamics in terms of a Markovian master equation [58]. This revealed phase transitions between states of high and low electronic polarisation as well as the emergence of a critical point that displays Ising universality [55]. These features are controlled by the distribution of the disordered electronic spin-spin interactions. The uncovered mean-field transitions imply the emergence of metastable states and

accompanying intermittent dynamics [3, 4, 69]. This was confirmed numerically through QJMC simulations of small systems, as we discuss in this chapter: we base this on the relation between intermittence and its associated variance in observables, and the presence of a large variance near phase transitions. These predictions complement those of conventional theoretical approaches, based, e.g., on the so-called *spin-temperature* which, due to their restriction to certain parameter regimes, would only predict a homogenous quasi-equilibrium state [66, 67, 70–74].

4.3.1 Model

We model the evolution of the electron system within the framework of a Markovian Lindblad master equation, see Eq. (2.24). For a system of N electrons, the Hamiltonian H at high static magnetic field, in the rotating frame approximation and in terms of the spin operators as defined for the Ising model above, is given by

$$\begin{aligned} H &= \sum_{k=1}^{N} \left(\omega_1 S_x^{(k)} + \Delta_k S_z^{(k)}\right) + 3 \sum_{k<k'} D_{kk'} S_z^{(k)} S_z^{(k')} \\ &\quad - \sum_{k<k'} D'_{kk'} \mathbf{S}_k \cdot \mathbf{S}_{k'}, \end{aligned} \tag{4.13}$$

where $\mathbf{S}_k = (S_x^{(k)}, S_y^{(k)}, S_z^{(k)})$. Here ω_1 is the strength of the microwave field, Δ_k are the offsets of the electron Larmor frequencies (detunings) from the microwave carrier frequency, and $D_{kk'}$, $D'_{kk'}$ are coefficients that parameterize the strength of the anisotropic and isotropic parts of the spin-spin dipolar and exchange interactions [60]. Depending on the degree of order and symmetries within the sample structure, $D_{kk'}$ and $D'_{kk'}$ can either be structured (e.g., for crystals) or random (e.g., for glasses). In amorphous materials Δ_k are also distributed due to the anisotropic interaction of the electrons with the static field, leading to inhomogeneous broadening of the EPR line [60, 68].

Dissipative processes are modeled by the jump operators $S_+^{(k)}$, $S_-^{(k)}$ and $S_z^{(k)}$, with rates $\gamma_{1\pm} = \frac{R_1}{2}(1 \mp p)$ and $\gamma_2 = 2R_2$ respectively, where $p = \tanh \frac{\hbar\omega_S}{2k_B T}$. The dissipation rates depend on the longitudinal (R_1) and transversal (R_2) relaxation rates of the electron spins as well as the thermal polarization $p \in [0, 1]$, which depends on the average electron Larmor frequency ω_S and the temperature T. Note, that throughout this section parameters will be expressed through p and thereby acquire their temperature dependence. For typical experimental

conditions (W-band, $\omega_S \sim 100$ GHz, sample temperature between $T \sim 0$ K and $T \sim 100$ K), p is in the region of $1 - 0.01$.

We now summarise the mean field results of Ref. [58]. First, all values of $D_{kk'}$ were fixed to $D/(N-1)$ with the average value of D, and all values $\Delta_k = \Delta$. The factor of $N-1$ accounts for the non-negativity of the coefficient, avoiding a super-extensive growth of state energy. From this, a trace ansatz such as that used in Sec. 4.2.1 results in a mean field phase diagram in the $\Delta - D$ plane with a similarly shaped bistable region as that found in Ref. [3]. The introduction of disorder heavily modifies this structure: a mean field approximation which incorporates disordered values of $D_{kk'}$ and Δ_k leads to a behaviour which is reflected relative to the average value of Δ, see Ref. [58] for details. It is this reflected behaviour with disorder which we seek to confirm numerically next.

4.3.2 Fluctuations in numerical simulations

The mean-field treatment of Ref. [58] is of course not exact. Whether the predicted qualitative phase structure survives away from mean-field depends on the effect of fluctuations [46, 54]. As shown in [3, 4, 69], phase coexistence at the mean-field level can be an indication – away from the thermodynamic limit – of the existence of long-lived metastable (rather than stationary) phases. These competing phases come with an intermittent dynamics of slow switching between them and a significantly longer relaxation time. While the value of the polarization will fluctuate over time within these phases, it will take a distinct average value in each phase.

We now show that this is indeed the case by investigating the numerically exact polarization dynamics for a small system, Eqs. (4.13), by means of quantum jump Monte Carlo simulations, see Sec. 2.2.2. In particular we monitor the time dependence of the polarization $p_z(t) = -(2/N)\sum_k \mathrm{Tr}\,(S_z^{(k)}\rho(t))$ for a variety of values of $a' = \Delta_0/\omega_1\sqrt{\eta}$ and $b' = 3pD_0/2\omega_1\sqrt{\eta}$: here Δ_0 is the mean of Δ_k, D_0 is the standard deviation of $D_{kk'}$, and $\eta = R_2/R_1$. For the set of parameters we consider, multiple disorder realizations of the dipolar coupling $\{D_{kk'}\}$, with $D'_{kk'} = D_{kk'}$ are taken. These are independent and identically distributed, sampled from a Gaussian distribution with variance defined by b'. Different disorder realizations are handled as follows: we begin by taking a set of random numbers from a Gaussian distribution of unit variance, defining the realization. For a given value of b' we then rescale all of these numbers by the

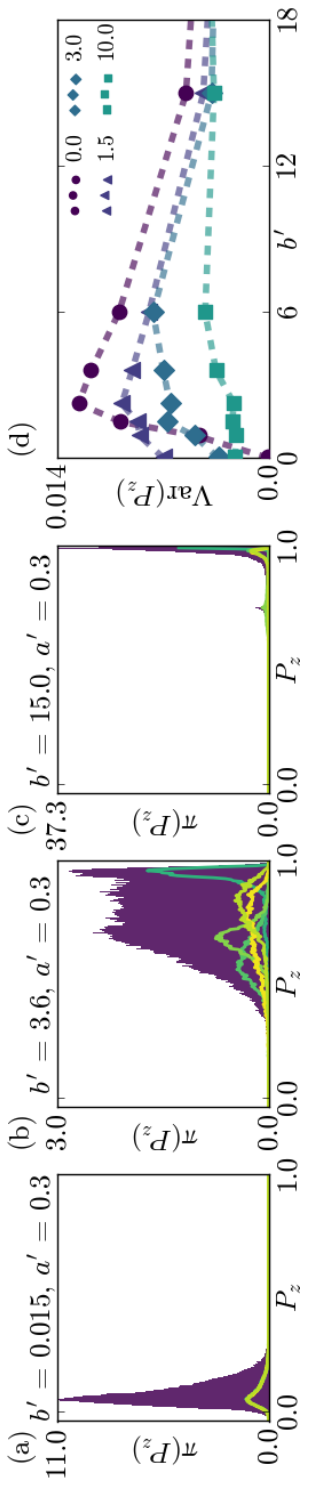


Figure 4.7: Numerical simulations and fluctuations. All results in this figure are produced for parameters $\omega_1 = 10^5$Hz, $R_1 = 1\mathrm{s}^{-1}$, $R_2 = 10^5\mathrm{s}^{-1}$, $p = 0.99$ and $N = 8$, and averaged over 10 disorder realizations. (a-c) Discrete approximations of the probability density (dark shaded area) for the observable P_z for three sets of parameters, such that $\int \pi(P_z)dP_z = 1$ over the range shown. The light colored curves represent the densities for some individual disorders, divided by the number of disorder realizations considered so that their addition (rather than their average) would equal the full probability density. This is done to better represent the contribution each disorder realization makes to the distribution. Panel (b) shows a strongly broadened distribution signalling enhanced fluctuations. This is consistent with the presence of metastable states that are expected from the mean-field analysis. (d) The variance of the time integrated observable P_z for varying b', with the fixed a' value indicated by the legend in the top right.

associated value of the standard deviation D_0. As it can be shown that the probability density satisfies $p_1(x)dx = p_{D_0}(D_0x)d(D_0x)$ where the subscript represents the variance of the Gaussian, this rescaling provides us with an equivalent set of numbers that were effectively drawn from a distribution with standard deviation D_0.

The simulations for Fig. 4.7 are done using the QJMC algorithm (see Sec. 2.2.2) to calculate the trajectory of the pure state of the system over time. To further increase the efficiency of these simulations over the general algorithm previously presented, we take advantage of the algebraic properties of the jump operators to reduce the cost of calculating which jump occurs. We first note that for the parameters chosen, the vast majority of jumps will be dephasing caused by the $S_z^{(k)}$ operators; the probability of dephasing jumps is independent of the state, since $S_z^{(k)\dagger}S_z^{(k)} = I$. The total unnormalized probability of dephasing is thus simply N times the norm of the state when a jump occurs. Meanwhile, for spin flip jumps caused by $S_+^{(k)}$ and $S_-^{(k)}$ we have $S_\pm^{(k)}S_\mp^{(k)} = I \mp S_z^{(k)}$: the total unnormalized probability of either flips up or down can therefore be calculated from the norm of the state and its total magnetisation.

In practice, this allows us to adopt the following procedure. We partition the interval $[0, 1]$ in three according to the relative probabilities of the three species of jumps, and identify which type of jump occurs using a random number. Once the sector in this which number resides is found, this sub-interval is partitioned over the sites, calculating the necessary additional expectations: the random number is shifted and rescaled to find which site the jump occurs on. For the most common case of dephasing, this requires no further calculations, reducing the potential calculation of $3N$ expectation values in the generic algorithm in Sec. 2.2.2 to a single expectation value: the magnetisation, calculated for the initial partition. In a system of $N = 8$ spins, this modification reduces the average CPU time for a trajectory by a factor of 10.

All trajectories are initialized in the same state, the all up configuration, data from a trajectory is only considered after sufficient time has elapsed that there is no memory of the initial state (we can be certain such a time scale exists for this finite system due to the results of [54]), i.e. after the relaxation time. The remainder of the trajectory is then cut up into time periods T of $\mathcal{O}(10^{-2}\text{s})$, chosen such that short time fluctations are averaged out so that only long time fluctuations influence the variance of the time integrated observable (similar to the approach used in Sec. 4.2.5).

Fluctuations due to metastability can be quantified by the probability distribution of the time integrated polarization, $P_z = (1/t)\int_0^t p_z(t')dt'$. As t is increased in systems without metastability we expect a contracting distribution with a single, approximately Gaussian peak around the stationary state value. In the presence of metastability we instead expect a broadened, non-Gaussian distribution. In particular for t on the order of metastable phase lifetimes one expects multiple peaks located near the average values of the different metastable phases. While we lack the distinct metastable phases due to small sizes and disorder, for t on the order of relaxation time, Fig. 4.7(a-c) shows an intermediate regime in which the disorder averaged distribution is strongly broadened and non-Gaussian. In Fig. 4.7(d) we plot the variance as a function of b' for several values of a'. We see a peak at intermediate values of b' for all curves, which is consistent with the expectation of a phase transition in the thermodynamic limit.

4.4 Summary

We have applied the general theory of metastability developed recently in Ref. [2] to the dynamics of an open many-body quantum system, namely the open quantum Ising model with transverse field in the presence of site decay, a model which could potentially be realised using Rydberg atoms. For this system the origin and properties of the metastable dynamics is particularly transparent: in a region of parameter space where interactions and transverse field compete there is time separation in the dynamics, such that the two leading eigenmodes of the master operator split from the rest. This means that the metastable manifold to which an initial state decays at short times is a one-dimensional simplex given by the convex combinations of two extreme metastable states. These two states represent the two metastable phases of the problem: an almost pure state of negative magnetisation in the z-direction, and one mixed state of almost vanishing magnetisation. We have also shown that the dynamics of this model at long times can be understood in terms of an effective classical dynamics between two phases inside the metastable manifold, which converges to the unique stationary state asymptotically.

We have further seen that the short time behaviour and the existence of the long-lived metastable states are qualitatively captured by a straightforward mean-field approximation to the dynamics, very much in the spirit of what

one does in slowly relaxing classical systems. Additionally, we discussed how metastability is directly related to fluctuating dynamics in individual realizations of the system evolution, specifically in the form of intermittency of quantum jump trajectories. The physical ingredients that give rise to metastability in the model studied here are those that could also be responsible for the system having a true stationary state phase transition in the thermodynamic limit. But just like in the case of analogous classical problems, the dynamics we uncovered (separation of timescales, transient relaxation to long-lived states, intermittency due to switching between metastable phases) is not dependent on that transition being present: metastability would occur in systems where the transition is avoided either through finite size or due to other kind of fluctuations.

The concrete application of the ideas of Ref. [2] to a many-body system should pave the way for further studies of metastability in other systems with even richer emergent collective dynamics, in particular systems where the manifold of long lived states is higher dimensional, potentially allowing for quantum mechanical evolution between these states.

Chapter 5

Classical metastable manifolds in open quantum systems

While the previous chapter focused on a simple case in which the metastable manifold was described by a line, we now describe techniques for constructing and analysing the metastable manifold when it is described by a higher dimensional simplex. Often the focus of studies on nonequilibrium open many-body quantum systems is a phase structure of the system stationary state, which can be characterised for example by static order parameters such as magnetisation. A question recently explored is whether such many-body systems can exhibit in the thermodynamic limit bistability (or multistability) of the stationary state, a topic covered both theoretically [69, 75–77] and experimentally [78, 79]. While the properties of system dynamics frequently preclude such an occurrence at a finite size [54], mean-field results often suggest multiple stationary states at infinite size [3, 37]. More sophisticated (albeit still approximate) techniques such as variational approaches [46–48], infinite tensor network simulations [38], or a field-theoretical analysis [37], however, usually indicate existence of a unique stationary state in the thermodynamic limit.

Regardless of the fate of the stationary state in the thermodynamic limit, multiple stationary states in the mean-field approximation often indicate the occurrence of metastability for finite-size systems, as seen in Chap. 4, i.e. distinct timescales in the evolution of the probability over configurations space of a classical model [1, 14–16, 50], or, for a quantum system, in the dynamics of a density matrix [2]. These timescales correspond to a fast evolution towards a set of long-lived metastable states, which is followed by a slow relaxation to the final stationary state. In some cases there is a further hierarchy of timescales

before the eventual final evolution to the stationary state [80].

As we have seen, metastability in classical systems with Markovian dynamics [1, 14–16, 50] and open quantum systems [2, 51] described by the Lindblad formalism [20, 21] requires a large separation in the eigenvalues of the master operator governing the system evolution, defining a manifold of long time states and the dynamics within it. The approach described in Sec. 2.1.3 and the previous chapter is restricted to 1D MMs; in this chapter we develop numerical techniques to unfold higher dimensional sets of relevant states supporting metastable dynamics in a general open quantum system, when the metastability is classical: in this case, the metastable states can be understood as probability distributions over the set distinct metastable phases.

Our spectral approach relies on the ability to diagonalise the system master operator, which is usually possible only for moderate system sizes. However, larger sizes may be required for metastability to become prominent in the statistical description of a model. Fortunately, the probabilistic presence of metastability is accompanied by a signature in the individual trajectories of a systems evolution: as seen previously, and as we will see here, the classical dynamics between the metastable phases can be observed as intermittence [3, 4, 40] or dynamical heterogeneity [5, 81] of system observables within a trajectory. These trajectories correspond to individual runs of an experimental system, or QJMC simulations [19, 24] (see Sec. 2.2.2) which may be done at larger system sizes than exact diagonalization, and average to return the dynamics described by the master operator. We further show that metastable phases of these dynamics may be extracted from trajectories through the use of large-deviation methods such as the "thermodynamics of trajectories" [3, 39, 40, 82, 83], thus allowing the study of metastability at much larger system sizes using QJMC simulations.

We have seen that for classical and quantum systems, metastability is often a consequence of proximity to a static first-order phase transition of the stationary state in the thermodynamic limit [13], but this is not necessary. In classical kinetically constrained models [42, 43, 84–87] the evolution of any system component is conditioned on the state of other components, resulting in glassy dynamics. This manifests both in dynamical heterogeneity and a hierarchy of timescales, despite the absence of transitions in the static properties of the constrained models. Quantum adaptations of these models have been produced through the concept of Rokhsar-Kivelson points [88, 89], leading to

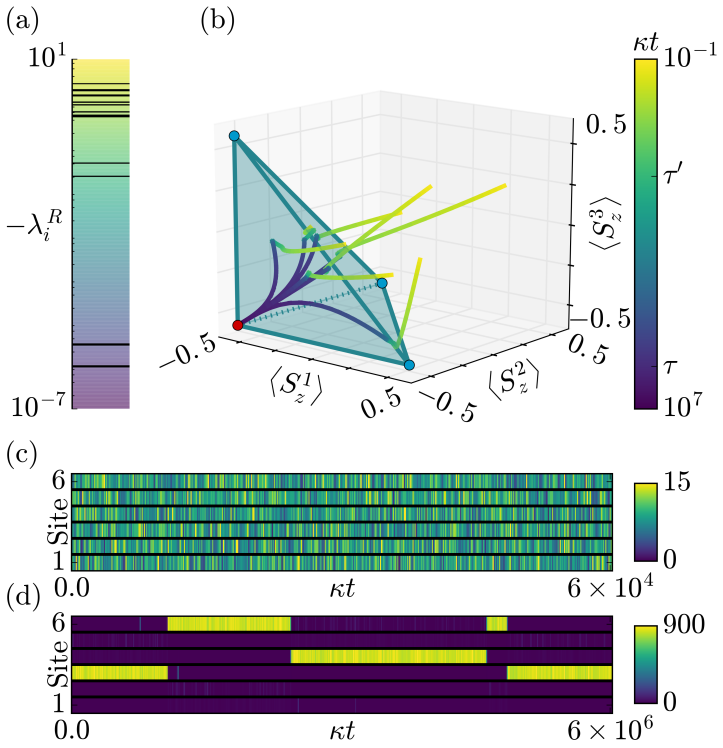


Figure 5.1: Metastable dynamics in the dissipative quantum East model: (a) Spectrum of the dissipative quantum East model with $N = 3$ spins shows a large separation $-\lambda_4^R \ll -\lambda_5^R$ for $p = 0.999$, $\Omega/\kappa = 0.1$, $\gamma/\kappa = 0.0001$. (b) The corresponding dynamics of average site magnetisation is shown for random initial states, with lines coloured according to the time along the curve in a log scale. After the initial relaxation (yellow-green) the site magnetisation approaches a limited region of values, which is well captured by the blue simplex of the magnetisation of metastable phases (green and blue dots), before final relaxation (blue-purple) to the unique stationary state (red circle), cf. Fig. 5.2. (c-d) QJMC trajectories of the dissipative quantum East model with $N = 6$ spins, for the non-interacting unconstrained case with $p = 0$ in (c), and for fully constrained case with $p = 1$ in (d), where dynamical heterogeneity is pronounced. Color indicates the number of jumps J_j^-, (5.24), of each spin (associated photon emissions), grouped for visibility in 500 time bins. The other parameters in (c), (d) are given by $\Omega/\kappa = 0.12$ and $\gamma/\kappa = 0.0096$.

quasi-many body localization behaviour in closed quantum systems [90–92]. Recent open quantum generalisations of these models [5, 40, 81] are also known to display dynamical heterogeneity; a model introduced in Ref. [5] acts as an extensive case study of complex metastability in open quantum systems, which we use to demonstrate the effectiveness of our techniques.

This chapter is organized as follows. In Sec. 5.1, we introduce the approach to classical metastability in open quantum systems. We begin in Sec. 5.1.1 by describing how to numerically construct a classical MM, along with a test to verify the classicality of metastable states in general open quantum dynamics. In Sec. 5.1.3 we relate the classical system dynamics at large times to intermittence in trajectories. Our approach is then applied to the dissipative quantum East model in Sec. 5.2, with discussion of the approach accuracy in Sec. 5.2.1, the properties of the classical MM in Sec. 5.2.2, and the features of the classical long-time dynamics in Sec. 5.2.3. Finally, we describe a construction of the classical MM using QJMC and large deviation methods in Sec. 5.3. We note here that this chapter is based largely on a paper, Ref. [93], containing rigorous mathematical backing for the algorithms presented here, and extensive perturbation theory results for our dissipative quantum East model case study. We will regularly reference the paper for results we do not present here.

5.1 Classical metastable manifolds

Recall that metastability results from a large separation in the real part (indicated by the superscript) of the spectrum [2], $\lambda_m^R \gg \lambda_{m+1}^R$, of the Lindblad operator Eq. (2.25), see Fig. 5.1(a,b). As discussed in Chap. 4, for times $t \gg \tau' = -1/\lambda_{m+1}^R$, the terms beyond the m-th in the sum in (2.33) can usually be neglected. Time dependence of the remaining terms can further be neglected, $e^{t\lambda_k^R} \approx 1$ for $k \leq m$, when the separation is big enough to have $-1/\lambda_m^R \ll t \ll -1/\lambda_m^R$. In this case the system state is metastable and can be approximated by the reduced expansion,

$$\rho(t) \approx \rho_{\text{ss}} + \sum_{k=2}^{m} c_k e^{it\lambda_k^I} R_k = \mathcal{P}\rho(0), \tag{5.1}$$

where $\mathcal{P}$ is the projection onto the low-lying eigenmodes of the master operator, i.e. the MM, and λ_k^I is the imaginary part of eigenvalue λ_k. Unlike Chap. 4, we now consider the general case of $m > 2$.

The MM is convex as a linearly transformed convex set of initial states,

and $(m-1)$-dimensional as parametrised by the coefficients $(c_2, ..., c_m)$, see Fig. 5.2(a), and cf. Fig. 5.1(b). At later times, $t \gg \tau'$, only the first m modes contribute to the evolution, cf. Eq. (5.1), which thus takes place essentially inside the MM and is generated by $\mathcal{L}_{\text{MM}} = \mathcal{P}\mathcal{L}\mathcal{P}$, see Fig. 5.2(b).

5.1.1 Constructing classical manifolds

In this chapter, we aim to study generic classical MMs, rather than just those with two metastable phases as in Chap. 4. Therefore, let us first consider a common classical regime for metastability: Markovian dynamics near a first order phase transition. At the transition, a system will possess a structure of multiple stationary states, corresponding to the dominant phases around the transition point: mathematically, these phases are provided by a physical basis of disjoint probability distributions over the right 0-eigenmodes. In turn, the dual of this basis over the left 0-eigenmodes describes the basins of attraction for these phases. The system has a probability of being in each of these phases at infinite time, for a given initial condition, depending on its initial probability of being located in the basin of attraction associated to each phase: the set of long time states thus forms a simplex with vertices corresponding to each distinct phase.

These phases and the corresponding basins remain when small changes to the system cause stationary states to become weakly unstable: for example, when the system parameters are moved a short distance from a transition, or when we instead consider finite size systems. Under such conditions these phases become metastable, with the basins describing the probability of being in a given phase on metastable timescales; the MM of long time states inherits the simplex structure of the stationary states, defined by the low-lying spectral structure. Remarkably, any MM in classical Markovian dynamics can be approximated by a simplex of approximately disjoint metastable phases [1, 14, 16], whether it results from proximity to a phase transition, or due to another origin such as the constrained dynamics of glassy systems.

For open quantum dynamics, in the case of $m = 2$ it is known that there any metastable state is a probabilistic mixture of two almost disjoint metastable phases [2, 4]. In general, however, the structure of an MM is no longer necessarily a simplex: in contrast to the classical case, where stationary manifolds at transitions feature only disjoint phases [94], open quantum systems may possess decoherence free subspaces (DFS) [95–97] and noiseless subsystems

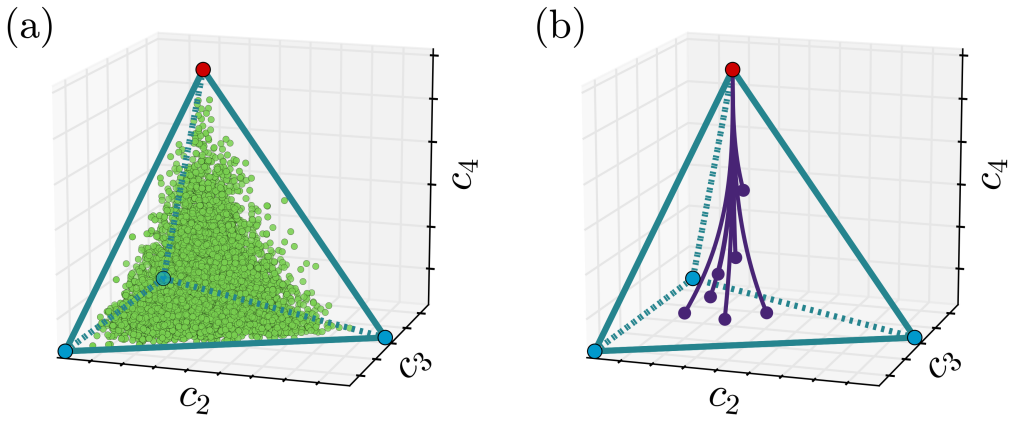


Figure 5.2: Example of metastable manifold: (a) The metastable manifold in the open quantum East model of $N = 3$ spins with periodic boundary conditions, illustrated by the coefficients (c_2, c_3, c_4) in Eq. (5.1). The blue lines show the simplex of $m = N + 1 = 4$ metastable phases (found at the vertices), while the small green dots indicate the projections of randomly generated pure states onto the MM. (b) The long-time evolution inside the MM towards the stationary state (red circle) for randomly selected initial states (also shown in Fig. 5.1b). In (a,b) the three metastable phases degenerate in c_4 (green dots) correspond to a 3-cycle of the translation symmetry (as L_2, L_3 gain a phase), while the top metastable phase (blue dot) is invariant to the symmetry (and so is L_4), cf. Fig 5.1(b). Softness $p = 0.999$ and other parameters as in Fig. 5.1(a,b).

(NSS) [98,99]. Thus, this more general structure will be inherited by the MM in proximity to such a transition [2]. For a given highly dimensional MM it is not easy however, to determine its structure from a general basis of 0-eigenmodes, even directly at a phase transition (see e.g. [100], while the algebraic approach in [101] cannot be generalised straightforwardly beyond the transition point).

In this chapter, we introduce a systematic approach for constructing the set of phases which provide the best simplex approximation to the MM for an open quantum system, and describe how to verify its accuracy, i.e. how classical the systems MM is. If accurate, this provides us with a set of operators defining metastable phases and the corresponding basins of attraction, which allow a complete understanding of the long time dynamics. To achieve this, we note that since the MM is convex, it necessarily contains all probabilistic mixtures constructed from any set of m metastable states, defining a simplex in the space of coefficients $(c_2, ..., c_m)$. The main idea behind our approach, sketched in Fig. 5.3, is to choose the set of m metastable states leading to the simplex of the maximal volume, see Fig. 5.2, thus covering as much of the true MM as possible. We then verify the classicality of this manifold by considering errors in the operators defining basins of attractions for the metastable phases, calculating a simple bound on the maximum distance of any metastable state from a given simplex, see Eq. (5.8) below.

Maximal volume simplex. Recall that a standard choice of right and left basis for the MM is given by the low-lying eigenmodes of $\mathcal{L}$, $R_1 = \rho_{\rm ss}$, $L_1 = \mathbb{1}$ for $k = 1$, and R_k, L_k, for $k = 2, ..., m$. However, the eigenmodes R_k, $k = 2, .., m$, do not represent physical states of the system as $\mathrm{Tr}(R_k) = 0$ from the trace-preservation ($L_1 = \mathbb{1}$) and orthogonality of the modes [$\mathrm{Tr}(L_j R_k) = \delta_{jk}$]. In contrast, any set of m metastable states $\rho_1(t)$,..., $\rho_l(t)$, by the truncation in Eq. (5.1), provides an approximately positive basis in the space of metastable states defined as

$$\tilde{\rho}_l \equiv \rho_{ss} + \sum_{k=2}^{m} c_k^{(l)} R_k, \quad l = 1, ..., m, \tag{5.2}$$

as long as $\tilde{\rho}_l$ are linearly independent. Furthermore, this set defines vertices of a simplex in the space of coefficients, with the volume equal the determinant of the corresponding basis transformation between R_1, ..., R_m, and $\tilde{\rho}_1$,..., $\tilde{\rho}_m$ [1],

$$(C)_{lk} \equiv c_k^{(l)}, \quad k, l = 1, ..., m, \tag{5.3}$$

[1] $\det C = \det D$, where $D_{l-1,k-1} = c_k^{(l)} - c_k^{(1)}$, $k, l = 2, .., m$, encodes the coefficients for the simplex with the 1st vertex shifted to the origin

so that $\tilde{\rho}_l = \sum_{k=1}^{m} (C)_{lk} R_k$, cf. Eq. (5.2). Indeed, the volume $\det C \neq 0$ for linearly independent states.

In order to find a basis of metastable states corresponding to the maximal simplex, we first note that the values of the coefficients c_k in Eq. 5.1 are bounded by the extreme eigenvalues of the left eigenmatrices, L_k, values which must therefore be achieved by the m vertices of the maximal simplex. It is thus reasonable to expect a good set of candidates for this simplex to consist of the $2(m-1)$ eigenvectors of the L_k associated to their extreme eigenvalues, for $k = 2, ..., m$: indeed, for extreme coefficient values achieved by a single vertex, we show that the corresponding extreme eigenvector resides close to the vertex in Ref. [93]. Some vertices must achieve multiple extreme values, since there are only m metastable phases to achieve $2(m-1)$ extreme values: the result of Ref. [93] thus implies some extreme eigenvectors must be almost identical, allowing us to reduce this set by clustering.

Despite the above result, the set of extreme eigenvectors may not be sufficient to identify the vertices of the simplex. When extremes of the coefficients are achieved by more than one vertex, the extreme eigenvectors may consist of mixtures of the vertices achieving this extreme. This may occur as an accidental degeneracy, or as we will see later, neccessarily occurs as a result of a systems symmetries. Further, it is possible that some vertices of the simplex may achieve no extreme values. Both of these issues may be addressed by considering extreme eigenstates of multiple random rotations of the left eigenmatrices: vertices missing the unrotated set of extreme eigenstates may achieve an extreme coefficient value of a rotated basis uniquely, thus being covered by an extreme eigenstate of the rotated basis. The resulting enlarged set of candidate states may then be clustered in coefficients of the original basis, providing a reduced set which is likely to contain all vertices, plus some of their mixtures. The combination of candidates corresponding to the vertices can then be identified as the combination providing the largest volume simplex.

To clarify the above, a generic approach to finding the vertices of the best simplex approximation to the MM is as follows:

1. Diagonalize $\mathcal{L}$ and construct a hermitian basis of the left and right eigenmatrices for the m eigenmodes below the gap in the spectrum.

2. Construct a set of candidate states:

    i. Apply a random rotation to the basis of left eigenmatrices L_k.

ii. Diagonalize the resulting basis of matrices and store the eigenstates associated to their extreme eigenvalues as candidates.

iii. Repeat for the desired number of random rotations.

3. Cluster the eigenvectors into a reduced set according to their relative distance in the truncated space of coefficients for the unrotated left eigenbasis, c_k for $k = 2, ..., m$.

4. Find vertices for the best simplex approximation as the combination of the remaining candidates providing the simplex with the largest volume.

Our approach, sketched in Fig. 5.3, finishes by checking the consistency of our assumption that the MM is classical.

Test of classicality. For low dimensional MMs, the classicality can be visibly observed by projecting a randomly generated set of initial conditions on to their metastable states, as done in Fig. 5.2(a) for an open quantum East model of $N = 3$ spins, where the MM is 3-dimensional. The metastable states are found well within the chosen simplex, confirming the classicality of the MM.

Were states found outside the simplex, it would be an indication that it provides a bad approximation to the MM, indicating the existence of states outside the basins of attraction for metastable phases. These basins are understood through the new left basis dual to Eq. (5.2), given by the inverse transformation to (5.3),

$$\tilde{P}_l = \sum_{k=1}^{m} (C^{-1})_{kl} \, L_k, \tag{5.4}$$

which are orthogonal by construction

$$\mathrm{Tr}(\tilde{P}_k \tilde{\rho}_l) = \sum_{n=1}^{m} (C^{-1})_{nk} (C)_{ln} = (CC^{-1})_{lk} = \delta_{kl}. \tag{5.5}$$

We note that the normalization of these matrices is fixed: in the eigenbasis, we have the freedom of choice to normalize either the left or right eigenmatrices, as only $\mathrm{Tr}(L_j R_k) = \delta_{jk}$ is required; in contrast, there is no freedom left in the normalization of the dual basis given by Eq. (5.4), as the trace of the metastable states of Eq. (5.2) is fixed to 1. A given simplex thus defines a unique dual basis, which we now use to understand the accuracy of the simplex.

The overlaps with these operators describe the probability of the system being measured in the corresponding metastable phase,

$$\tilde{p}_k = \mathrm{Tr}[\tilde{P}_k \rho(0)], \tag{5.6}$$

and are, by definition, the barycentric coordinates within the chosen simplex: the positions between each vertex and the opposing side of the simplex. A state within the metastable regime can thus be approximated as, cf. Eq. (5.1),

$$\rho(t) \approx \sum_{k=1}^{m} p_k \tilde{\rho}_k. \tag{5.7}$$

While $\sum_{k=1}^{m} \tilde{p}_k = 1$ is guaranteed for all states by trace preservation of the dynamics, for states outside the simplex, $\tilde{p}_k$ may be below 0 or above 1. The distance a probability $\tilde{p}_k$ can be outside this range is bounded by the eigenvalues of the $\tilde{P}_k$ operators, as with the coefficients c_k and eigenmatrices L_k before. Therefore, by checking the spectrum of the dual basis Eq. (5.4), we can investigate how well the simplex approximates the MM.

In particular, consider the number of $\tilde{P}_k$ eigenvalues below 0, normalised by the dimension D of the system Hilbert space (e.g. $D = 2^N$ for a chain of N spins-1/2),

$$\bar{\mathcal{C}} \equiv D^{-1} \sum_{k=1}^{m} \sum_{l=1}^{D} \max\left(-\lambda_k^{(l)}, 0\right), \tag{5.8}$$

where $\lambda_k^{(l)}$ is the l-th eigenvalue of $\tilde{P}_k$. Geometrically, the eigenvalues below zero determine how far a state could be away from the face of the simplex opposite the associated phase: averaged over initial states, we would expect this to dominate the eigenvalues above 1 in the average distance of states outside the simplex, since to the surface area of the simplex they are relevant for is much larger. Indeed, in Ref. [93], we show that $2\bar{\mathcal{C}}$ bounds from above the average L_1-distance of metastable states from the chosen simplex in the coefficient space. Meanwhile, the maximal distance of any metastable state from the simplex is bounded by twice

$$\mathcal{C}_{\max} \equiv \sum_{k=1}^{m} \max\left(|\lambda_k^{\min}|, 0\right) \geq D\,\bar{\mathcal{C}}, \tag{5.9}$$

where $\lambda_k^{\min}$ is the minimal eigenvalue of $\tilde{P}_k$. Furthermore, the average and maximal distance in the space of density matrices, are respectively bounded by $2\,\bar{\mathcal{C}}(1 + \mathcal{C}_{\mathrm{MM}})$ and $2\,\mathcal{C}_{\max}(1 + \mathcal{C}_{\mathrm{MM}})$, where

$$\mathcal{C}_{\mathrm{MM}} = \max_{1\leq k\leq m} \min_{0\leq t<\infty} \|\rho_k(t) - \tilde{\rho}_k\|_1 \tag{5.10}$$

with $\rho_l(t)$ projecting onto $\tilde{\rho}_k$ in the expansion (5.1), denotes the corrections to the positivity (and stationarity) of the metastable phases in the trace-norm. Note that for systems with metastability, not necessarily classical, by definition,

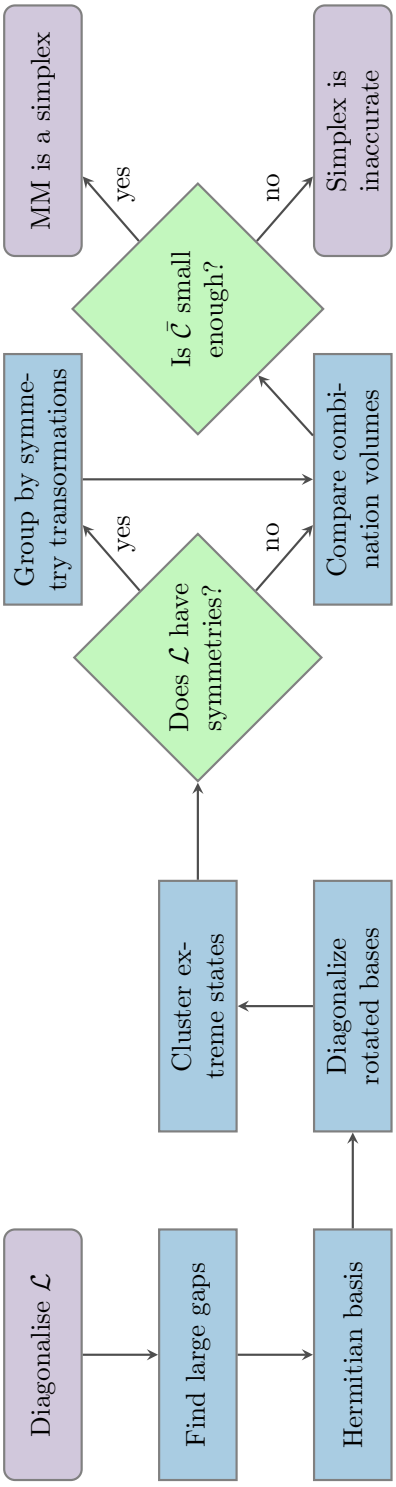


Figure 5.3: Metastable manifold construction: We sketch the main steps in the approach to constructing the maximal simplex within a given metastable manifold, providing the best classical approximation. This is based on the combination of the clustering result of Ref. [93] with random rotations of the basis of left eigenmatrices, as described in the text. The algorithms speed can be further enhanced by making use of symmetries to group the candidate metastable states. Finally, we supplement the construction with a consistency check based on the accuracy measure $\bar{\mathcal{C}}$.

we require $C_{MM} \ll 1$, and thus it will contribute in the higher order to the bounds on the distance.

Therefore, when $\bar{\mathcal{C}}$ of (5.8) and $\mathcal{C}_{\max}$ of (5.9) are small in comparison to distances inside the simplex (rescaled by 2), which in L_1-norm are bounded exactly by 1, the MM is well approximated with the given simplex, and thus is classical. This is demonstrated in our case study, the quantum East model investigated in Secs. 5.2-5.3, where we find that long-lasting metastable phases form a simplex of $N+1$ metastable phases for N spins, with a strong bound on the distance of states from the simplex, see Fig. 5.4.

Combined with the procedure for constructing the metastable phases, this measure of accuracy completes the generic clustering based algorithm outlined in Fig. 5.3. In general, we expect this to fail whenever the MM is not classical, as is the case for quantum MM [2] featuring decoherence free subspaces [95–97] or noiseless subsystems [98, 99]: for example, qubit DFSs or NSSs amount to Bloch-sphere structures in the coefficient space, rather than a simplex, see also [102]. The approach we describe will also fail when the low-lying part of the master operator spectrum is not sufficiently separated from the rest of the spectrum, e.g. when the system size is insufficient for the effects of a phase transition to induce a gap.

Utilising discrete symmetries. Constructing metastable manifolds via the approach previously discussed is impeded by the presence of symmetries; however, the construction can also be augmented by utilising these symmetries. To this end, we will now discuss how the discrete symmetries relate to the eigenmatrices of the Lindblad operator. Consider the system dynamics $\mathcal{L}$ obeying a discrete symmetry on the super-operator level, a so called *weak symmetry*, $[\mathcal{L},\mathcal{U}] = 0$, where $\mathcal{U}\rho \equiv U\rho U^\dagger$ and $U^d = \mathbb{1}$ for some $d \in \mathbb{N}$, see Refs. [25, 26, 94]. As we consider a unique stationary state, we are interested in the case when the symmetry U is not itself conserved by the dynamics, $\mathcal{L}^\dagger(U) \neq 0$, otherwise there would be at least as many stationary states as the number $n \leq d$ of eigenspaces of U [26]. For example, in the open quantum East model with periodic boundary conditions discussed in Sec. 5.2, $\mathcal{U}$ can be chosen as the translation symmetry, in which case $n = d = N$ equals the number of spins.

From $[\mathcal{L},\mathcal{U}] = 0$ it follows that the master operator $\mathcal{L}$ is block-diagonal in the operator basis of eigenmatrices of $\mathcal{U}$. Therefore, the eigenmatrices of $\mathcal{L}$, R_k and L_k, can be chosen as eigenmatrices of $\mathcal{U}$, whose structure we now briefly characterise. The superoperator $\mathcal{U}$ features at most d different

eigenvalues, inherited from U: as $U^d = \mathbb{1}$, we have eigenvalues $e^{i\phi_k}$ with $\phi_k = 2\pi k/d$. Let V_k be the corresponding eigenspace of U spanned by $|\psi_{j_k}^{(k)}\rangle$, $j_k = 1, ..., \dim(V_k)$. The eigenmatrices of $\mathcal{U}$ with an eigenvalue $e^{i\delta\phi} \neq 1$ correspond to coherences between U-eigenspaces, e.g. $|\psi_{j_k}^{(k)}\rangle\langle\psi_{j_l}^{(l)}|$ between V_k and V_l when $\delta\phi = \phi_k - \phi_l = 2\pi(k-l)/d$. In particular, the eigenvalue 1 corresponds to symmetric operators, i.e. linear combinations of operators supported on V_k, $|\psi_{j_k}^{(k)}\rangle\langle\psi_{j'_k}^{(k)}|$, $k = 1, ..., n$. Due to the symmetry, the eigenmatrices of $\mathcal{L}$ can also be chosen as eigenmatrices of $\mathcal{U}$, i.e., $\mathcal{U}^\dagger(L_k) = e^{-i\delta\phi_k} L_k$ and $\mathcal{U}(R_k) = e^{i\delta\phi_k} R_k$, in which case under the symmetry transformation $\rho \mapsto \mathcal{U}(\rho)$ the coefficients simply gain a phase $c_k = \mathrm{Tr}[L_k\rho] \mapsto e^{-i\delta\phi_k} c_k$.

Coefficient degeneracy due to symmetry. One of the reasons our generic algorithm considers random rotations is to compensate for cases in which extreme values of the coefficients are achieved by multiple vertices: when these extremes are degenerate in coefficients of the reduced eigenbasis. While unlikely to occur in a generic model, it is not uncommon to end up with a basis of L_k in which these eigenvalues are degenerate: a typical example would be models with symmetries, such as the translation invariance present in the dissipative quantum East model we consider in Sec. 5.2.

To see how symmetries result in degeneracies, first, let us note that if there exists a low-lying invariant eigenmmatrix L_k, $\mathcal{U}^\dagger(L_k) = L_k$, its eigenvectors, in particular the extreme eigenvectors, can be chosen as invariant states. The metastable states originating from those invariant eigenvectors will also be symmetric, and thus have 0-coefficients for any asymmetric eigenmatrix L_l, $\mathcal{U}^\dagger(L_l) \neq L_l$. As a result, the extreme states may correspond to mixtures of asymmetric metastable phases, rather than a single symmetric phase: this is demonstrated in the vertical coefficient c_4 in Fig. 5.2, where the lower extreme eigenvector may lie anywhere in the lower triangle.

Second, note that the asymmetric eigenmatrices $\mathcal{U}^\dagger(L_l) = e^{i\delta\phi_l} L_l$, where $e^{i\delta\phi_l} \neq 1$, are necessarily not hermitian, since $\mathcal{U}^\dagger(L_l^\dagger) = [\mathcal{U}^\dagger(L_l)]^\dagger = e^{-i\delta\phi_l} L_l$, and thus $L_l^\dagger$ (which is also an eigenmatrix of $\mathcal{L}$ due to the hermiticity preservation in the dynamics) belongs to a different eigenspace of $\mathcal{U}^\dagger$. In order to consider hermitian operators we can replace L_l and $L_l^\dagger$ by $L_l^{\mathrm{Re}} \equiv (e^{i\varphi} L_l + e^{-i\varphi} L_l^\dagger)/2$ and $L_l^{\mathrm{Im}} \equiv (e^{i\varphi} L_l - e^{-i\varphi} L_l^\dagger)/2i$, where $e^{i\varphi}$ is an arbitrary phase [with the corresponding transformation of R_l and $R_l^\dagger$ into $e^{-i\varphi} R_l + e^{i\varphi} R_l^\dagger$ and $i(e^{-i\varphi} R_l - e^{+i\varphi} R_l^\dagger)$]. Due to the free phase $e^{i\varphi}$, corresponding to rotation by the angle φ of the new coefficients, the projection of the maximal simplex on the new

coordinates can again lead to more than a single phase corresponding to the extreme values of new coefficients: this is visible in the coefficient c_3 in Fig. 5.2, where the left extreme eigenvector may lie anywhere on the lower left edge of the simplex.

Symmetry transformations of metastable manifold. While the degeneracies discussed above are addressed by our generic algorithm, when symmetries are present the number of combinations for which the simplex volume must be checked can become substantial. However, the number of combinations can be reduced substantially by making use of the symmetry: intuitively we would expect a symmetry transformation of a metastable state to also be a metastable state, allowing us to instead consider combinations of candidate state sets which are invariant under transformations. To this end, we show in Ref. [93] that for discrete symmetries, the vertices of a classical MM must be approximately permuted under an action of the symmetry, with corrections on the order of the simplex approximation's accuracy, Eq. (5.9).

This allows us to enhance the generic algorithm, as sketched in Fig. 5.3. After clustering near-identical candidate states, we can further group candidates according to their transformations under symmetries, removing any duplicated sets. These groups may further include vertices not covered by extreme eigenvectors of the current matrix basis: for example, in the case study of Sec. 5.2, using symmetries as described here removes the need to consider randomly rotated bases.

5.1.2 Disjointness of metastable phases in classical MM

In Sec. 5.1.1 we discussed when the metastable manifolds of open quantum systems, in the coefficient space of low-lying eigenmodes, can be well approximated by a simplex, and how to construct the vertices of that simplex. When this is the case any system state during the metastable regime, i.e., any metastable state given by Eq. (5.1), can be approximated as a classical probabilistic mixture of metastable phases corresponding to the vertices of the chosen simplex, cf. Eqs. (5.8) and (5.9).

As we now explain, the classical features of the metastable manifold go even further. Namely, the metastable phases $\tilde{\rho}_1$, ..., $\tilde{\rho}_m$, are not only *approximately positive* with their trace equal 1 [which directly follows from the expansion in Eq. (5.1)], but can be shown to be *approximately disjoint* in analogy to the classical metastability and classical phase transitions [16]: that is, distinct

metastable phases describe states restricted to distinct regions of the state space.

In Ref. [93] we prove (in the leading order of corrections) that

$$\mathrm{Tr}[\rho_k(t)^{1/2}\rho_l(t)^{1/2}] \lesssim 2\,(\mathcal{C}_{\max}+\mathcal{C}_{\mathrm{MM}})^{1/2}, \tag{5.11}$$

where $k,l=1,...,m$, $k\neq l$, $\rho_k(t)$ is a metastable state that projects onto $\tilde{\rho}_k$ in the expansion in Eq. (5.1). We have two types of corrections: $\mathcal{C}_{\mathrm{MM}}$, Eq. (5.10), denotes the corrections to stationarity in the metastability regime (which are also corrections to the positivity of the metastable phases), and $\mathcal{C}_{\max}$ bounds the distance from the simplex of any state in the metastable manifold, cf. Eq. (5.9). Since $\rho_k(t)$ is positive, the bound in Eq. (5.11) implies that the metastable phases must be *approximately disjoint*.

Indeed, for the subspace $\mathcal{H}_k$ defined as the space spanned by eigenstates of the projections $\tilde{P}_k$ with eigenvalues equal or above $1/2$ we have

$$\mathrm{Tr}[\mathbb{1}_{\mathcal{H}_k}\,\rho_l(t)] \lesssim 2(\mathcal{C}_{\max}+\mathcal{C}_{\mathrm{MM}}), \tag{5.12}$$

$$\mathrm{Tr}[\mathbb{1}_{\mathcal{H}_k}\,\rho_k(t)] \gtrsim 1-2(\mathcal{C}_{\max}+\mathcal{C}_{\mathrm{MM}}), \tag{5.13}$$

while $|\mathrm{Tr}[\mathbb{1}_{\mathcal{H}_k}\,\rho_l(t)]-\mathrm{Tr}(\mathbb{1}_{\mathcal{H}_k}\,\tilde{\rho}_l)|\leq\mathcal{C}_{\mathrm{MM}}$. Here $\mathcal{H}_k$ captures not only majority of $\rho_k(t)$ [or $\tilde{\rho}_k$] support, but also its *basin of attraction*, i.e. the initial system states which in the metastable regime are approximated by $\tilde{\rho}_k$. For derivation see Ref. [93].

Finally, we note that a similar bound to Eq. (5.11) can be proven implying the approximate orthogonality of metastable phases, but in that case the scalar product, $\mathrm{Tr}[\rho_k(t)\rho_l(t)]\leq\mathrm{Tr}[\rho_k(t)^2]^{1/2}\mathrm{Tr}[\rho_l(t)^2]^{1/2}$, will be not only small as a consequence of classical metastability, but will also be reduced by the mixedness of metastable phases (see Ref. [93]).

5.1.3 Effective classical dynamics and intermittence

The disjointness of these metastable phases relevant on large time scales, and the eventual relaxation to a stationary state over these phases, is suggestive of an effective classical dynamics of jumps between these phases. We now describe this dynamics, and the corresponding signature in individual trajectories of a systems evolution, in detail.

Effective long-time dynamics. The evolution for times $t\gg\tau'\equiv(-\mathrm{Re}\lambda_{m+1})^{-1}$ effectively takes place on the metastable manifold towards the stationary

state [2], as

$$\rho(t) \approx \rho_{\rm ss} + \sum_{k=1}^{m} c_k e^{t\lambda_k} R_k = e^{t\mathcal{L}}\mathcal{P}[\rho(0)], \tag{5.14}$$

cf. Eq. (2.33). We can project to find the evolution generator in this space

$$\mathcal{L}_{\rm MM} = \mathcal{P}\mathcal{L}\mathcal{P}. \tag{5.15}$$

This generator can be now expressed in the basis of the metastable phases, Eq. (5.3), yielding the dynamics in the barycentric coordinates approximating the classical probabilities, $\tilde{\mathbf{p}} = (\tilde{p}_1, .., \tilde{p}_m)$, Eq. (5.6),

$$d\tilde{\mathbf{p}}/dt = \mathcal{L}_{\rm MM}\,\tilde{\mathbf{p}} = C^{-1}\Lambda C\,\tilde{\mathbf{p}}, \tag{5.16}$$

where $(\Lambda)_{kl} := \lambda_k \delta_{kl}$ for $k, l = 1, .., m$ is the diagonal matrix with the low-lying eigenvalues of the master operator.

Entries in each column of $\mathcal{L}_{\rm MM}$ add to 0, which corresponds to probability conservation of the dynamics in the basis of metastable phases. By definition, the long-time evolution, Eq. (5.15), transforms the metastable manifold onto itself. This does not guarantee, however, that the simplex of metastable phases is transformed onto itself, as the evolution may cause states to leave the simplex, which will lead to the initial probability distribution acquiring negative values at later times. Nevertheless, we first note that if the stationary state lays inside any simplex, as all states approach it asymptotically, there exist a time when all states are found within that simplex. Furthermore, if the maximal simplex is a close approximation for the metastable manifold, we expect the reduced master operator to be close to a generator of stochastic classical dynamics between m metastable phases (for $m = 2$ see [4]). Sample evolutions given by this effective operator and transformed into the c_k coordinate system are shown in Fig. 5.2(b).

Dynamics of observable averages and correlations. While the long time evolution of the systems statistics is well described by Eq. (5.16), as we will see below, the short time evolution will differ significantly. This allows metastability to be observed in the behaviour of statistical quantities such as expectation values or autocorrelations of system observables [2, 4, 52]. For the full evolution, we have

$$\begin{aligned} \langle O \rangle(t) &= \mathrm{Tr}\left[O\,\rho(t)\right] = \mathrm{Tr}\left[O\,e^{t\mathcal{L}}\rho(0)\right] \\ &= \langle O \rangle_{\rm ss} + \sum_k c_k\, d_k\, e^{t\lambda_k}, \end{aligned} \tag{5.17}$$

where O is a system observable, e.g. spin magnetisation, and we introduced decomposition into the master operator eigenmodes, $c_k = \mathrm{Tr}[L_k\,\rho(0)]$, $d_k = \mathrm{Tr}(O\,R_k)$, cf. (2.33), with $\langle O\rangle_{\mathrm{ss}} = d_1 = \mathrm{Tr}[O\,\rho_{\mathrm{ss}}]$ being the stationary (static) average. For separation in the master operator spectrum between the real parts of λ_m and λ_{m+1} eigenvalues, at long times $t \gg \tau'$, the exact dynamics (5.17) should be accurately captured by the effective long-time dynamics taking place in the metastable manifold, Eq. (5.15). In this case, the dynamics of an observable O average depends on the evolution of the probability distribution between the metastable phases, Eq. (5.6),

$$\begin{aligned}\langle O\rangle(t) &\approx \langle O\rangle_{\mathrm{ss}} + \sum_{k=2}^{m} c_k\,d_k\,e^{t\lambda_k} \\ &= \mathbf{o}^T\,\tilde{\mathbf{p}}(t) = \mathbf{o}^T\,e^{t\mathcal{L}_{\mathrm{MM}}}\,\tilde{\mathbf{p}},\end{aligned} \tag{5.18}$$

where $(\mathbf{o})_k = \mathrm{Tr}(O\tilde{\rho}_k)$, $k = 1, ..., m$, are the averages of the observable in the metastable phases, and $\tilde{\mathbf{p}}_k = \mathrm{Tr}[\tilde{P}_k\rho(0)]$, see Fig. 5.8(f,g).

Observation of the metastability in expectation values requires preparation of an initial system state different from the stationary state, something often difficult to achieve in experimental settings. Nevertheless, for the system in the stationary state, metastability can also be observed as double-step decay, or a plateau, in the time-autocorrelation of a system observable. This is due to the fact that the first measurement perturbs the stationary state causing its subsequent dynamics. When time between measurements is greater than τ', the state conditioned on the initial measurement relaxes into the metastable manifold and follows the effective dynamics between metastable phases,

$$\begin{aligned}\mathrm{Tr}(\mathcal{O}e^{t\mathcal{L}}\mathcal{O}\rho_{\mathrm{ss}}) &\approx \mathrm{Tr}(\mathcal{O}e^{t\mathcal{L}_{\mathrm{MM}}}\mathcal{P}\mathcal{O}\rho_{\mathrm{ss}}) \\ &= \mathbf{o}^T\,e^{t\mathcal{L}_{\mathrm{MM}}}\,\mathbf{O}\,\mathbf{p}_{\mathrm{ss}},\end{aligned} \tag{5.19}$$

where $\mathcal{O}$ denotes the superoperator representing the measurement of the observable O on a system state, while $\mathbf{O}_{ij} = \mathrm{Tr}[\tilde{P}_i O(\tilde{\rho}_j)]$ and $\mathbf{p}_{\mathrm{ss}}$ is the stationary distribution of ρ_{ss} between the metastable phases [2, 4].

Metastability in dynamics of trajectories. For systems exhibiting metastability in the statistics, the individual evolutions of the system over time typically exhibit *intermittence* (distinct periods of activity isolated in time) or *dynamical heterogeneity* (distinct periods of activity isolated both in time and space) in the emission measurement record or observables (see Fig. 5.2(c)). These features of dynamics can be understood as a consequence of metastable phases differing in

activity or observable averages, as follows. Course graining of quantum trajectories in time on the timescales required for relaxation to metastable manifold, leads to time-coarse-grained system state corresponding to a metastable phase (or their probabilistic mixture if initialised in the superposition of supports of metastable phases), and the coarse-grained trajectory corresponding to transitions between these metastable phases. The timescales of those transitions are exactly captured by the effective dynamics described above, by interpreting $\mathcal{L}_{\mathrm{MM}}$ as a generator of classical stochastic dynamics, (5.16). In particular, the (negative) inverse of the diagonal generator provides the effective lifetime of metastable phases in classical metastable manifolds.

If the metastable phases differ in activity or observable averages, quantum trajectories will inherit these macroscopic properties, leading to intermittence or dynamical heterogeneity characterised by the timescales of the effective dynamics, allowing for metastability to be observed not only on average, cf. Eqs. (5.18) and (5.19), but also in individual realisations in experiments. This connection is further strengthened by the discussion of statistics of quantum trajectories in Sec. 5.3.

5.2 Dissipative quantum East model

We now apply the techniques introduced above to the dissipative quantum East model [5, 40], a generalization of the classical East models studied in relation to glass physics [42, 43]. Such systems classically often exhibit multiple stages of relaxation on different time scales, and we expect such behaviour to occur in their quantum counterparts.

For the quantum model, first consider a system consisting of one 1/2-spin with the Hamiltonian H and jump operators J^- and J^+, see Eq. (2.25),

$$\begin{aligned} H &= \Omega\, S^x, \\ J^- &= \sqrt{\kappa}\, S^-, \\ J^+ &= \sqrt{\gamma}\, S^+, \end{aligned} \tag{5.20}$$

where S^x and $S^\pm = S^x \pm iS^y$ are the spin operators. The Hamiltonian consists of a transverse field causing oscillations in the $|0\rangle$-$|1\rangle$ basis, while S^- can be associated with the photon emission, and S^+ with photon absorption. This

dynamics features a unique stationary state [5],

$$\rho_{\rm ss} = \begin{bmatrix} \frac{\Omega^2+\kappa(\gamma+\kappa)}{(\gamma+\kappa)^2+2\Omega^2} & -i\frac{(\gamma-\kappa)\Omega}{(\gamma+\kappa)^2+2\Omega^2} \\ i\frac{(\gamma-\kappa)\Omega}{(\gamma+\kappa)^2+2\Omega^2} & \frac{\Omega^2+\gamma(\gamma+\kappa)}{(\gamma+\kappa)^2+2\Omega^2} \end{bmatrix}, \tag{5.21}$$

expressed in the basis $|0\rangle$, $|1\rangle$. The many body dynamics is defined using the eigenstates of the resulting stationary state $\rho_{\rm ss}$, the unexcited and excited states $|u\rangle$ and $|e\rangle$, defined so $|u\rangle$ and $|e\rangle$ approach $|0\rangle$ and $|1\rangle$ respectively, as the coherent field Ω tends to 0. The probabilities of these states in the one-body stationary state are its eigenvalues λ_u and λ_e, such that $\rho_{\rm ss} = \lambda_u |u\rangle\langle u| + \lambda_e |e\rangle\langle e|$ (see Ref. [93] for the formulas).

A many-body interacting quantum model is then constructed as follows [5, 81], in analogy to the classical East model. We define a *constraint* operator

$$F_j(p) = (1-p)\mathbb{1}_j + p\,|e\rangle\langle e|_j\,, \tag{5.22}$$

where the subscript j represents the operators acting on j-th spin. The constrained Hamiltonian for the interacting system is then defined as

$$H = \sum_{j=1}^{N} \Omega\, F_{j-1}^2(p) \otimes S_j^x, \tag{5.23}$$

while the constrained jump operators are defined as

$$J_j^- = \sqrt{\kappa}\, F_{j-1}(p) \otimes S_j^-, \tag{5.24}$$

$$J_j^+ = \sqrt{\gamma}\, F_{j-1}(p) \otimes S_j^+, \tag{5.25}$$

where $j = 1, ..., N$, S_j^x and $S_j^\pm$ are the spin operators for j-th spin, cf. (5.20), and we have assumed periodic boundary conditions (i.e. $N \equiv 0$ for the operator indices). The constraint, parametrized by p, is absent when $p = 0$; for $p = 1$ it is hard, i.e., dynamics of the spin $j+1$ only occurs if the state of its neighbour to the left, j-spin, features some probability of being in the excited state $|e\rangle$. For intermediate values of $0 \leq p < 1$, we refer to the constraint as soft.

For the hard constraint, this system possesses two stationary states: a so called dark state disconnected from the rest of the state space where no dynamics occurs due to no constraint being fulfilled, $(|u\rangle\langle u|)^{\otimes N}$, and an active state given by a product state of the stationary state of the single particle system, $\rho_{\rm ss}^{\otimes N}$, see also Ref. [93]. This follows directly from the construction of the dynamics, as the constraint is chosen such that it commutes with the stationary state of the single particle system, and as such the diagonal state

is acted on as if the master operator were that of a non-interacting system. Furthermore, the latter stationary state remains stationary for all values of p.

Despite this simple stationarity, at low temperatures ($\gamma/\kappa \ll 1$) and small values of coherent field ($|\Omega|/\kappa \ll 1$), the dynamics manifests a significant change as p tends to 1, with jumps in trajectories becoming localized both spatially and temporally [40], see Fig. 5.2(c,d): this is referred to as *dynamical heterogeneity*. Note that this change in the dynamics is not related to any static transition in the stationary state, with observables remaining analytic due to the product stationary state $\rho_{\rm ss}^{\otimes N}$. In this section, we will unfold the dynamical structure of the quantum East model using the approach towards classical metastability in open quantum systems outlined in Sec. 5.1. In order to motivate the usefulness of these numerical techniques, we first discuss the approaches via a mean-field approximation and perturbation theory.

Mean-field theory. A common informative treatment of open many-body quantum systems is mean-field theory, often resulting in the prediction of multiple stationary states [3,37]. These stationary states can often be identified with metastable phases in the finite-size system, with the mean-field describing short time evolution into the metastable manifold [4], and long-time dynamics neglected due to the lack of correlations acting as noise on this set of states. It is known that mean-field is ineffective in the classical case ($\Omega = 0$), as the removal of spatial dependence in the state causes the constraint's directionality to be lost. This can also be argued in the quantum model: while the stationary state of the quantum (and classical) East model is homogeneous, the dynamical heterogeneity of trajectories suggests the long time dynamics taking place between states which are not translationally symmetric, and thus cannot be reproduced the homogeneous mean-field ansatz. As such, we will forgo a mean-field treatment.

Perturbation theory. The dynamical heterogeneity is present in the East model dynamics at low temperatures ($\gamma/\kappa \ll 1$), small values of coherent field ($|\Omega|/\kappa \ll 1$), and constraint close to hard ($p \approx 1$, equivalent to $|1-p| \ll 1$). Such separation of scale in the dynamical parameters, motivates the use of non-hermitian perturbation theory [103] for the dynamics with jumps J_j^- featuring the hard constraint, perturbed with respect to the low temperature, the weak coherent field or the soft constraint. In Ref. [93] we derive the first, second, and third-order corrections to the dynamics of the system consisting of any number of spins, together with discussion of the finite size effects. Here we summarise

those results, with further comparisons of the perturbative dynamics with the findings of the approach introduced in Sec. 5.1 in the following sections.

The stationary states of jumps J_j^- and hard constraint correspond to the states which feature none, $|0...0\rangle$, or only isolated excitations $|...010...\rangle$, as such states are dark to any jump operator J_j^-, i.e. the action of the jump operators is 0 on these states. This also leads to all coherences between such states being stationary, so that they form a decoherence free subspace (DFS) [95–97]. Upon perturbing, this DFS becomes a *quantum metastable manifold* and undergoes slow dynamics at the timescales we now discuss [2].

Low temperature. Already in the first order, the perturbative dynamics for $\gamma/\kappa \ll 1$ leads to the decay of the dark DFS towards states with any excitations followed at least by two unexcited sites, i.e., $|0...0\rangle$, $|...00100...\rangle$, with no coherences being stationary any longer. Therefore, the *metastable manifold is classical* in the perturbative regime of low temperatures. Furthermore, in higher orders of γ, excitations are separated by a distance growing exponentially with the order of the corrections, see Ref. [93]. Ultimately, this leads to only two stationary states: the state without any excitations, $|0...0\rangle$, and the uniform state with a single excitation, $N^{-1}\sum_{j=1}^{N}|0...01_j0...0\rangle$, which approximate, in the zero order of γ, the two stationary states at $p = 1$. Softening of the hard constraint, in the regime $|1-p| \ll 1$, leads additionally to *detailed balance dynamics* featuring removal and reintroduction of isolated excitations, with the rates proportional to $\kappa(1-p)^2$ and $\gamma(1-p)^2$, respectively, which facilitates a unique stationary state, see Ref. [93].

Weak coherent field. Here, the perturbation in Ω introduces both the Hamiltonian and the change of constraints, cf. Eqs. (5.23) and (5.24). In Ref. [93] we show there are no odd-order corrections in Ω to the dynamics. Furthermore, the second-order corrections correspond to dephasing of all coherences in the DFS, with probabilistic mixtures of the states of none, $|0...0\rangle$, or only isolated excitations $|...010...\rangle$, remaining stationary, the first order-corrections to the state structure introduce the rotation of $|0\rangle$ and $|1\rangle$ towards $|u\rangle$ and $|e\rangle$. Therefore, we again conclude that the *metastable manifold is classical*. Although this is analogous to the perturbative dynamics due to γ, the dynamics of excitations can take place at earliest in the forth-order. Moreover, the stationary state, cf. (5.21), which has probabilities $\lambda_u = 1 - \lambda_e = 1 - \gamma/\kappa - 16\Omega^4/\kappa^4 + ...$ (see Ref. [93]), suggests that the coherent field in the forth order may play an analogous role to the temperature, but in the rotated basis $|u\rangle$, $|e\rangle$. Due to

complexity of forth-order perturbation theory, we will instead investigate this hypothesis using the approach of Sec. 5.1.

Finally, we note that the perturbations in the temperature, the coherent field, or softness of the constraint, are local, cf. Eqs. (5.23) and (5.24). Therefore, the timescales of the resulting perturbative dynamics can be proportional to the system size, which significantly limits the validity of the perturbation theory, to $\gamma N \ll \kappa$, $|\Omega| N \ll \kappa$, and $|1-p| N \ll \kappa$ (as $\kappa/2$ is the slowest eigenvalue of the dynamics with J^- at the hard constraint). This system-size dependent regime is not an issue for the numerical methods of Sec. 5.1, which we now discuss.

5.2.1 Accuracy of the simplex approximation

We begin by constructing the classical MM over a range of parameters and testing the accuracy of the resulting simplex.

First, we check for what parameters there exist suitable gaps in the spectrum to carry out the construction. This is done for $N = 6$ in Fig. 5.4(a,b) (which is the system size discussed in the rest of the chapter). There exist gaps between the 7th and 8th (here $m = 7$), and 10th and 11th eigenvalues (here $m = 10$), for different ranges of parameters, including points outside the regime of applicability for perturbation theory. In a certain region of parameters both of these gaps occur: this will lead to a hierarchy of classical MMs [80], which we discuss in the next Sec. 5.2.2.

With the presence of these gaps in the spectrum we can now apply the computational approach discussed in Sec. 5.1 and sketched in Fig. 5.3. We first consider $2(m-1)r$ ($m = 7, 10$) candidate states originating from the extreme eigenstates of r random rotations of the left eigenmatrices, before clustering those found near each other, and then generating cycles under the translation symmetry (of possible length 1, 2, 3 and 6 for $N = 6$ spins). Finally, we choose a maximal simplex formed by m metastable states solely chosen as the complete approximate cycles of the representatives (e.g. for $m = 7$, it could be in general chosen as cycles of length 1 and 6, or two cycles of length 2 and a single cycle of length 3, etc.), which defines m metastable phases, the properties of which we discuss in the next Sec. 5.2.2.

The dual basis to the chosen metastable phases can be directly used to test the classicality of the metastable manifold. The probability operators Eq. (5.4) need to be diagonalized, and their eigenvalues analysed as in Eqs. (5.8) and (5.9), which provides us with an estimate of the simplexes accuracy. In

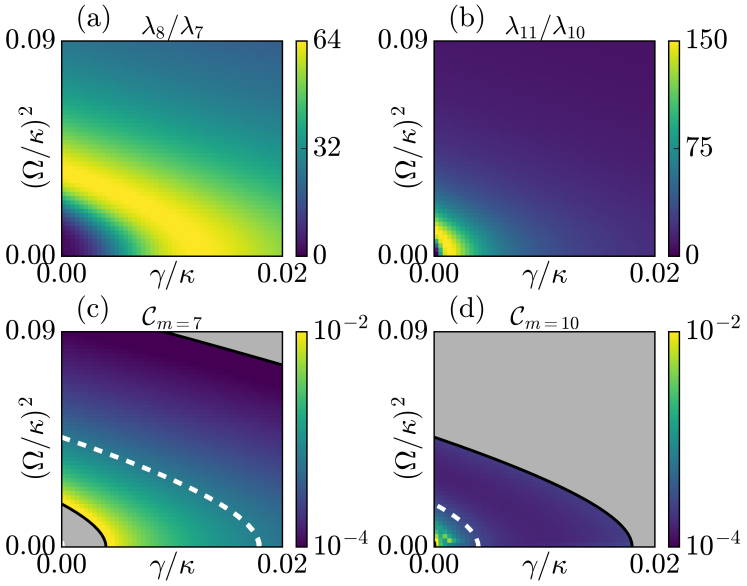


Figure 5.4: Separation in master operator spectrum and classicality: (a-b) The ratios of the master operator eigenvalues (the real parts) demonstrate two gaps in the spectrum at $m = 7, 10$ for $N = 6$ spins, which shows a hierarchy of MMs in the quantum East model. (c-d) The classicality $D^{-1}\sum_{k=1}^{m}\sum_{l=1}^{D}[\max(-\lambda_k^{(l)}, 0) + \max(\lambda_k^{(l)} - 1, 0) \geq \mathcal{C} \geq \mathcal{C}_{\max}$, see Eq. (5.8) and (5.9), of the MM construction for $m = 7$ (c), and $m = 10$ (d), rescaled by the Hilbert space size $D = 2^6$. Softness $p = 0.99$.

Fig. 5.4(c,d) we observe that the metastable manifold with $m = 7$ is well approximated by 7 metastable phases for broad regime of low temperatures and weak coherent fields, but with their values above a certain threshold (black line with grey region below). This parameter regime directly corresponds to the large separation at $m = 7$ in the master operator spectrum, cf. Fig. 5.4(a). Below the threshold, the metastable manifold instead consists of $m = 10$ metastable phases, cf. Fig. 5.4(d) (with the threshold denoted by white dashed line): these remain metastable also above the threshold, but for a smaller range of values of the field and temperature than in the case of $m = 7$. This is again a consequence of the presence of the separation in the master operator spectrum at $m = 10$ for a smaller parameter regime than at $m = 7$, cf. Fig. 5.4(a,b). Nevertheless, we can conclude that the existing *metastable manifolds are classical* for low temperatures and weak coherent fields, except negligibly small values where, at finite softness, both for $m = 7$ and $m = 10$ the separation in the spectrum disappears, cf. Fig. 5.4(a,b). This is in the complete agreement with the perturbation theory results derived in Ref. [93], which predict emergence of a classical manifold from a quantum metastable manifold at small temperature or weak coherent field (but not in the case of only softening the constraint, cf. Ref. [93]). In the rest of this chapter, we will focus at the case when there exists a gap in the master operators at $m = 10$ [below white dashed line in Fig. 5.4(c)].

5.2.2 Metastable phases

We now discuss the properties of the metastable phases forming the classical metastable manifold and their relation to the translation symmetry.

Metastable phases. In Fig. 5.5(a) we show the spin magnetisation along z-axis for the metastable phases. For $m = 7$ (first two rows, above the white dashed line), the metastable manifold consist of the state with all spins down (no excitation), and six states with a single spin up (a single excitation). For $m = 10$, the manifold additionally contains three states with two excitations at maximally separated sites, i.e. followed by two empty sites [see third row in Fig. 5.5(a)]. This is exactly the structure of the metastable manifold we obtained in the first order perturbation theory for temperature (see Ref. [93]), but now we have confirmed that the case of coherent field is analogous. As the probability of a spin up or down seems to decrease with the stronger coherent field, we also confirm (see the insets), that the spins in metastable phases

are actually aligned with the rotated eigenbasis, $|u\rangle$ and $|e\rangle$, of the stationary state, (5.21). Therefore, the metastable phases can be approximately viewed as $|uuuuuu\rangle$, $|euuuuu\rangle$, $|euueuu\rangle$ and their translations, which are orthogonal due to different number of excitations, or their positions in space, cf. Sec. 5.1.2. These states are stable since the presence of an excited spin facilitates dynamics on the spin to its right, in turn facilitating dynamics further along the chain: the states which are metastable feature excitations as separated as possible, thus relaxing the slowest.

The dynamics facilitated by these excitations cause photon emissions from their right neighbour, resulting in the metastable state, an average over trajectories in this phase, containing a mixture of many similar pure states with the same excitations. We demonstrate this mixing by displaying the purity of the metastable states in Fig. 5.5(b). The states with a single or double excitation feature a purity slightly below 1, cf. Fig 5.2(d), with a lower purity for the state with more excitations as a result of more emissions and thus greater mixing. We have observed this behaviour in the first-order perturbative corrections due to temperature, with purity lowered proportionally to γ/κ, while Fig. 5.5(b) suggests it is also the case for the coherent field, contributing as Ω^4/κ^4.

Translation symmetry. The phases discussed above feature three groups distinguished by the number of excitations; as mentioned previously, any metastable manifold must be invariant under the systems symmetries. Furthermore, for any classical metastable manifold, the set of metastable phases must be invariant under such symmetries, which simply permute the metastable phases. In particular, the size of invariant subsets of metastable phases is determined by the orders of the symmetry subgroups. In the case of the dissipative quantum East model with translation symmetry due to the periodic boundary conditions, $N = 6$ spins results in four subgroups, the group itself, the identity, and subgroups of order 2 and 3. Indeed, in Fig. 5.5(a), for the region of spectrum separation between the 10th and 11th eigenvalues ($m = 10$) the subgroups of order 1, 6, and 3 correspond to the cycles of the metastable phases with none, single, and double excitations, respectively. When the gap between the 7th and 8th eigenvalues is also present (parameters above the white dashed line), the metastable manifold with longer lived states ($m = 7$), due to the cycles composing the $m = 10$ MM, necessarily includes only none or a single excitations.

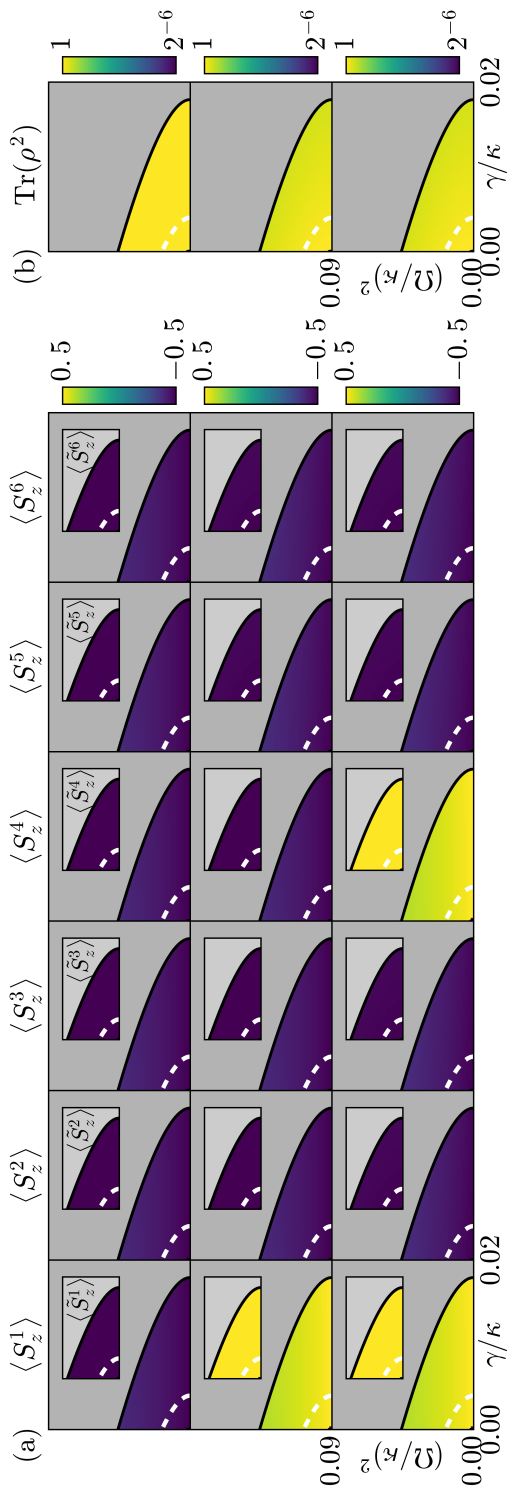


Figure 5.5: Classical metastable manifold of the dissipative quantum East model: (a) The site-wise z magnetisation, for the metastable phases: dark state, and examples of the single and double excitation states, respectively. The MM contains all translations of these single (6 states) and double excitation states (3 states). The insets show the site-wise z magnetisation in the $|u\rangle$, $|e\rangle$ basis, defined as $\tilde{S}_z^j = (|e\rangle\langle e|_j - |u\rangle\langle u|_j)/2$ for j-th spin. (b) The purities of the metastable phases, chosen as in (a).

5.2.3 Effective dynamics and comparison to the classical East model

Classical stochastic dynamics. The long time-dynamics $\mathcal{L}_{\mathrm{MM}}$ taking place between the phases discussed in Sec. 5.2.2, see Eq. (5.15), can be understood by considering the master operator projected on the metastable manifold, (see Eq. (5.16), see Fig. 5.6(a)).

In the previous Sec. 5.2.1, we have shown that the metastable manifold is well approximated by m disjoint metastable phases, i.e. any metastable state can be approximated by a probability distribution between the metastable phases – its barycentric coordinates. Therefore, we expect the reduced master operator to be close to a generator of stochastic classical dynamics on these probability distributions: it should be be both positivity preserving and probability conserving, the later of which is guaranteed by construction, see Sec. 5.1.3.

Positivity of the dynamics corresponds in the stochastic generator to the negativity of the diagonal elements and positivity of the off-diagonal elements. Therefore, in order to quantify how close the effective master operator is to positive dynamics on the simplex, we define a stochastic generator $\mathcal{L}^{+}_{\mathrm{MM}}$ constructed by replacing any negative off-diagonal components in $\mathcal{L}_{\mathrm{MM}}$ by zero, while simultaneously increasing the magnitude of diagonal elements to maintain probability conservation (the columns summing to 0). We then calculate the distance between the two operators, using the norm induced by the L_1-norm of probability distributions, $\|\mathcal{X}\|_1 = \sup_{\mathbf{p}\geq 0,\,|\mathbf{p}|_1=1} |\mathcal{X}\mathbf{p}|_1$, corresponding to the maximal L_1-norm among the columns in $\mathcal{X}$. We thus consider

$$\Delta^{+} = \frac{\left\|\mathcal{L}_{\mathrm{MM}} - \mathcal{L}^{+}_{\mathrm{MM}}\right\|_1}{\left\|\mathcal{L}_{\mathrm{MM}}\right\|_1 + \left\|\mathcal{L}^{+}_{\mathrm{MM}}\right\|_1}, \tag{5.26}$$

where we additionally rescale by the individual operator norms, in order to obtain $0 \leq \Delta^{+} \leq 1$. We plot Δ^{+} for the long-time dynamics in the dissipative quantum East model in Fig. 5.6(b): we observe values much smaller than 1 across the entire metastable region of the parameter space, confirming the *effective dynamics is well approximated by stochastic classical dynamics.*

Detailed balance in the effective dynamics. Reassured this is an accurate classical description of the long time dynamics, we now demonstrate how this construction may be used to study its physical properties. We seek to compare with the classical East model ($\Omega = 0$). In particular, the classical model features detailed balance: there are no stationary currents between 2^N configurations of

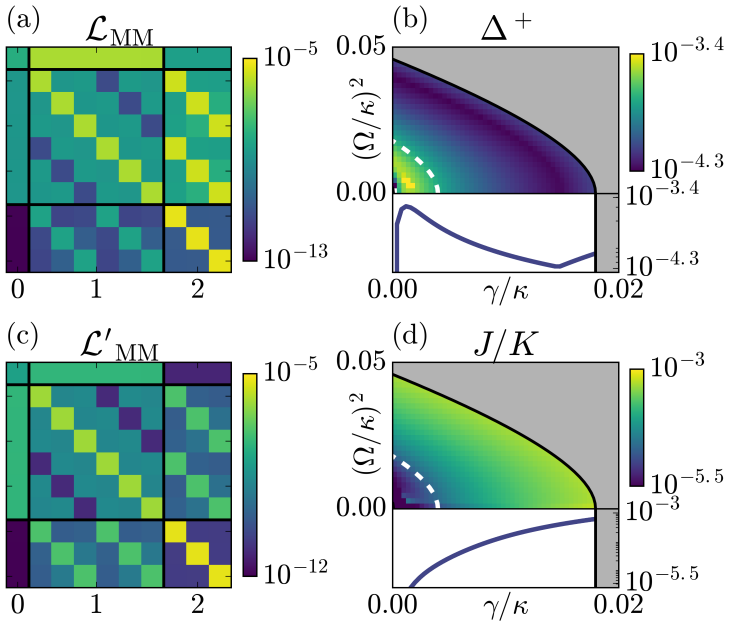


Figure 5.6: Effective long-time dynamics: (a) Absolute values of the effective master operator entries in the basis of metastable phases for $\Omega/\kappa = 0.024$, $\gamma/\kappa = 0.0016$ and $m = 10$. Diagonal elements are negative while off-diagonal are approximately positive. The horizontal labels indicate the number of excitations in a metastable phase, delineated by the vertical black lines. The horizontal lines indicate the same for the vertical axis. (b) The distance to a positive stochastic generator, Eq. (5.26), over (top) the metastable region of the parameter space and (bottom) the classical $\Omega/\kappa = 0$ cross section. (c) Absolute values of entries in the similarity-transformed effective master operator $\mathcal{L}'_{\mathrm{MM}}$ display the transposition symmetry associated with the detailed balance. Furthermore, the diagonal elements are negative while all the off-diagonal are positive. (d) The ratio of the total current and total activity in the stationary state, see Eqs. (5.29) and (5.30) confirms the detailed balance being present within the metastable region.

the classical system (spins up or down), i.e.,

$$(\mathcal{W})_{ij}\,(\mathbf{p}_{\rm ss})_j - (\mathcal{W})_{ji}\,(\mathbf{p}_{\rm ss})_i = 0, \tag{5.27}$$

where we denoted by $\mathcal{W}$ the projection of $\mathcal{L}$ onto probability distributions over the classical configurations (indexed by i and j), and $\mathbf{p}_{ss}$ denotes the stationary distribution.

Detailed balance implies the existence of a similarity transformation which renders the operator hermitian

$$\mathcal{W}' = \mathrm{diag}(\tilde{\mathbf{p}}_{\rm ss})^{-1/2}\mathcal{W}\,\mathrm{diag}(\tilde{\mathbf{p}}_{\rm ss})^{1/2}, \tag{5.28}$$

where hermiticity, $\mathcal{W} \approx \mathcal{W}'^{T}$ follows component wise from Eq. (5.27). To check our effective description has detailed balance, we can apply this transformation to $\mathcal{L}_{\rm MM}$, with $\tilde{\mathbf{p}}_{\rm ss}$ given by projecting the stationary state $\rho_{\rm ss}^{\otimes N}$ over the metastable phases. Despite the underlying quantum dynamics caused by coherent driving from the Hamiltonian, we observe that the effective dynamics becomes approximately symmetric, see Fig. 5.6(c).

Furthermore, we can directly quantify how well the system satisfies detailed balance: we consider the ratio of the total current J to the total activity K in the stationary state associated to the effective master operator,

$$J = \sum_{k,l>k} \left|(\mathcal{L}_{\rm MM})_{kl}\,(\tilde{\mathbf{p}}_{\rm ss})_l - (\mathcal{L}_{\rm MM})_{lk}\,(\tilde{\mathbf{p}}_{\rm ss})_k\right|, \tag{5.29}$$

$$K = \sum_{k,l>k} (\mathcal{L}_{\rm MM})_{kl}\,(\tilde{\mathbf{p}}_{\rm ss})_l + (\mathcal{L}_{\rm MM})_{lk}\,(\tilde{\mathbf{p}}_{\rm ss})_k\,. \tag{5.30}$$

If the currents are negligible relative to the activity, the model essentially has detailed balance. In Fig. 5.6(d), we indeed observe that the current across all metastable parameters is small compared to the system's activity; in comparison, the classical East model also features approximate detailed balance when restricted to the metastable manifold.

In perturbation theory, these results can be traced back to the fact that dynamics between system configurations, in the leading order in γ or $(1-p)^2$, only introduces or removes one excitation at a time, or shifts a single excitation. The result is the same ladder structure as the classical dynamics (for homogeneous states), thus necessarily implying the detailed balance (while the approximation worsens for larger γ), see Ref. [93] for details. Approximate detailed balance also in the presence of a weak coherent field, Fig. 5.6(d), suggests that a similar mechanism may be responsible for the long-time dynamics in

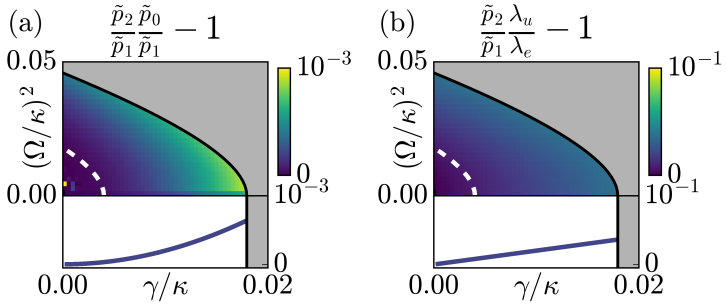


Figure 5.7: Stationary state properties: (a) The free energy of the metastable phases does not depend on the number of interactions, as the ratio of the stationary probabilities between the state with a single excitation and the unexcited state, $\tilde{p}_1/\tilde{p}_0$ approximately equals the ratio of the probabilities for a double excitation and a single excitation $\tilde{p}_2/\tilde{p}_1$. (b) The ratio $\tilde{p}_1/\tilde{p}_0$ actually corresponds to the ratio of the stationary probabilities in as single state dynamics, Eq. (5.21), of the excited state, λ_e, and unexcited state, λ_u. Both plots are shown over (top) the metastable region of the parameter space and (bottom) the classical $\Omega/\kappa = 0$ cross section.

the quantum East model. This is indeed confirmed for the parameters chosen in Fig. 5.6(a): the most probable transitions (yellow-light green) are associated with the removal of the second excitation, or removal of a single excitation towards the unexcited state; the less likely transitions (green) correspond to a shift of a single excitation, the introduction of one excitation, or removal of two excitations; the least likely transitions (blue) correspond to the the introduction of two excitations simultaneously, or shift of two excitations [see also Fig. 5.8(b,c)].

Non-interacting structure of the stationary state. Since the long-time dynamics system possesses detailed balance, the stationary state of the effective master operator is thermal: we now discuss the effective free energy function defining this thermal stationary state. In the full classical East model, whose stationary state is also a product state, the free energy is simply a function of the number of excitations, but not their relative distance (i.e. it is not dependent on any type of interactions). Due to the exponential form of a thermal distribution, this can be tested by considering ratios of state probabilities: the exponents only state dependence will be a linear function of the number of excitations. We test this property in Fig. 5.7(a) for the quantum East model using the distribution of the stationary state over the metastable phases, by comparing the ratio of probabilities of finding the stationary state in one of the single or double excited states, $\tilde{p}_2/\tilde{p}_1$, to the ratio of finding it in the unexcited state or

one of the single excitation states, $\tilde{p}_1/\tilde{p}_0$. We find that as in the classical East model, in the quantum model interactions do not play a role in the free energy of the metastable phases.

Furthermore, the free energy per excitation is directly determined by the ratio of probabilities for excited and unexcited states in the single-site dynamics, see Fig. 5.7(b). This is again the consequence of the product structure of the stationary state, and the metastable states being approximated simply as states with a single or double excitations, cf. Fig. 5.5(a), which appear as the leading order corrections to the stationary state above the no-excitation contribution [2]. Therefore, the error of this non-interacting approximation of the free energy will increase as with growing temperatures and coherent field values, cf. Fig. 5.7(b).

5.2.4 Effective lifetimes and dynamical heterogeneity

As mentioned previously in Sec. 5.1.3, the long-time dynamics between metastable phases are directly related to quantum trajectories: lifetimes for trajectories to remain identifiable with these phases, and the transition rates between these distinct periods, are described by the effective master operator of Eq. (5.16). We discuss this correspondence in detail now.

Lifetime of metastable phases. The effective lifetimes of the metastable phases are given by the inverse magnitude of the diagonal elements of the effective master operators, (5.16). By translation symmetry of the metastable manifold, the lifetimes of states related by the symmetry must be the same, i.e., we only have three different timescales: the lifetime τ_0 of the homogeneous unexcited state, the lifetime τ_1 of six states with a single excitation, and the lifetime τ_2 of three states with double excitations, which are shown for the parameter regime leading to metastable dynamics in Fig. 5.8(a).

The unexcited state is the longest lived metastable phase. Note that this metastable phase can only be can only be excited due to the softness of constraint in H or J_j^+ (for any $j = 1, ..., N$), cf. (5.24), which thus takes places at the rate proportional to $N(1-p)^2(\Omega^2/\kappa+\gamma)+...$ [in the perturbative regime $|1-p| \ll 1$, see Ref. [93]], where the dependence of the rate on the system size is due to the translation symmetry: the excitation can be introduced in any

[2] In the case of the classical model ($\Omega = 0$), in the perturbative regime, the metastable manifold is known to consist of isolated excitations at any system size (see Ref. [93]), and thus the free energy over metastable phases is again only the function of number of excitations, and so we can expect, also in the quantum East model for larger system sizes

of N spins. In contrast, the removal of a single excitation at j-th spin, again requires the softness of constraint in J_j^- (or in H, which however is of lower order), and thus takes place at the faster rate $\kappa(1-p)^2 + ...$, leading to the separation of timescales $\tau_1/\tau_0 \approx N(\Omega^2/\kappa^2 + \gamma/\kappa)$.

Furthermore, in the parameter region where two gaps are present in the master operator spectrum [above the white dashed line in Fig. 5.8(a)], we know from Sec. 5.2.2 that the hierarchy of metastable manifolds exists ($m = 7, 10$). This is manifested in the distinct values of the lifetimes τ_1 and τ_2 of the metastable phases with single and double excitations, respectively; with a single gap in the master operator spectrum ($m = 10$, below the white dashed line), their lifetimes are necessarily comparable. We note that the softness of constraint causes the removal rate of an excitation from metastable phases with a single excitation and double excitation to be the same (except from the fact that two possible sites to decay in the double excited state), while for hard constraint only the second excitation can be removed due to the temperature of the coherent field (by flipping the unexcited spins between two excitations which allows for the hard constraint to be fulfilled). When the constraint is soft, the absence or presence of separation between τ_1 and τ_2 is determined by the softness-induced and temperature-induced dynamics being faster, respectively. In Fig. 5.8(a), the regime of smaller (greater) γ and Ω below (above) the threshold corresponds to the former (latter) process being the fundamental mechanism in relaxation of the metastable phase with double excitation towards the stationary state.

Structure of effective stochastic dynamics generator. In Fig. 5.8(b,c) we show examples of the effective master operator for two sets of parameters, indicated by the crosses in Fig. 5.8(a), corresponding to the cases with a single MM and the hierarchy of two MMs, respectively.

In both cases, a double excitation phase is most likely transformed into two single excitation phases (equally likely due to the translation symmetry by 3 sites of the double excitation phase), with one excitation inducing relaxation of the other. A single excitation phase is most likely transformed into no-excitation phase, which in turn gets excited most likely with only a single excitation (into one of six single-excitation phases). This ladder structure of the effective classical dynamics supports detailed balance in the dynamics, as we discussed in detail in Sec. 5.2.3.

Beyond those leading order transformations, however, shifts of a single

excitations are possible due to two different mechanisms. In Fig. 5.8(c) we observe that the shift a single excitation is possible to all sites except that corresponding to the possible position of a second excitation, in which case the second excitation is introduced instead. This indicates that the shift is actually facilitated by the introduction of excitations and their subsequent decay, which can be facilitated either by several excitations by the temperature/coherent field or softness of constraint allowing for introduction of excitations directly in unexcited sites. The uniform probability of shifts to different sites in Fig. 5.8(c), suggest that the two processes contribute equally, while, in the case of two MMS in Fig. 5.8(d), the larger values of the coherent field and temperature dominate the latter process and only some shifts are possible. This is directly supported by the perturbation results in the classical model, see Ref. [93]. We note that due to small system size $N = 6$ and the translation symmetry of the MM, there is no apparent directionality in the dynamics for both cases: we would in general expect this to follow from the presence of the constraint to the left, cf. Eqs. (5.23) and (5.24), and is present in perturbation theory for larger system sizes.

Nevertheless, in both cases, the unexcited metastable lifetime is much longer than the metastable phases with a single or double excitations, so that in the trajectories of the classical effective operator most time is spent in the unexcited state. Excitations are thus present at isolated moments in time; these periods are also isolated in space, due to the symmetry structure of the metastable manifold (see also Ref. [93]). As we discuss next, this structure of the time and space separation corresponds directly to *dynamical heterogeneity* observed in photon emissions in the quantum East model also for larger system sizes [5, 40].

Metastability in quantum trajectories as dynamical heterogeneity. We now discuss how the spectral gaps in the master operators manifest in the emission activity of individual experimental realisations of the evolution.

First, let us consider dynamics in the case of the state being (on average) in one of the metastable phases. An excitation of site $(j-1)$ in a metastable phase fulfils the hard constraint of the single spin dynamics of the j-th spin, cf. Eqs. (5.20), (5.23) and (5.24), thus enabling its relaxation towards the stationary state (5.21). Therefore, for the system initialised in such a state, for times before the effective dynamics in the metastable manifold takes place and the metastable phase is changed, $t \ll \tau' \equiv (-\mathrm{Re}\lambda_m)^{-1}$, in an individual realisation of an experiment (or quantum trajectories obtained in QJMC simulations), we can

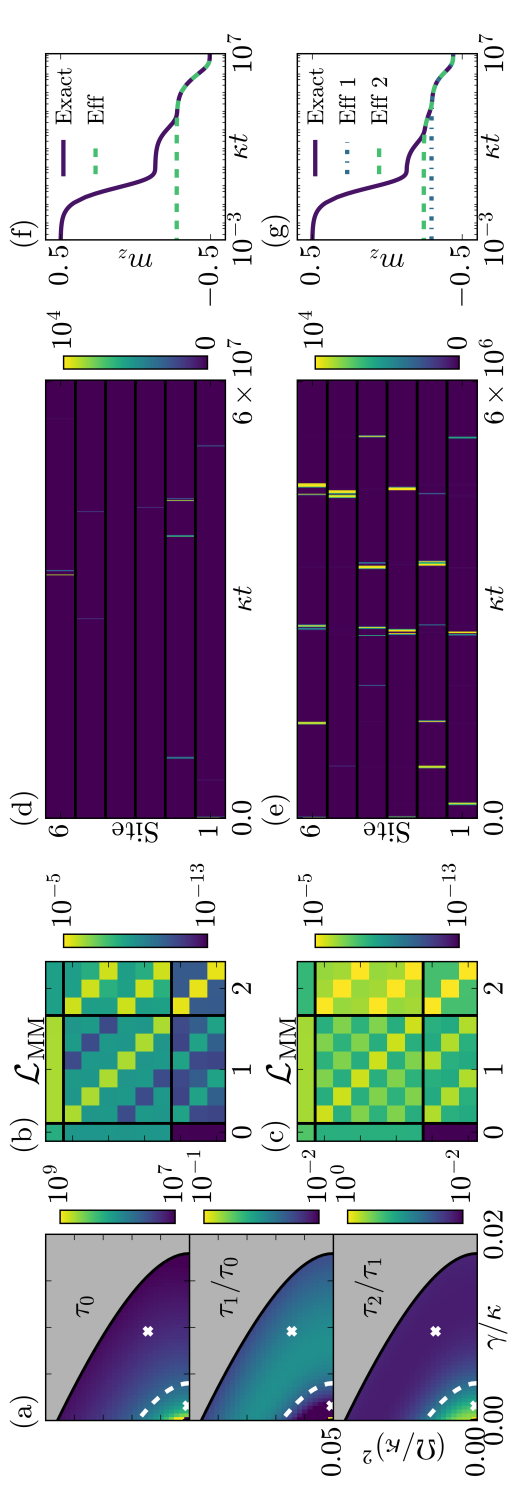


Figure 5.8: Effective stochastic dynamics and quantum trajectories: (a) Effective lifetimes of the metastable phase in the MM as a function of the parameters, plotted relative to the next longest lifetime. Here τ_0 is the lifetime of the dark state, τ_1 the lifetime of states with a single excitation, and τ_2 the lifetime of states with two excitations. (b,c) The component magnitudes of the effective master operators for (b) $\Omega/\kappa = 0.024$, $\gamma/\kappa = 0.0016$ and (c) $\Omega/\kappa = 0.12$, $\gamma/\kappa = 0.0096$. (d,e) Sample QJMC trajectories corresponding to (b,c) respectively. Trajectories are split into 500 time-bins for which the total activity of jumps J_j^- (photon emissions from j-th spin) within each bin is plotted, see Eq. (5.24). Note the presence of simultaneous excitations from two sites. (f,g) Exact (solid) and effective (dashed, dash-dotted) evolution of the total z magnetisation from an initial all up state, corresponding to (b,c) respectively.

expect photon emissions to take place on the site j at the rate $\mathrm{Tr}[(J^-)_j^\dagger J_j^- \rho_{\mathrm{ss}}] = \langle 1|\rho_{\mathrm{ss}}|1\rangle \approx \Omega^2/\kappa + \gamma + ...$ This site will thus appear brighter for higher temperature of coherent field values, see Fig. 5.8(d,e); phases will emit a quantity of photons proportional to the number of excitations, distinguishing them within a trajectory. In contrast, for the unexcited metastable phase, the hard constraint in the dynamics is not fulfilled, and therefore, this phase will appear *dark* in quantum trajectories, before softness in the constraint will allow for the introduction of a single excitation, at $t \geq \tau'$.

At longer times, higher-order processes introducing several excitations or exploiting softness of constraint will become non-negligible on average, contributing to the long-time dynamics of the metastable phases by connecting disjoint parts of system space. In individual quantum trajectories these processes will take place separately and at fluctuating times, but will typically be followed by the fast decay of excitations due to satisfied hard constraints (on timescales $t \ll \tau'$) towards another metastable phase. Therefore, a time coarse-graining of quantum trajectories will lead to the system transitioning only between metastable phases. On the other hand, an average over trajectories must return the evolution of the master operator, Eq. (2.25), while projecting the averaged state onto the MM yields a probability distribution over metastable phases evolving according to the classical stochastic generator, Eq. (5.15). Therefore, the transitions in coarse-grained quantum trajectories must be governed by the same effective generator. This is corroborated in Fig. 5.8(b,c), where, correspondingly with the transition rates of the effective stochastic generator, in the case of a single MM, mostly transitions between the excited states and dark states are observed; meanwhile for two MMs, there is also a significant presence of transitions between states with a single excitation (excitation shifts).

We conclude that the classical trajectories over the metastable phases generated by $\mathcal{L}_{\mathrm{MM}}$, Eq. (5.15), can be viewed as a result of *temporal coarse graining of quantum trajectories* in the full dynamics. In particular, the dynamical heterogeneity in the quantum trajectories, is the microscopic counterpart to the classical stochastic jumps between the unexcited phase and the phases with a single excitation, which can be directly identified with the dynamical phases of none or a localised activity (photon emissions from the site neighbouring with the excitation).

We have observed that the classical metastability of the system dynamics

manifests itself also in the behaviour of individual quantum trajectories of the system evolution, e.g. by the intermittence [4] or dynamical heterogeneity, when the metastable phases are characterised by different dynamical behaviour. Furthermore, as we show in Sec. 5.3, the above discussion can be generalised to any set of classical metastable phases which differ in activity, and thus the connection between time-coarse grained quantum trajectories and stochastic dynamics of metastable phases is fully general.

Metastability in dynamics of observable averages. This dynamical heterogeneity induces a plateau structure in the model's statistical properties, as a result of the differing lifetimes of distinct metastable states. This can be observed in the behaviour of statistical quantities such as expectation values or autocorrelations of system observables [2, 4, 52], manifesting as a double-step decay in the quantum East model for $N = 6$ sites.

As discussed in Sec. 5.1.3, plateaus in the decay of averages and correlations, can be captured by the long-time effective dynamics in the metastable manifold, for times $t \gg \tau' \equiv (-\mathrm{Re}\lambda_{m+1})^{-1}$, see Eqs. (5.18) and (5.19). We demonstrate this in Fig. 5.8(f,g) for the total magnetisation $m_z = 1/N \sum_i \langle S_i^z \rangle$, initialized from the all up state. Indeed we observe an excellent agreement at long times between the exact and effective dynamics, in the both cases with one and two MMs, which correspond to one or two plateaus in the dynamics, respectively. These plateaus exhibit the time regimes of system metastability, and are consequently reproduced by the effective dynamics in the MM.

Physically, we note that the observable S_z effectively counts the number of excitations, and thus the initial decay corresponds to the removal of excitations towards two isolated or a single excitation, which appear stationary in the metastable regime. After the metastable regime, further relaxation towards either the stationary state or metastable phases with no or a single excitation takes place according to the long time effective dynamics. Interestingly, in both cases, the exact dynamics features an additional (anomalous) plateau at earlier times, which is not due to any further gap present in the spectrum of the master operator, but results instead from the zero overlap of either the observable or the initial state with many eigenmodes (not due to their translational symmetry), cf. Eqs. (5.1) and (5.17), resulting in an effective gap in the eigenvalues of master operator which actually contribute to the dynamics, and thus an *effective metastability*, see also Fig. 5.9.

5.3 Thermodynamics of trajectories

In some systems the metastability can be a collective effect emerging as the system size increases [4]. If large system sizes are required for prominent metastability, exact diagonalization may be infeasible, a requirement for the procedure to unfold classical metastable manifolds proposed in Sec. 5.1 and applied to the dissipative quantum East model in Sec. 5.2. Here we introduce an alternative numerical approach to classical metastable manifolds using quantum jump Monte Carlo simulations [24] and biased sampling in the framework of so-called thermodynamics of trajectories, based on large deviation theory. Applied extensively in classical equilibrium statistical mechanics and stochastic systems (for a detailed review see [6]), biased sampling can also be applied to open quantum systems [3, 39, 40, 82].

Thermodynamics of trajectories. Consider a time-integrated observable $K(t)$ related to jumps in the system dynamics, e.g. the total number of jumps $K(t)$ occurring in a quantum trajectory of length t. If the probability of observing a given value of $K(t)$ is biased according to that value, not only the typical trajectories, but also rare events, i.e. the tails/large deviations in the probability distribution, can be studied. Here we will show that biasing of quantum trajectories allows for accessing, via the average over time or over trajectories, not only the stationary state, but also the metastable states.

Let $P[K(t), t]$ be the probability of a trajectory of length t having undergone $K(t)$ jumps. Since this is a time averaged observable in the large time limit, we expect that the probability asymptotically takes a large deviation form $P[K(t), t] \propto e^{-t\phi(k)}$ for the activity $k = K(t)/t$ [39]. On the other hand, we may bias the probability distribution, corresponding to a moment generating function $Z(s, t)$,

$$Z(s,t) = \sum_{K(t)=0}^{\infty} P[K(t), t]\, e^{-sK(t)} \propto e^{-t\theta(s)}, \tag{5.31}$$

which in the long time limit also takes the large deviation form with rate function $\theta(s)$, related to $\phi(k)$ via the Legendre transform. In particular, $\theta(s)$ corresponds to the *scaled cumulant generating function*, $\log[Z(s, t)]/t$ and can be found using the numerical and analytical techniques of large deviation theory (see [7, 8] for examples of classical numerical techniques).

Biasing on the ensemble of trajectories can be incorporated directly into the master equation, (2.25), by introducing an additional factor in the dissipative

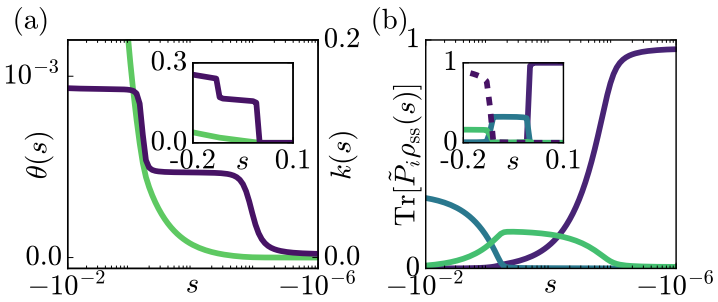


Figure 5.9: Biased sampling for metastable phases: (a) The leading eigenvalue (rate function) $\theta(s)$ (light) of the biased master operator, Eq. (5.32), for the quantum East model, and the corresponding activity $k(s)$ (dark), plotted on a log scale for negative values of s. Here bias is applied to total activity, i.e. all jump operators. The inset shows a larger range of parameters on a linear scale. (b) The projection of the stationary state of the biased dynamical onto the metastable manifold: the dark state (dark), a single excited phase (light) and a two-excitation phase (intermediate). The inset shows a larger range of parameters, along with the distance between the state and its projection on the metastable manifold (dashed). In (a,b) $\Omega/\kappa = 0.15$, $\gamma/\kappa = 0.0004$ and $p = 0.999$, while $\theta(s)$ and $\rho_{\mathrm{ss}}(s)$ were obtained by numerical diagonalisation of $\mathcal{L}_s$.

part related to jump occurrence [3, 39],

$$\begin{aligned}\mathcal{L}_s(\rho) &= -i[H,\rho] + e^{-s}\sum_j \left[J_j\rho\, J_j^\dagger - \frac{1}{2}\{J_j^\dagger J_j,\rho\}\right] \\ &= \mathcal{L}(\rho) + \left(e^{-s}-1\right)\sum_j J_j\rho\, J_j^\dagger,\end{aligned} \tag{5.32}$$

so that

$$Z(s,t) = \mathrm{Tr}\left(e^{t\mathcal{L}_s}\rho\right), \tag{5.33}$$

for the initial state ρ. The eigenvalue of $\mathcal{L}_s$ with the largest real part corresponds to $\theta(s)$, while for small s the associated eigenmatrix $\rho_{\mathrm{ss}}(s)$ is the stationary state of the system with dynamics biased according to their activity, $\mathcal{L}_s\,\rho_{\mathrm{ss}}(s) = \theta(s)\,\rho_{\mathrm{ss}}(s)$. In particular, values of s where the leading eigenvalue is not unique lead to non-analyticities in $\theta(s)$, recognised as first-order *dynamical phase transitions* [39], with the associated sharp changes in the rate function derivative $k(s) = -\partial_s\theta(s)$ related to the activity in $\rho_{\mathrm{ss}}(s)$. This is analogous to non-analyticities in the free energy in equilibrium statistical mechanics. Therefore, if a dynamical phase transition occurs nearby $s = 0$, it is related to coexistence of phases of different activity, $k(s) \approx \sum_j \mathrm{Tr}[J_j^\dagger J_j\,\rho_{\mathrm{ss}}(s)]$, and thus

typical trajectories (at $s = 0$) exhibit a sharp intermittence due to dynamical phases $\rho_{\rm ss}(s)$ from either side of the transition differing in activity [3, 39, 40, 82].

Biased sampling for metastable phases. As argued in the precious section 5.2.4, the intermittence in quantum trajectories does not necessarily require non-analyticities in eigenvalues of $\mathcal{L}_s$ resulting in the thermodynamic limit, but can instead occur due to the metastability present in the dynamics, see also [4]. This analogy goes even further and, as we prove in Ref. [93], in such a case, biasing quantum trajectories according to the jump activity which distinguishes the metastable phases, allows for the metastable phases to be obtained as the stationary state, $\rho_{\rm ss}(s)$, of the biased dynamics, $\mathcal{L}_s$. The proof follows closely the argument for the classical dynamics in [50], and relies on the almost degenerate non-hermitian perturbation theory, where $\delta\mathcal{L}_s(\rho) = (e^{-s} - 1)\sum_j J_j \rho\, J_j^\dagger$ is considered as a perturbation of the master operator $\mathcal{L}$, cf. Eq. (5.32). Briefly, by choosing the bias value s so that the perturbation is larger than the contribution of slow modes, i.e. $\mathcal{L}_{\rm MM}$ in Eq. (5.15), but nevertheless much smaller than the separation to the fast modes, the effective dynamics of metastable phases can be neglected. In this case the perturbation to the steady state of the biased dynamics, $\rho_{\rm ss}(s)$, simply corresponds to the metastable phase with the highest or the lowest activity, for negative and positive s, respectively. Furthermore, the rate function and its derivative can be approximated by

$$\theta(s) = \left(e^{-s} - 1\right) \max_{1\le k\le m} \sum_j \mathrm{Tr}\left(J_j^\dagger J_j\, \tilde{\rho}_k\right), \tag{5.34}$$

$$k(s) = e^{-s} \max_{1\le k\le m} \sum_j \mathrm{Tr}\left(J_j^\dagger J_j\, \tilde{\rho}_k\right), \tag{5.35}$$

for negative s, while for positive s the maximum is replaced by the minimum. We note that the smoothness of $\theta(s)$ is still guaranteed by non-negligible contribution from $\mathcal{L}_{\rm MM}$ at the intermediate values of s.

This result is clearly confirmed in Fig. 5.9(a) where at the negative bias (i.e. towards larger activity) two sharp transitions are found close to $s = 0$. The corresponding activity equals zero, one or twice the value which can be identified as total single spin activity proportional to $\Omega^2/\kappa + 2\gamma + ...$, see Eq. (5.21), and changes as the perturbation due to the bias becomes larger than λ_m for $m = 7$ and $m = 10$, which correspond, respectively, to the smaller MM with only single excitations beyond the dark state, and the larger MM with also double excitations being metastable. This is further supported by Fig. 5.9(b), where in the decomposition between metastable phases, the stationary state of the biased dynamics at $s = 0$ corresponds mostly to the dark metastable phase,

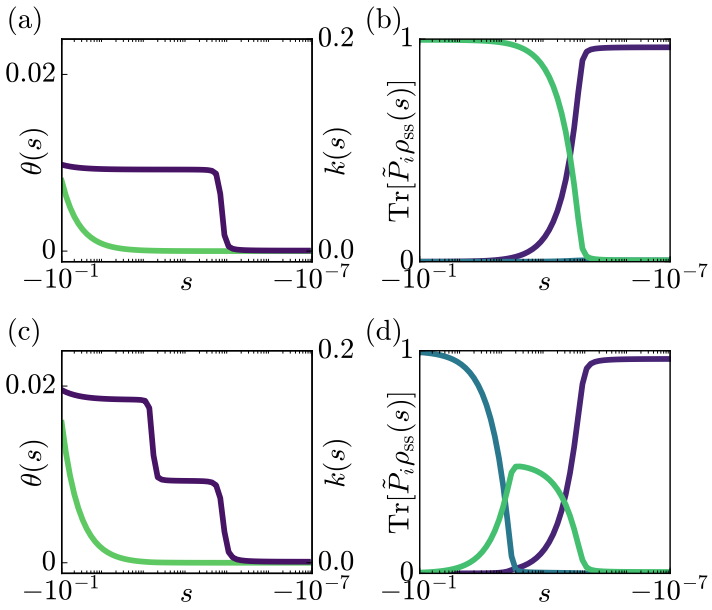


Figure 5.10: Detailed biased sampling for unfolding classical metastable manifolds: (a,c) The leading eigenvalue (rate function) $\theta(s)$ of the biased master operator, (5.36), for the quantum East model, and the corresponding activity $k(s)$, plotted on a log scale as a function of bias for all jumps on a single site (a), $s_1 = s$, or two sites (c), $s_1 = s_4 = s$. (b,d) The projection of the stationary state of the biased dynamics onto the metastable manifold at $s = 0$: the dark phase (dark), the phase with a single excitation on the third or sixth site (light) and the phase with two excitations on the third and sixth site (intermediate). In (a-d) $\Omega/\kappa = 0.15$, $\gamma/\kappa = 0.0004$ and $p = 0.999$, while $\theta(s)$ and $\rho_{\mathrm{ss}}(s)$ were obtained by numerical diagonalisation of $\mathcal{L}_{\mathbf{s}}$.

while for a large enough negative bias can be characterised as the equal mixture of six single-excitation metastable phases or the equal mixture of three double-excitation metastable phases (here homogeneity follows from the translation symmetry of $\mathcal{L}_s$). Interestingly, for larger values of the bias s [insets in Fig. 5.9] another sharp transition is observed, when the corresponding stationary state is found outside the metastable manifold. This sharp transition corresponds directly to the effective metastability observed already in Fig. 5.8(f,g), and is a consequence of the fact that the average activity in any system state is a linear function of the average S_z spin magnetisation, and therefore it perturbs only some of the eigenmodes with an effective gap in the set of their eigenvalues.

The bias with respect to total activity leads to the translationally symmetric operator $\mathcal{L}_s$, (5.32), and thus its stationary state is homogeneous, and it cannot distinguish the individual single- and two-excitation metastable phases.

Dynamics can be biased instead with respect to activity of individual jumps, which leads to the master operator

$$\mathcal{L}_{\mathbf{s}}(\rho) = -i[H,\rho] + \sum_j \left[e^{-s_j} J_j \rho J_j^\dagger - \frac{1}{2}\{J_j^\dagger J_j, \rho\} \right], \tag{5.36}$$

where the $(\mathbf{s})_j = s_j$ are the values of individual biases. In particular, for local dissipation, as in the dissipative quantum East model, cf. Eq. (5.24), $\mathcal{L}_{\mathbf{s}}$ no longer features translation symmetry, and thus it can allow for distinguishing metastable phases differing spatially in the activity profile. This is demonstrated in Fig. 5.10, where the bias is tuned away from 0 for one or two sites (first and fourth, $s_1, s_4 \neq 0$). In the case of a single site being biased (a,b), the stationary state of the dynamics with a large enough negative bias becomes the corresponding metastable phase with a single excitation located to the left of the biased site, so that the excitation can satisfy the hard constraint and facilitate the activity on the site. In the case of the activity biased equally on two sites (c,d), the stationary state first becomes an equal mixture of two metastable phases with a single excitation (due to the translation symmetry of $\mathcal{L}_{\mathbf{s}}$ by 3 sites), while for a large enough negative bias it corresponds exactly to the metastable phase with two excitation next to the two sites being biased.

In Figs. 5.9 and 5.10, in order to demonstrate that biasing the dynamics can be used to distinguish metastable phases, we have used the exact diagonalisation of the biased master operators in Eqs. (5.32) and (5.36). It is known, however, that biasing of the classical stochastic dynamics can be efficiently applied directly to the generation of stochastic trajectories, with techniques such as transition path sampling [7] and cloning [8]. If such techniques can generalised to the quantum case via quantum jump Monte Carlo sampling, following the discussion above, we conclude that they could be used to distinguish metastable phases differing in activity, without the need of diagonalising the master operators in Eq. (2.25) or Eq. (5.32).

Time-coarse-graining of quantum trajectories and effective stochastic dynamics. Finally, we note that the proof in Ref. [93] connecting the steady state of the biased dynamics with metastable phases, provides a complementary argument to the discussion in Sec. 5.2.4 of the connection between time-coarse grained quantum trajectories and classical stochastic dynamics between the metastable phases. Above we have argued that post-selecting trajectories towards more (less) activity leads to the time-averaged state in the trajectories given exactly by the metastable phase with an excitation (no excitation) to the

left of the biased site. Moreover, it also follows that for the intermediate bias values, the biased steady state corresponds to the mixture of metastable phases exactly the same as in the case of biasing the effective classical dynamics inside the metastable manifold with their average activity, i.e. magnetisation. In other words, the corresponding rate functions coincide in the neighbourhood of $s = 0$ (with size given by the gap in the master operator spectrum), which implies that the main contributions to the first two cumulants of the full jump statistics, i.e, the average and variance, are well captured by the effective classical dynamics between metastable phases [104], see Ref. [93] for the proof.

5.4 Summary

We have described a general set of techniques for achieving a complete understanding of classical metastability emerging from open quantum systems.

First, we described an approach based on the low-lying eigenmodes of the dynamics, which provides the structure of the manifold of metastable states relevant at long times, together with the effective dynamics within the manifold. This was successfully applied to a quantum generalization of the classical East model, commonly found in the study of glass physics, allowing us to show that the metastable manifold was classical, and given by a hierarchy of states characterized by the number of excited sites, similar to the classical East model. Further, the long time effective dynamics of the model was shown not only to be classical, but also to possess detailed balance, with the free energy depending only on the number of excitations, not their distance: both properties also found in the classical East model.

This approach requires diagonalization of the master operator describing the dynamics, a difficult task in some models of interest; we discussed an alternative to this technique based on the concept of biased trajectory sampling. While biased sampling of quantum trajectories is difficult to achieve at present, we demonstrated this method in principle, again using the dissipative quantum East model: we found that appropriately biased ensembles of trajectories return, to a good approximation, the metastable phases of the unbiased dynamics. However, for this to allow for the study of systems with larger state spaces, the development of efficient trajectory sampling for open quantum systems will be required.

While these techniques allow to uncover the long time properties of open

quantum systems exhibiting classical metastability, it is currently unknown how to approach the systems exhibiting quantum metastability, e.g. with metastable coherences [2], which will be addressed in future research. Such methods, among others, will also inform the study of structure at first-order phase transitions in open quantum systems.

Chapter 6

Spectral properties of classical and quantum reset processes

The dynamics of stochastic processes, such as animals foraging for food in the wilderness or a person searching for car keys, often include random resets in time, taking the form of returns to past locations where food was successfully located or the last place a person remembers seeing their keys [105]. Recently, there has been a renewed interest in these processes, due to the fact that they can improve the efficiency of certain random search processes and algorithms in terms of mean hitting or first-passage time [106–111]. Reset processes have also been studied from a more physical point of view, as they provide a simple model of nonequilibrium processes breaking detailed balance [112–115], as well as of processes showing dynamical phase transitions in their relaxation dynamics [116], mean first-passage time [117], or large deviations [118–120].

These studies follow many previous works in mathematics, in queuing theory and in population dynamics, in particular, on stochastic processes involving some form of random resets, variously referred to as failures, catastrophes, disasters or decimations; see, e.g., [121–129]. Most of these works, as well as those from physics mentioned above, make use of the correspondence that exists between resets and renewals to obtain renewal representations of both time-dependent and stationary distributions, in addition to first-passage statistics. Modified Fokker–Planck and Feynman–Kac equations with additional source and sink terms describing the evolution of these distributions and statistics have also been obtained (see, e.g., [107, 118, 128]) and can be solved explicitly for some simple models, including reset versions of Brownian motion [106] and the Ornstein-Uhlenbeck process [130].

In this chapter, we present a different approach to reset processes based on the spectral properties of their generator or master operator. Our main result is a relation between the spectrum of the generator of a reset process and that of its reset-free counterpart. More precisely, we show that the real part of the eigenvalues of the generator are shifted for all non-stationary modes by the reset rate, while the corresponding eigenstates, representing the dynamical modes, are not modified. We also provide explicit expressions for the stationary state and current of reset processes involving weighted sums over the dynamical modes, which are applied to two prototypical models, namely, the totally asymmetric random walk in one dimension, related to queuing, and the one-dimensional Brownian motion. The results obtained clearly explain how resets can accelerate or even induce relaxation to a stationary state by opening a spectral gap, and how non-zero stationary currents can be created without having complex eigenvalues in the spectrum of the generator. These results can also be combined with the spectral theory of classical metastability [1,14,16], or quantum metastability discussed in earlier chapters, to demonstrate that weak resetting can modify the weighting of metastable states without modifying those states significantly.

While resets have been extensively considered in classical nonequilibrium physics, a relatively unexplored area is the addition of resets to quantum systems, either closed or interacting with an environment. This case has been considered recently for a quantum walker subjected to continuous measurements on a particular site, resulting in a random collapse of the wavefunction followed by an evolution starting from the measured site [131, 132]. We conclude our study by generalising our spectral results to the type of open quantum systems described in general by the Lindblad master equation, providing a natural link with the recent extension of the spectral theory of metastability to quantum systems [2]. We illustrate this generalization by computing numerically the stationary state of a model of coherent hopping in one dimension realizing the reset quantum random walker, and by applying our method to the dissipative transverse field Ising model [3], previously considered in Chap. 4, providing a demonstration of the effects of resets on metastability [4].

6.1 Classical reset Markov processes

We first consider the classical jump processes introduced in Sec. 2.1. The reset version of that process is constructed simply by adding new transitions at a rate Γ from every configuration to a target or reset state, denoted by C_0. The generator of the reset process is thus given by

$$\mathcal{L}^{\Gamma} = \mathcal{L} + \Gamma \sum_{C \neq C_0} |C_0\rangle \langle C| - \Gamma \sum_{C \neq C_0} |C\rangle \langle C| , \tag{6.1}$$

where the additional terms can be absorbed into the old jump operators and escape rate operator to give shifted transition and escape rates. Note that we can add

$$0 = \Gamma |C_0\rangle \langle C_0| - \Gamma |C_0\rangle \langle C_0| \tag{6.2}$$

to $\mathcal{L}^{\Gamma}$ to obtain the simpler form

$$\begin{aligned} \mathcal{L}^{\Gamma} &= \mathcal{L} + \Gamma \sum_{C} |C_0\rangle \langle C| - \Gamma \sum_{C} |C\rangle \langle C| \\ &= \mathcal{L} + \Gamma |C_0\rangle \langle -| - \Gamma I, \end{aligned} \tag{6.3}$$

where I is the identity operator. In this form, it is clear that the reset adds transitions from all states to C_0, contributing to an extra escape rate Γ in the diagonal, which keeps the conservation condition $\langle -| \mathcal{L}^{\Gamma} = 0$.

The dynamics generated by (6.3) is arguably the simplest form of reset process. As defined, reset events are Poissonian with rate Γ, which is independent of the state of the system at the time of the reset.

We study in this section the spectral properties of the reset process, deriving the new eigenvalues, left eigenvectors and right eigenvectors of $\mathcal{L}^{\Gamma}$ in terms of those of $\mathcal{L}$. The results are then used to obtain spectral representations of the stationary state and current of the reset process, and to discuss the effect of resets on metastable states.

6.1.1 Eigenvalues and eigenvectors

Recalling the spectral theory of Sec. 2.1.1, we begin our analysis with the right eigenvectors by noting that, due to conservation of probability and the fact that $\langle -|r_i\rangle = 0$ for all $i \neq 1$, we have

$$\begin{aligned} \mathcal{L}^{\Gamma} |r_i\rangle &= \big(\mathcal{L} + \Gamma |C_0\rangle \langle -| - \Gamma I\big) |r_i\rangle \\ &= (\lambda_i - \Gamma) |r_i\rangle \end{aligned} \tag{6.4}$$

for $i \neq 1$. Consequently, the right eigenvectors of the reset process are the same as those of the original process, while the eigenvalues are shifted down by Γ:

$$\lambda_i^\Gamma = \lambda_i - \Gamma, \qquad i \neq 1. \tag{6.5}$$

This applies, as noted, to all modes except the stationary state, discussed below, which is still such that $\lambda_1^\Gamma = 0$.

To determine the left eigenvectors, we act from the left with the original eigenmodes

$$\begin{aligned}\langle l_i| \mathcal{L}^\Gamma &= \langle l_i| \left(\mathcal{L} + \Gamma |C_0\rangle \langle -| - \Gamma I\right) \\ &= (\lambda_i - \Gamma) \langle l_i| + \Gamma \langle l_i|C_0\rangle \langle -| \\ &= (\lambda_i - \Gamma) \left(\langle l_i| + \frac{\Gamma \langle l_i|C_0\rangle}{\lambda_i - \Gamma} \langle -|\right).\end{aligned}$$

But by conservation of probability $\langle -| \mathcal{L}^\Gamma = 0$, we also have

$$\langle l_i| \mathcal{L}^\Gamma = \left(\langle l_i| + \frac{\Gamma \langle l_i|C_0\rangle}{\lambda_i - \Gamma} \langle -|\right) \mathcal{L}^\Gamma \tag{6.6}$$

for all $i \neq 1$. Thus we see that the new left eigenvectors are given by

$$\langle l_i^\Gamma| = \langle l_i| + \frac{\Gamma \langle l_i|C_0\rangle}{\lambda_i - \Gamma} \langle -|, \qquad i \neq 1. \tag{6.7}$$

For $i = 1$, we have as before $\langle l_1^\Gamma| = \langle -|$.

6.1.2 Stationary state

The stationary state $|P_{\text{ss}}^\Gamma\rangle$ of the reset process, corresponding to $|r_1^\Gamma\rangle$, is obtained from the results above by noting that the new left and right eigenvectors are orthonormal to each other, so that $\langle l_i^\Gamma | P_{\text{ss}}^\Gamma\rangle = \delta_{i1}$. Substituting this condition in Eq. (6.7), we find

$$\langle l_i | P_{\text{ss}}^\Gamma\rangle = -\frac{\Gamma \langle l_i|C_0\rangle}{\lambda_i - \Gamma}, \tag{6.8}$$

for $i \neq 1$, and thus

$$|P_{\text{ss}}^\Gamma\rangle = |P_{\text{ss}}\rangle - \sum_{i=2}^{D} \frac{\Gamma \langle l_i|C_0\rangle}{\lambda_i - \Gamma} |r_i\rangle. \tag{6.9}$$

We see that in addition to the stationary state of the process without resets, the resetting stationary state contains a contribution of the dynamical modes, weighted according to how significant they are in the evolution of the reset state in the original dynamics (the overlaps $\langle l_i|C_0\rangle$), and the reset rates magnitude

relative to the corresponding eigenvalue λ_i. This agrees with intuition: since the eigenvalues are related to the lifetimes of the dynamical modes, if the average time between resets is larger than the lifetime of a mode, it will not make a significant contribution to the new steady state. We note that this equation also has the expected limits of $|P^0_{\rm ss}\rangle = |P_{\rm ss}\rangle$ and $|P^\infty_{\rm ss}\rangle = |C_0\rangle$.

This result applies for processes with a finite number D of states, but also to infinite-dimensional processes, provided that they possess a well-defined spectrum of eigenvalues with corresponding left and right eigenmodes. This latter fact will be illustrated in the next section with the example of Brownian motion.

We should also note that the result holds if the reset state $|C_0\rangle$ is replaced by a reset probability distribution $|P_0\rangle$ over configurations, giving the probability of reaching different states after a reset event. In this case, $|C_0\rangle$ in Eq. (6.9) is simply replaced by the "mixed" reset state $|P_0\rangle$. This follows since the reset state is never referred to above as anything more than as a vector in state space.

Finally we mention the modification resulting from a lack of ergodicity, i.e., when $\mathcal{L}\,|r_i\rangle = 0$ and $\langle l_i|\,\mathcal{L} = 0$ for more than one pair of states, causing an initial state dependence of the stationary state. Generically, we can still choose a basis such that $\langle l_1| = \langle -|$ and $\langle l_i|r_j\rangle = \delta_{ij}$ within this null eigenspace, allowing us to use nearly the same proof scheme as above. The reset rates break the zero eigenvalue's degeneracy and induces a unique stationary state, with the remainder of the null eigenspace shifted to an eigenvalue of $-\Gamma$. In Eq. (6.9) the unique steady state $|P_{\rm ss}\rangle$ is replaced by the state-dependent steady state that would be reached from the reset state under the original dynamics.

6.1.3 Stationary current

The current associated with the stationary state $|P^\Gamma_{\rm ss}\rangle$ of the reset process is defined, for any given link or transition $c \to c'$, by

$$J^\Gamma_{c\to c'} = \left\langle c|P^\Gamma_{\rm ss}\right\rangle \mathcal{L}^\Gamma_{c'c} - \left\langle c'|P^\Gamma_{\rm ss}\right\rangle \mathcal{L}^\Gamma_{cc'}, \tag{6.10}$$

where $\mathcal{L}^\Gamma_{ij}$ is the (i,j) component of $\mathcal{L}^\Gamma$. Substituting the expression of the stationary state, found in Eq. (6.9), together with the expression of the generator

$\mathcal{L}^\Gamma$, we can decompose the current into three parts as

$$J^\Gamma_{c\to c'} = J_{c\to c'} + \sum_{i=2}^{D} \frac{\Gamma \langle l_i|C_0\rangle}{\Gamma - \lambda_i} J^i_{c\to c'} + \Gamma\left(\left\langle c|P^\Gamma_{\rm ss}\right\rangle \delta_{c'c_0} - \left\langle c'|P^\Gamma_{\rm ss}\right\rangle \delta_{c_0 c}\right), \tag{6.11}$$

where

$$J^i_{c\to c'} = \langle c|r_i\rangle \mathcal{L}_{c'c} - \langle c'|r_i\rangle \mathcal{L}_{cc'}. \tag{6.12}$$

The first term on the right-hand side of Eq. (6.11) is the current of the original reset-free process, while the second is the weighted contribution of new currents coming from the non-stationary modes of the original process. Finally, the third term is the current coming from the reset transitions. From the signs appearing in the last term, we see that there is a current loop from all the states to the reset state C_0 and then back from C_0 to all other states, so that C_0 acts both as a sink and source.

From this result, it is clear that the reset process will violate the condition of detailed balance, i.e., $J^\Gamma \neq 0$, if the original process satisfies the condition of detailed balance, i.e., $J = 0$. In this case, it is known that the original process has a real spectrum, which implies from our results that the spectrum of the reset process must also be real, even though $J^\Gamma \neq 0$. This shows that currents are not necessarily associated with complex spectra of the dynamical generator. In fact, detailed balance is only a sufficient condition for the generator spectrum to be real, not a necessary condition.

In principle, it is also possible to have a reset process satisfying detailed balance ($J^\Gamma = 0$) if the original process violates detailed balance ($J \neq 0$). However, this is a rather peculiar case, requiring that the added reset transitions with rate Γ exactly counterbalance all the non-zero currents arising in the reset-free process. In this case, the original process must again have a real spectrum in order for the spectrum of the reset process to be real.

6.1.4 Metastability

We close this section by discussing the effect of resets on metastable states that arise when the evolution of the probability distribution $P(C,t)$ exhibits two distinct time scales: a fast evolution towards long-lived metastable states, followed by a slow relaxation to the final stationary state, as discussed extensively in Sec. 2.1.3.

We focus for simplicity on the one-dimensional metastable manifold case. First, we note that we can rewrite Eq. (6.9) as

$$|P_{\rm ss}^{\Gamma}\rangle = |P_{\rm ss}\rangle - \sum_{i=2}^{D} \frac{\langle l_i|C_0\rangle}{\frac{\lambda_i}{\Gamma} - 1} |r_i\rangle \,. \tag{6.13}$$

As a result, we see that, if we consider $\Gamma \approx |\lambda_2| \ll |\lambda_3|$, then the coefficients in the sum for the terms $i \geq 3$ are small compared to the coefficient for $i = 2$, so we can truncate to only the first two terms:

$$|P_{\rm ss}^{\Gamma}\rangle \approx |P_{\rm ss}\rangle - \frac{\Gamma \langle l_2|C_0\rangle}{\lambda_2 - \Gamma} |r_2\rangle \,. \tag{6.14}$$

Since the spectrum of the process with resets is simply a real shift by Γ, values on this scale preserve the gap in the spectrum required for metastability, as for $\Gamma \approx |\lambda_2|$ we still have $\mathrm{Re}(\lambda_2) - \Gamma \ll \mathrm{Re}(\lambda_3) - \Gamma$. Physically, this regime corresponds to the average time between resets being comparable to the lifetime of the metastable phases, in which the short timescale dynamical modes represented by $i \geq 3$ are averaged out and make negligible contribution to the stationary state.

Using the definitions (2.18) of the eMSs with the modified left eigenmodes from Sec. 6.1.1, the eMSs of the model with resets are given by

$$\begin{aligned} |\tilde{P}_1^{\Gamma}\rangle &= |P_{\rm ss}^{\Gamma}\rangle + c_2^{\Gamma,\max} |r_2\rangle \\ |\tilde{P}_2^{\Gamma}\rangle &= |P_{\rm ss}^{\Gamma}\rangle + c_2^{\Gamma,\min} |r_2\rangle \,, \end{aligned} \tag{6.15}$$

where, since the modification to the left eigenmodes is simply a shift by the flat state, the coefficients are now given by

$$c_2^{\Gamma,\min/\max} = c_2^{\min/\max} - \frac{\Gamma \langle l_2|C_0\rangle}{\Gamma - \lambda_2}. \tag{6.16}$$

Substituting this and Eq. (6.14) into Eq. (6.15), we see that the eMSs with reset are approximately equal to the original eMSs, as the effect of the modifications to the steady state and left eigenmodes cancel. Applying Eq. (2.19) to the model with reset and using $|\tilde{P}_i^{\Gamma}\rangle \approx |\tilde{P}_i\rangle$, we thus obtain

$$\begin{aligned} |P_{\rm ss}^{\Gamma}\rangle &\approx (p_1^{\rm ss} + \Delta p) |\tilde{P}_1\rangle + (p_2^{\rm ss} - \Delta p) |\tilde{P}_2\rangle \\ &= |P_{ss}\rangle + \Delta p |\tilde{P}_1\rangle - \Delta p |\tilde{P}_2\rangle \,, \end{aligned}$$

where

$$\Delta p = \frac{\Gamma \langle l_2|C_0\rangle}{\Delta c_2(\Gamma - \lambda_2)}. \tag{6.17}$$

We see that, depending on the overlap of the reset state with $|l_2\rangle$, this coefficient can cause a notable modification of the steady state mixture even for small Γ. This means physically that resets will make whichever eMS is closer to the reset state more likely to occur in the stationary state, as expected. Finally, the modified effective dynamics can be constructed simply by replacing the coefficients and eigenvalues with the new ones in Eq. (2.20).

6.2 Classical applications

We apply in this section our formula (6.9) for the stationary state of the reset process for two exactly-solvable models. The applicability of this formula is obviously limited by the fact that it requires the full spectrum of the reset-free process. For this reason, we expect it to be more useful for approximating the stationary state than for calculating that state exactly, either by truncating the sum involved to a limited number of modes or by expanding the sum perturbatively in Γ. Moreover, while exact results can be hard to find, the formula can be useful numerically when applied to processes in which the resets break symmetries of the original, reset-free process. Such symmetries can indeed be used to diagonalise the original process for system sizes much larger than would otherwise be possible, with the resulting spectrum then being used in (6.9) to derive the stationary state with resets. This is demonstrated later in the context of adding resets to a closed quantum system, breaking time-reversal symmetry.

6.2.1 Totally asymmetric random walk

The first model that we consider is a particle hopping on a one-dimensional lattice of length L with periodic boundary conditions, so the states are $|x\rangle$ with $x \in \{1, 2, \ldots, L\}$ and $|L+1\rangle = |1\rangle$. We take the particle to hop only to the right with rate γ, so that the master operator is

$$\mathcal{L} = \gamma \sum_{x=1}^{L} |x+1\rangle \langle x| - \gamma I. \tag{6.18}$$

This operator is translation invariant and can be diagonalized by discrete Fourier transform, with left and right eigenvectors given by

$$|r_n\rangle = \frac{1}{L} \sum_{x=1}^{L} e^{i\frac{2\pi n}{L}(x-1)} |x\rangle \tag{6.19}$$

and

$$\langle l_n| = \sum_{x=1}^{L} e^{-i\frac{2\pi n}{L}(x-1)} \langle x|, \tag{6.20}$$

respectively, where $n \in \{0, ..., L-1\}$. As before, these eigenvectors are normalized such that $\langle l_n|r_m\rangle = \delta_{nm}$. Moreover, the eigenvalues are given by

$$\lambda_n = \gamma(e^{-i2\pi n/L} - 1). \tag{6.21}$$

We now add resets at rate Γ onto the reset site $|1\rangle$. The new eigenvalues and eigenvectors can then be calculated exactly using the results of the previous section, with Eq. (6.9) leading to

$$\left\langle x|P_{\rm ss}^{\Gamma}\right\rangle = \frac{\Gamma}{\gamma+\Gamma} S_L(x), \tag{6.22}$$

where

$$S_L(x) = \frac{1}{L}\sum_{n=0}^{L-1} \frac{e^{i\frac{2\pi n}{L}x}}{e^{i\frac{2\pi n}{L}} - \frac{\gamma}{\gamma+\Gamma}}. \tag{6.23}$$

Considering the sum $S_L(x)$ on different sites, we find

$$S_L(x+1) - \frac{\gamma}{\gamma+\Gamma} S_L(x) = \delta_{xL}, \tag{6.24}$$

and so $S_L(x+1) = \gamma/(\gamma+\Gamma)S_L(x)$ when $x \neq L$. Consequently,

$$\left\langle x|P_{\rm ss}^{\Gamma}\right\rangle = \frac{\Gamma}{\gamma}\left(\frac{\gamma}{\gamma+\Gamma}\right)^x S_L(1). \tag{6.25}$$

At this point, rather than explicitly calculate the sum $S_L(1)$, we can just normalise the stationary state to find

$$S_L(1) = \frac{1}{1-\left(\frac{\gamma}{\gamma+\Gamma}\right)^L}, \tag{6.26}$$

thus giving

$$P_{\rm ss}^{\Gamma}(x) = \left\langle x|P_{\rm ss}^{\Gamma}\right\rangle = \frac{\Gamma}{\gamma+\Gamma}\frac{1}{1-\left(\frac{\gamma}{\gamma+\Gamma}\right)^L}\left(\frac{\gamma}{\gamma+\Gamma}\right)^{x-1}. \tag{6.27}$$

This result is interesting because, while the infinite-size limit of the initial model neither has a stationary state or the ability to reach one (the spectral gap tends to zero), the infinite-size limit of the model with resets gains a gap of exactly Γ, with the corresponding stationary state given by the limit of Eq. (6.27), with probabilities

$$P_{\rm ss}^{\Gamma}(x) = \frac{\Gamma}{\gamma+\Gamma}\left(\frac{\gamma}{\gamma+\Gamma}\right)^{x-1}, \tag{6.28}$$

where normalization can be checked via the geometric series. In this way, we see that resets localise the particle near the reset state, with a localisation length of

$$\epsilon = \frac{1}{\ln\left(\frac{\gamma+\Gamma}{\gamma}\right)}. \tag{6.29}$$

6.2.2 Brownian motion

We now show how to apply our results to continuous-state models by seeing them as the limit of a sequence of finite-dimensional models which have a discrete spectrum and well-defined eigenvectors. We consider for this purpose the reset Brownian motion in one dimension, first studied in [106] via a modified Fokker-Planck equation.

The master, or Fokker-Planck operator in this case, without reset is the Laplacian

$$\mathcal{L}p(x) = D\frac{d^2p(x)}{dx^2} \tag{6.30}$$

on the real line, with D as the diffusion constant and $p(x)$ the probability density. The spectrum of this operator is trivial, but it has no normalised stationary state, nor is it possible to define the orthogonality relation between left and right eigenfunctions. To address this problem, we restrict the system, as commonly done in physics, to the finite interval $[-L/2, L/2)$ with periodic boundary conditions. The spectrum of this restricted model is simply given by

$$\lambda_n = -D\left(\frac{2\pi n}{L}\right)^2, \qquad n \in \mathbb{Z}, \tag{6.31}$$

with equal right and left eigenmodes, due to the Hermiticity of $\mathcal{L}$, given by

$$r_n(x) = \frac{1}{\sqrt{L}}e^{i\frac{2\pi n}{L}x}, \tag{6.32}$$

and normalised according to

$$\langle r_n|r_m\rangle = \int_{-L/2}^{L/2} r_n^*(x)r_m(x)\,dx = \delta_{nm}. \tag{6.33}$$

Since the spectrum exists and can be normalized appropriately, we may use our results of Sec. 6.1. Adding resets at a rate Γ to the position 0, and defining the states $|0\rangle$ and $\langle -|$ by $\langle g|0\rangle = g(0)$ and

$$\langle -|f\rangle = \langle l_0|f\rangle = \int_{-L/2}^{L/2} f(x)\,dx, \tag{6.34}$$

respectively, we find the new stationary state, which is now a probability density, to be given by the sum

$$p_{\mathrm{ss}}^{\Gamma}(x) = \frac{\Gamma}{L} \sum_{n=-\infty}^{\infty} \frac{e^{i\frac{2\pi n}{L}x}}{D\left(\frac{2\pi n}{L}\right)^2 + \Gamma}. \tag{6.35}$$

Taking the infinite-size limit, we then find

$$p_{\mathrm{ss}}^{\Gamma}(x) = \Gamma \int_{-\infty}^{\infty} \frac{dk}{2\pi} \frac{e^{ikx}}{Dk^2 + \Gamma}, \tag{6.36}$$

which can be solved using residues to give

$$p_{\mathrm{ss}}^{\Gamma}(x) = \frac{1}{2}\sqrt{\frac{\Gamma}{D}} e^{-\sqrt{\frac{\Gamma}{D}}|x|}. \tag{6.37}$$

This agrees with the result of [106] and is similar to the distribution (6.28) found for the discrete random walk.

6.3 Open quantum systems with resets

We next consider adding resets to open quantum systems interacting with an environment, as introduced in Sec. 2.2.

For the classical stochastic processes discussed in the previous sections, reset occurred with equal probability from every state at times distributed exponentially with rate Γ. We can construct a similar kind of reset dynamics for quantum open systems by adding jump operators

$$J_i^{\Gamma} = \sqrt{\Gamma}\, |\psi\rangle \langle \phi_i| \tag{6.38}$$

to the Lindbladian (2.25). Here $|\phi_i\rangle$ form a complete orthonormal basis, i.e., $\langle \phi_i | \phi_j \rangle = \delta_{ij}$, and $|\psi\rangle$ is the reset state. This modifies the Lindblad generator to

$$\mathcal{L}_{\Gamma}(\rho) = \mathcal{L}(\rho) + \mathcal{V}_{\Gamma}(\rho) - \Gamma\rho, \tag{6.39}$$

where

$$\mathcal{V}_{\Gamma}(\rho) = \Gamma \operatorname{Tr}(\rho) |\psi\rangle \langle \psi| . \tag{6.40}$$

To check that this construction has state-independent resets, as desired, we can consider the quantum jump Monte Carlo (QJMC) approach to simulating individual trajectories of the system's evolution (see, e.g., [23]). When the system undergoes a stochastic dissipative change (a "jump"), the probability of the change being a reset is

$$P_{\Gamma}(|\phi\rangle) \propto \sum_{k}^{\dim(\mathcal{H})} \langle \phi | J_k^{\Gamma\dagger} J_k^{\Gamma} |\phi\rangle = \Gamma \langle \phi | \phi \rangle , \tag{6.41}$$

and is thus state independent as required.

To analyse the spectrum of the model with resets, we make the same assumptions as in Sec. 6.1: we assume that the stationary state of the model without resets is unique, and that it is diagonalizable (i.e., there are no non-trivial Jordan blocks). The uniqueness of the stationary state implies $\mathrm{Tr}(R_i) = 0$ and hence

$$\mathcal{L}_\Gamma(R_i) = (\lambda_i - \Gamma)R_i \tag{6.42}$$

for $i \in \{2, ..., \dim(\mathcal{H}^2)\}$. This shows, similarly to the classical case, that the R_i's remain eigenmodes of the model with resets, with modified eigenvalues

$$\lambda_i^\Gamma = \lambda_i - \Gamma. \tag{6.43}$$

For $i = 1$, we have again $\lambda_1 = 0$ and the stationary state $R_1 = \rho_{\mathrm{ss}}$, which we calculate below using an analogous method to that of Sec. 6.1.1.

Next, we consider the corresponding left eigenmodes dual to the above. The adjoint equation is given by

$$\mathcal{L}_\Gamma^\dagger(\rho) = \mathcal{L}^\dagger(\rho) + \mathcal{V}_\Gamma^\dagger(\rho) - \Gamma\rho, \tag{6.44}$$

where $\mathcal{V}_\Gamma^\dagger(\rho) = \Gamma \langle\psi| \rho |\psi\rangle I$. Note that the identity I remains an eigenmode with eigenvalue 0, as expected. Inserting the original left eigenmodes, we find

$$\mathcal{L}_\Gamma^\dagger(L_k) = (\lambda_k^* - \Gamma)L_k + \Gamma \langle\psi| L_k |\psi\rangle I. \tag{6.45}$$

Defining

$$L_k^\Gamma = L_k + \frac{\Gamma \langle\psi| L_k |\psi\rangle}{\lambda_k^* - \Gamma} I, \tag{6.46}$$

we see that, since the identity is annihilated by the adjoint operator, we have

$$\mathcal{L}_\Gamma^\dagger \left(L_k^\Gamma\right) = (\lambda_k^* - \Gamma)L_k^\Gamma, \tag{6.47}$$

demonstrating that the new left eigenmodes are L_k^Γ. It can be checked that $\mathrm{Tr}(L_i^{\Gamma\dagger} R_j) = \delta_{ij}$ for $j \neq 1$ and for all i, as expected, since $\mathrm{Tr}(R_j) = 0$. Finally, requiring $\mathrm{Tr}(L_i^{\Gamma\dagger} \rho_{ss}^\Gamma) = \delta_{i1}$ for the new stationary state ρ_{ss}^Γ gives the expansion coefficients of that state in the original right eigenmode basis as

$$\rho_{ss}^\Gamma = \rho_{ss}^0 - \sum_{j=2}^{\dim(\mathcal{H})^2} \frac{\Gamma \langle\psi| L_j^\dagger |\psi\rangle}{\lambda_j - \Gamma} R_j, \tag{6.48}$$

which, as can be checked, gives $\mathcal{L}_\Gamma \rho_{ss}^\Gamma = 0$.

The practical applicability of these results depends, as in the classical case, on the system studied and whether, in particular, it has symmetries simplifying

the spectral problem. There is an additional benefit in the case of closed quantum systems coming from the fact that the Lindblad equation reduces in that case to the von Neumann equation, allowing for much larger system sizes to be studied compared to a direct spectral solution of the open quantum problem. We demonstrate this next.

6.3.1 Coherent hopping on a chain

The first example that we consider to illustrate our results is a simple model of coherent hopping on a closed periodic chain, described by the Hamiltonian

$$\begin{aligned} H =& \gamma \sum_{x=1}^{L-1} \left(|x+1\rangle \langle x| + |x\rangle \langle x+1| \right) \\ &+ \gamma \left(|1\rangle \langle L| + |L\rangle \langle 1| \right), \end{aligned} \tag{6.49}$$

and no jump operators, so that the reset-free system is closed. The dynamics generated by this Hamiltonian is similar to that considered in [131, 132]. The main difference is that we consider state-independent resets whereas [131, 132] consider resets induced by continuously measuring the system's state on a particular site, leading to a single jump operator proportional to the projective measurement on that site.

For closed quantum systems, the spectrum of the corresponding Lindblad equation is given by all possible outer products of the eigenvectors and corresponding differences of eigenvalues of H. Given

$$H |e_k\rangle = \lambda_k |e_k\rangle , \tag{6.50}$$

the matrices $R_{kk'} = |e_k\rangle \langle e_{k'}|$ then provide the right eigenmodes of the Lindblad equation

$$\mathcal{L}(R_{kk'}) = -i(\lambda_k - \lambda_{k'}) R_{kk'}, \tag{6.51}$$

with the corresponding left eigenmodes also given by $L_{kk'} = |e_k\rangle \langle e_{k'}|$. In this context, our results at the start of Sec. 6.3 can be modified to handle degenerate modes with $\mathcal{L}(R_i) = 0$, as is the case for closed quantum systems, analogously to the procedure described at the end of Sec. 6.1.2. The resulting modification to Eq. (6.48) for coherent dynamics contains a sum over the non-zero eigenvalue modes as before, with the unique stationary density matrix replaced by a diagonal matrix in the energy eigenbasis of probabilities for the reset state to be measured in each eigenstate of the Hamiltonian.

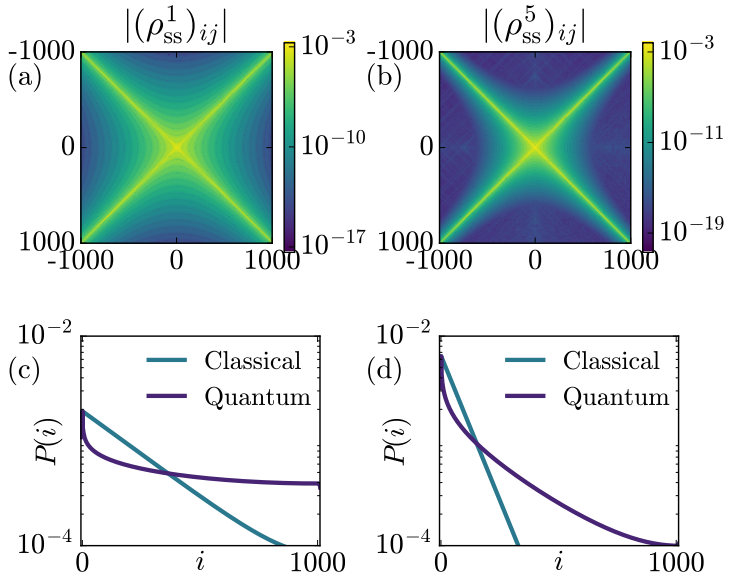


Figure 6.1: (a,b) Magnitude of the stationary density matrix on a log scale. (c,d) Occupation probability for each site of the chain compared with the probability of a classical hopping model with exponential distribution. Plots are for (a,c) $\Gamma = 1$ and (b,d) $\Gamma = 5$.

Using the outer product structure of the eigenstates, we can rewrite this sum more compactly as the matrix product

$$\rho^{\Gamma}_{ss} = E\Lambda^{\Gamma}E^{\dagger}, \tag{6.52}$$

where E is the matrix of eigenvectors defined by $HE = E\Lambda$ with $\Lambda_{ii} = \lambda_i$, and Λ^{Γ} has elements defined by

$$\Lambda^{\Gamma}_{ij} = \frac{\Gamma \langle\psi|e_j\rangle \langle e_i|\psi\rangle}{\Gamma + i(\lambda_i - \lambda_j)}. \tag{6.53}$$

These matrices can be efficiently constructed numerically and used to calculate the stationary state of a closed system after the addition of resets.

For the coherent hopping model we have

$$|e_n\rangle = \frac{1}{\sqrt{L}} \sum_{x=1}^{L} e^{i\frac{2\pi n}{L}(x-1)} |x\rangle , \tag{6.54}$$

and $\lambda_k = 2\Omega\cos(2\pi n/L)$. Choosing resets to the state $|0\rangle$ for a chain of $L = 2001$ and hopping rate $\gamma = 1000 \gg \Gamma$, the numerically calculated stationary state is given for two different reset rates in Fig. 6.1. As expected, the magnitude of the components of the stationary state decay away from the reset state (Fig. 6.1(a,b)). In Fig. 6.1(c,d), we plot the probability for the system to be

found in each site against the distance from the reset state. For comparison, we also plot the probability for a classical random walk with resets, with parameters fixed by equating the probability of the two distributions at the reset state. We see that the coherent dynamics allows particles to move away from the reset state at a faster rate than the dissipative dynamics, leading to a crossing point beyond which there is a higher probability of locating the particle in the coherent model compared to the dissipative model.

6.3.2 Open quantum Ising model

Here we return to the dissipative Ising model considered in Chap. 4, defined by equations (4.9) and (4.10). Unlike the models previously considered, this system is not exactly solvable without resets; however, it possesses a translation symmetry, which can be used with Eq. (6.48) to numerically diagonalise the model for larger system sizes than if we simply tried to diagonalize the symmetry-lacking Lindblad equation with resets.

As we have seen in Chap. 4, this system exhibits a collective metastability in a region of the parameter space. This metastability takes the form of a decomposition of the system's state after a long evolution into a linear combination of a paramagnetic phase and ferromagnetic phase on either side of the crossover. This is followed by an eventual relaxation to a particular mixture of these two phases. We thus use this model to study the effect of adding resets to a model with metastability explicitly, comparing the quantum generalization of the results from Sec. 6.1.4 with the stationary states given by Eq. (6.48).

We start by studying the reset rate dependence of the system's magnetisation in the z direction: recall,

$$M = \frac{1}{N}\sum_{i=1}^{N} S_z^i. \tag{6.55}$$

Considering a system of $N = 7$ spins, in Fig. 6.2(a) we plot the magnetisation of both the full reset stationary state given by Eq. (6.48) (solid lines) and the approximate decomposition of the reset stationary state into the original metastable phases given by Eq. (6.17) (dashed lines). This is done for two different reset states, $|\psi_1\rangle = |\uparrow\uparrow\uparrow\uparrow\uparrow\uparrow\uparrow\rangle$ and $|\psi_2\rangle = |\uparrow\downarrow\uparrow\downarrow\uparrow\downarrow\uparrow\rangle$, both of which have a high probability of evolving into the paramagnetic state after a time in the metastable regime.

Without resets the stationary state is dominated by the ferromagnetic phase. However, for both reset states, there is a larger probability of evolving into the

paramagnetic phase than the ferromagnetic phase on metastable timescales. When the reset rate is increased, we expect the stationary state to become more biased towards the paramagnetic phase. This is clearly demonstrated in Fig. 6.2(a), with strong agreement between the exact result and the approximation for reset rates up to the order of $|\lambda_2|$. For Γ beyond this scale, metastability is lost and the approximation fails, with the magnetisation approaching that of the reset states for large Γ.

To quantify the agreement, we show in Fig. 6.2(b) the trace distance between the truncated metastable state, as given by Eq. (6.17), and the full reset stationary state, as given by Eq. (6.48). We can see that this distance is close to zero up until $\Gamma = |\lambda_2|$, after which it increases rapidly, demonstrating a strong accuracy of Eq. (6.17) when the average time between resets is equal to or longer than the metastable timescale, as assumed in Sec. 6.1.4. This change in the stationary magnetisation for smaller reset rates corresponds directly to the changing mixture of metastable phases in the stationary state. This is seen in Fig. 6.2(c), which shows a higher probability of the system being found in the paramagnetic phase as Γ is increased. The same behavior can also be seen at the trajectory level in the two plots of Fig. 6.2(d,e), which show sample trajectories without resets and with resets to the state $|\uparrow\uparrow\uparrow\uparrow\uparrow\uparrow\uparrow\rangle$ at a rate Γ, respectively. As expected, we see that resets induce more periods of paramagnetic phase dropping back into the ferromagnetic phase.

We note that it may be possible to conduct an experiment to study the effect of resets on this Ising model (and similar many-body spin models) using ultra-cold atoms confined in optical latices [44,53,133,134]. In such experiments, the $|\downarrow\rangle$-state is associated with the atomic ground state, while the $|\uparrow\rangle$-state is represented by a Rydberg nS-state. These states are coupled coherently by laser, leading to Rabi oscillations at a frequency Ω and a detuning Δ relative to the energy difference between the two states. Excited atoms at lattice sites with position r_i and r_j interact via a van der Waals potential $V_{ij} = C_6/|r_i - r_j|^6$, where C_6 is the dispersion coefficient characterizing the interaction strength. Altogether this gives a Hamiltonian of the form

$$H = \Omega \sum_i S_x^i + \Delta \sum_i S_z^i + \frac{1}{2} \sum_{i \neq j} V_{ij} n_i n_j, \tag{6.56}$$

where $n_i = 1/2I + S_z^i$. For sufficiently large lattice spacing a, the interaction decays so rapidly that it can be approximated as a nearest-neighbour interaction. Applying a laser detuning of the form $\Delta = -C_6/a^6$ then leads for a periodic

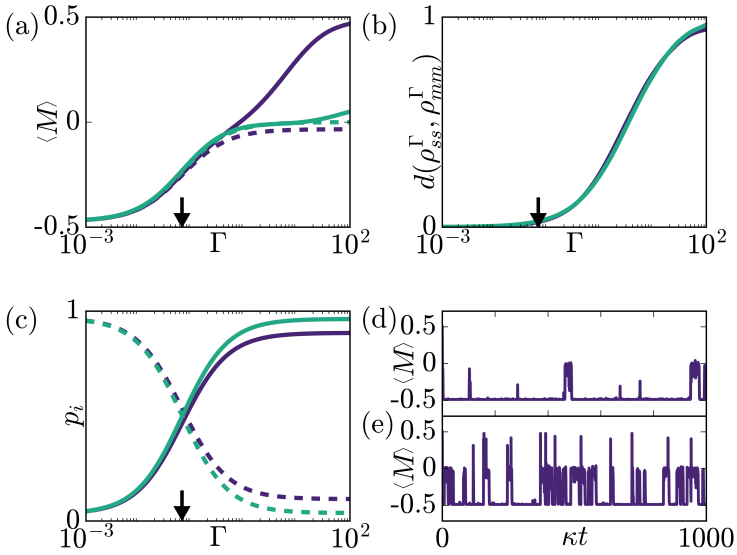


Figure 6.2: (a) Magnetisation in the z direction of the stationary state (solid) compared with the metastable approximation (dashed) as a function of the reset rate Γ. (b) Probability of the two extreme metastable states as a function of Γ. (c) Trace distance between the stationary state and the metastable approximation as a function of Γ. (d-e) Sample trajectories of the magnetisation over time for $\Gamma = 0$ (d) and $\Gamma = 0.05$ (e). Purple lines are for resets to the "all up" state ψ_1, while blue lines are for resets to the "alternating" state ψ_2. Arrows indicate the point where $\Gamma = |\lambda_2|$.

chain to the Ising Hamiltonian (4.9), up to an overall energy shift that can be discarded. Dissipation occurs naturally via photon-emitted decay of the Rydberg states.

To simulate resets in this system, we can force it into a high magnetisation state at random intervals determined externally from an exponential distribution. While it is difficult in practice to place the system in a specific pure state with high magnetisation reliably, the above results simply generalize to a probability distribution of pure reset states (i.e., a reset "density matrix"). If such a density matrix has a large positive expectation value for the magnetisation, evolution after reset will have a high probability of leading to the paramagnetic state on the metastable timescale, resulting in similar observations to those of Fig. 6.2. These resets could be implemented via a strong laser pulse, such that the system can be momentarily approximated as non-interacting and the pulse modelled as instantaneous.

6.4 Summary

We have developed in this work a general spectral approach to investigate the properties of Markov processes that are reset to a fixed state at random exponentially distributed times. Our main result shows that the spectrum of the generator of a reset Markov process is globally shifted by the reset rate compared with the spectrum of the corresponding reset-free process, except for the stationary mode, which stays at zero. We have also provided an explicit formula for the stationary distribution of the reset process, based on the spectrum of the reset-free process.

This spectral approach can be applied not only to classical stochastic processes but also, as we have shown, to closed and open quantum systems modelled by Lindblad-type equations. In both cases, the approach provides a natural way to study how resets can create a stationary state by opening a gap in the spectrum and how it affects metastable states. This was illustrated using various classical and quantum processes, including reset Brownian motion and the transverse field Ising model reset to a paramagnetic or ferromagnetic state.

For future work, it would be interesting to develop a similar approach for the large deviations of reset processes, based on the spectrum of the tilted generator [118, 119]. There does not seem to be, a priori, a direct extension of our results for this generator, as the basic property used to prove our results, namely, that the non-stationary eigenstates have zero norm, does not hold in general for the eigenstates of the tilted generator. However, it might be possible to obtain partial results when the addition of reset to the master operator mixes only a small subset of the non-reset spectrum.

There also remains much work to be done on quantum systems, for which resets can be induced either by measurements, as in [131, 132], or through other external perturbations. Some results on these systems have also been obtained very recently in [135] for the stationary state of closed quantum systems with reset, which form, as we have seen, a specific case of the quantum systems considered here.

Chapter 7

Conclusion

We have seen how metastability in open quantum systems can arise in a variety of situations: from proximity to a suspected phase transition, as in the Ising model of Chap. 4; to the constrained dynamics typical of glassy systems, such as the quantum East model in Chap. 5. In the process, we made substantial use of symmetries as discussed in Chap. 3, and we developed an extensive numerical approach to complex classical metastability in Chap. 5. We further saw how randomly occurring resets could bias a system towards a particular metastable phase in Chap. 6, amongst several other general results about the spectral properties of classical and quantum systems with resets.

There remain many avenues of research to be explored following this work. In the more general realm of reset processes, very little is known about the effect of resets on quantum systems, with only a handful of cases having been considered [131, 132, 135]; similarly, it remains to be seen whether there exist general spectral results when resetting for the modified master operators which describe a systems large deviations. The discovery of efficient trajectory sampling techniques for the study of large deviations in open quantum systems remains an open problem, with a lack of detailed balance and the computational time required per trajectory rendering current approaches time consuming. Such sampling would allow for an alternative approach to constructing classical metastable phases and the dynamics between them as discussed in Sec. 5.3, however a general understanding of quantum metastable manifolds is yet to be achieved, either through spectral techniques or sampling. An alternative to large deviation based sampling could be the use of Markov state modelling, a technique in which low-dimensional effective models are constructed from an underlying classical stochastic dynamics: this would require a two-fold

extension of these techniques, first to produce effective classical models from an underlying open quantum dynamics, and secondly to produce effective quantum dynamics. We hope to address many of the above questions in future work.

Bibliography

[1] B. Gaveau and L. S. Schulman. Dynamical metastability. *J. Phys. A*, 20(10):2865–2873, 1987.

[2] K. Macieszczak, M. Guta, I. Lesanovsky, and J. P. Garrahan. Towards a Theory of Metastability in Open Quantum Dynamics. *Phys. Rev. Lett.*, 116:240404, 2016.

[3] C. Ates, B. Olmos, J. P. Garrahan, and I. Lesanovsky. Dynamical phases and intermittency of the dissipative quantum Ising model. *Phys. Rev. A*, 85(4):043620, 2012.

[4] Dominic C. Rose, Katarzyna Macieszczak, Igor Lesanovsky, and Juan P. Garrahan. Metastability in an open quantum Ising model. *Phys. Rev. E*, 94:052132, 2016.

[5] B. Olmos, I. Lesanovsky, and J. P. Garrahan. Facilitated Spin Models of Dissipative Quantum Glasses. *Phys. Rev. Lett.*, 109:020403, 2012.

[6] H. Touchette. The large deviation approach to statistical mechanics. *Phys. Rep.*, 478(1):1–69, 2009.

[7] L. O. Hedges, R. L. Jack, J. P. Garrahan, and D. Chandler. Dynamic Order-Disorder in Atomistic Models of Structural Glass Formers. *Science*, 323(5919):1309–1313, 2009.

[8] C. Giardina, J. Kurchan, V. Lecomte, and J. Tailleur. Simulating Rare Events in Dynamical Processes. *J. Stat. Phys.*, 145(4):787–811, 2011.

[9] Crispin Gardiner. *Stochastic Methods: A Handbook for the Natural and Social Sciences*. Springer Series in Synergetics. Springer-Verlag Berlin Heidelberg, 2009.

[10] Juan P. Garrahan. Classical stochastic dynamics and continuous matrix product states: gauge transformations, conditioned and driven processes, and equivalence of trajectory ensembles. *J. Stat. Mech.*, 2016(7):073208, 2016.

[11] S. A. Gershgorin. Über die Abgrenzung der Eigenwerte einer Matrix. *Bull. Acad. Sci. URSS*, 1931(6):749–754, 1931.

[12] Oskar Perron. Zur theorie der matrices. *Mathematische Annalen*, 64(2):248–263, Jun 1907.

[13] P. M. Chaikin and T. C. Lubensky. *Principles of condensed matter physics*, volume 1. Cambridge Univ Press, 2000.

[14] B. Gaveau and L. S. Schulman. Theory of nonequilibrium first-order phase transitions for stochastic dynamics. *J. Mat. Phys.*, 39(3):1517, 1998.

[15] A. Bovier, M. Eckhoff, V. Gayrard, and M. Klein. Metastability and Low Lying Spectra in Reversible Markov Chains. *Commun. Math. Phys.*, 228:219, 2002.

[16] B. Gaveau and L. S. Schulman. Multiple phases in stochastic dynamics: Geometry and probabilities. *Phys. Rev. E*, 73(3):036124, 2006.

[17] H. Larralde and F. Leyvraz. Metastability for Markov Processes with Detailed Balance. *Phys. Rev. Lett.*, 94:160201, 2005.

[18] Enzo Olivieri and Maria Eulália Vares. *Large Deviations and Metastability*. Encyclopedia of Mathematics and its Applications. Cambridge University Press, 2005.

[19] C. W. Gardiner and P. Zoller. *Quantum Noise*. Complexity. Springer, third edition edition, 2004.

[20] Heinz-Peter Breuer and Francesco Petruccione. *The Theory of Open Quantum Systems*. Oxford University Press, 2007.

[21] G. Lindblad. On the generators of quantum dynamical semigroups. *Commun. Math. Phys.*, 48(2):119–130, 1976.

[22] Vittorio Gorini, Andrzej Kossakowski, and E. C. G. Sudarshan. Completely positive dynamical semigroups of n-level systems. *Journal of Mathematical Physics*, 17(5):821–825, 1976.

[23] M. B. Plenio and P. L. Knight. The quantum-jump approach to dissipative dynamics in quantum optics. *Rev. Mod. Phys.*, 70:101–144, 1998.

[24] Andrew J. Daley. Quantum trajectories and open many-body quantum systems. *Adv. Phys.*, 63(2):77–149, 2014.

[25] B. Buča and T. Prosen. A note on symmetry reductions of the Lindblad equation: transport in constrained open spin chains. *New J. Phys.*, 14(7):073007, 2012.

[26] V. V. Albert and L. Jiang. Symmetries and conserved quantities in Lindblad master equations. *Phys. Rev. A*, 89:022118, 2014.

[27] Katarzyna Macieszczak and Dominic C. Rose. Weak unitary symmetries of the Lindblad equations simplify quantum trajectories. *In preparation*, 2019.

[28] J. D. Pritchard, D. Maxwell, A. Gauguet, K. J. Weatherill, M. P. A. Jones, and C. S. Adams. Cooperative Atom-Light Interaction in a Blockaded Rydberg Ensemble. *Phys. Rev. Lett.*, 105:193603, 2010.

[29] R. Blatt and C. F. Roos. Quantum simulations with trapped ions. *Nat. Phys.*, 8(4):277–284, 2012.

[30] J. W. Britton, B. C. Sawyer, A. C. Keith, C.-C. J. Wang, J. K. Freericks, H. Uys, M. J. Biercuk, and J. J. Bollinger. Engineered two-dimensional Ising interactions in a trapped-ion quantum simulator with hundreds of spins. *Nature*, 484(7395):489–492, 2012.

[31] Y. O. Dudin and A. Kuzmich. Strongly Interacting Rydberg Excitations of a Cold Atomic Gas. *Science*, 336(6083):887–889, 2012.

[32] T. Peyronel, O. Firstenberg, Q. Liang, S. Hofferberth, A. V. Gorshkov, T. Pohl, M. D. Lukin, and V. Vuletic. Quantum nonlinear optics with single photons enabled by strongly interacting atoms. *Nature*, 488(7409):57–60, 2012.

[33] G. Günter, H. Schempp, M. Robert-de Saint-Vincent, V. Gavryusev, S. Helmrich, C. S. Hofmann, S. Whitlock, and M. Weidemüller. Observing the Dynamics of Dipole-Mediated Energy Transport by Interaction-Enhanced Imaging. *Science*, 342(6161):954–956, 2013.

[34] S. Schmidt and J. Koch. Circuit QED lattices: Towards quantum simulation with superconducting circuits. *Ann. Phys.*, 525(6):395–412, 2013.

[35] E. G. D. Torre, S. Diehl, M. D. Lukin, S. Sachdev, and P. Strack. Keldysh approach for nonequilibrium phase transitions in quantum optics: Beyond the Dicke model in optical cavities. *Phys. Rev. A*, 87:023831, 2013.

[36] L. M. Sieberer, M. Buchhold, and S. Diehl. Keldysh field theory for driven open quantum systems. *Rep. Prog. Phys.*, 79(9):096001, 2016.

[37] M. F. Maghrebi and A. V. Gorshkov. Nonequilibrium many-body steady states via Keldysh formalism. *Phys. Rev. B*, 93:014307, 2016.

[38] A. A. Gangat, I. T, and Y.-J. Kao. Steady States of Infinite-Size Dissipative Quantum Chains via Imaginary Time Evolution. *Phys. Rev. Lett.*, 119(1), 2017.

[39] J. P. Garrahan and I. Lesanovsky. Thermodynamics of Quantum Jump Trajectories. *Phys. Rev. Lett.*, 104:160601, 2010.

[40] I. Lesanovsky, M. van Horssen, M. Guţă, and J. P. Garrahan. Characterization of Dynamical Phase Transitions in Quantum Jump Trajectories Beyond the Properties of the Stationary State. *Phys. Rev. Lett.*, 110:150401, 2013.

[41] M. Esposito, U. Harbola, and S. Mukamel. Nonequilibrium fluctuations, fluctuation theorems, and counting statistics in quantum systems. *Rev. Mod. Phys.*, 81(4):1665, 2009.

[42] K. Binder and W. Kob. *Glassy Materials and Disordered Solids: An Introduction to Their Statistical Mechanics (Revised Edition)*. World Scientific, 2011.

[43] G. Biroli and J. P. Garrahan. Perspective: The glass transition. *J. Chem. Phys.*, 138(12):12A301, 2013.

[44] Tony E. Lee, H. Häffner, and M. C. Cross. Collective Quantum Jumps of Rydberg Atoms. *Phys. Rev. Lett.*, 108:023602, 2012.

[45] O. Viehmann, J. von Delft, and F. Marquardt. Observing the Nonequilibrium Dynamics of the Quantum Transverse-Field Ising Chain in Circuit QED. *Phys. Rev. Lett.*, 110:030601, 2013.

[46] H. Weimer. Variational Principle for Steady States of Dissipative Quantum Many-Body Systems. *Phys. Rev. Lett.*, 114:040402, 2015.

[47] H. Weimer. Variational analysis of driven-dissipative Rydberg gases. *Phys. Rev. A*, 91:063401, 2015.

[48] V. R. Overbeck, M. F. Maghrebi, A. V. Gorshkov, and H. Weimer. Multicritical behavior in dissipative Ising models. *Phys. Rev. A*, 95(4), 2017.

[49] M. Marcuzzi, M. Buchhold, S. Diehl, and I. Lesanovsky. Absorbing State Phase Transition with Competing Quantum and Classical Fluctuations. *Phys. Rev. Lett.*, 116:245701, 2016.

[50] J. Kurchan. Six out of equilibrium lectures. *arXiv:0901.1271*, 2016.

[51] J. Thingna, D. Manzano, and J. Cao. Dynamical signatures of molecular symmetries in nonequilibrium quantum transport. *Sci. Rep.*, 6:28027, 2016.

[52] B. Sciolla, D. Poletti, and C. Kollath. Two-Time Correlations Probing the Dynamics of Dissipative Many-Body Quantum Systems: Aging and Fast Relaxation. *Phys. Rev. Lett.*, 114:170401, 2015.

[53] Markus Müller, Linmei Liang, Igor Lesanovsky, and Peter Zoller. Trapped Rydberg ions: from spin chains to fast quantum gates. *New J. Phys.*, 10(9):093009, 2008.

[54] S. G. Schirmer and X. Wang. Stabilizing open quantum systems by Markovian reservoir engineering. *Phys. Rev. A*, 81:062306, 2010.

[55] M. Marcuzzi, E. Levi, S. Diehl, J. P. Garrahan, and I. Lesanovsky. Universal Nonequilibrium Properties of Dissipative Rydberg Gases. *Phys. Rev. Lett.*, 113:210401, 2014.

[56] M. Guta. Fisher information and asymptotic normality in system identification for quantum Markov chains. *Phys. Rev. A*, 83:062324, 2011.

[57] C. Catana, L. Bouten, and M. Guta. Fisher informations and local asymptotic normality for continuous-time quantum Markov processes. *J. Phys. A*, 48(36):365301, 2015.

[58] A. Karabanov, D. C. Rose, W. Köckenberger, J. P. Garrahan, and I. Lesanovsky. Phase Transitions in Electron Spin Resonance Under Continuous Microwave Driving. *Phys. Rev. Lett.*, 119:150402, 2017.

[59] G. Lancaster. Electron paramagnetic resonance (a review). *Journal of Materials Science*, 2(5):489–495, 1967.

[60] A. Schweiger and G. Jeschke. *Principles of Pulse Electron Paramagnetic Resonance*. Oxford University Press, 2001.

[61] R. G. Griffin and T. F. Prisner. High field dynamic nuclear polarization—the renaissance. *Phys. Chem. Chem. Phys.*, 12:5737–5740, 2010.

[62] A. Vadim Atsarkin and Walter Köckenberger. The Different Magnetic Resonance Communities Join Forces for Progress in DNP: an Editorial for the Special Issue on DNP. *Applied Magnetic Resonance*, 43(1-2):1–2, 2012.

[63] W. T. Wenckebach. *Essentials of Dynamic Nuclear Polarization*. Spindrift Publications, 2016.

[64] Chester F. Hwang and Daniel A. Hill. Phenomenological Model for the New Effect in Dynamic Polarization. *Phys. Rev. Lett.*, 19:1011–1014, 1967.

[65] Kan-Nian Hu, Hsiao-hua Yu, Timothy M. Swager, and Robert G. Griffin. Dynamic Nuclear Polarization with Biradicals. *Journal of the American Chemical Society*, 126(35):10844–10845, 2004. PMID: 15339160.

[66] M. Borghini. Spin-Temperature Model of Nuclear Dynamic Polarization Using Free Radicals. *Phys. Rev. Lett.*, 20:419–421, 1968.

[67] A. Abragam and M. Goldman. *Nuclear magnetism: order and disorder*. International series of monographs on physics. Clarendon Press, 1982.

[68] Alexander Karabanov, Grzegorz Kwiatkowski, Carlo U. Perotto, Daniel Wiśniewski, Jonathan McMaster, Igor Lesanovsky, and Walter Köckenberger. Dynamic nuclear polarisation by thermal mixing: quantum theory and macroscopic simulations. *Phys. Chem. Chem. Phys.*, 18:30093–30104, 2016.

[69] M. Foss-Feig, P. Niroula, J. T. Young, M. Hafezi, A. V. Gorshkov, R. M. Wilson, and M. F. Maghrebi. Emergent equilibrium in many-body optical bistability. *Phys. Rev. A*, 95:043826, 2017.

[70] V. A. Atsarkin. Dynamic polarization of nuclei in solid dielectrics. *Phys.-Usp*, 21(9):725–745, 1978.

[71] Sami Jannin, Arnaud Comment, and J. J. van der Klink. Dynamic Nuclear Polarization by Thermal Mixing Under Partial Saturation. *Applied Magnetic Resonance*, 43(1-2):59–68, 2012.

[72] Yonatan Hovav, Akiva Feintuch, and Shimon Vega. Theoretical aspects of dynamic nuclear polarization in the solid state – spin temperature and thermal mixing. *Phys. Chem. Chem. Phys.*, 15:188–203, 2013.

[73] Sonia Colombo Serra, Alberto Rosso, and Fabio Tedoldi. Electron and nuclear spin dynamics in the thermal mixing model of dynamic nuclear polarization. *Phys. Chem. Chem. Phys.*, 14:13299–13308, 2012.

[74] Andrea De Luca and Alberto Rosso. Dynamic Nuclear Polarization and the Paradox of Quantum Thermalization. *Phys. Rev. Lett.*, 115:080401, 2015.

[75] J. J. Mendoza-Arenas, S. R. Clark, S. Felicetti, G. Romero, E. Solano, D. G. Angelakis, and D. Jaksch. Beyond mean-field bistability in driven-dissipative lattices: Bunching-antibunching transition and quantum simulation. *Phys. Rev. A*, 93:023821, 2016.

[76] W. Casteels and M. Wouters. Optically bistable driven-dissipative Bose-Hubbard dimer: Gutzwiller approaches and entanglement. *Phys. Rev. A*, 95:043833, 2017.

[77] F. Letscher, O. Thomas, T. Niederprüm, M. Fleischhauer, and H. Ott. Bistability Versus Metastability in Driven Dissipative Rydberg Gases. *Phys. Rev. X*, 7:021020, 2017.

[78] N. R. de Melo, C. G. Wade, N. Šibalić, J. M. Kondo, C. S. Adams, and K. J. Weatherill. Intrinsic optical bistability in a strongly driven Rydberg ensemble. *Phys. Rev. A*, 93:063863, 2016.

[79] S. R. K. Rodriguez, W. Casteels, F. Storme, N. Carlon Zambon, I. Sagnes, L. Le Gratiet, E. Galopin, A. Lemaître, A. Amo, C. Ciuti, and J. Bloch. Probing a Dissipative Phase Transition via Dynamical Optical Hysteresis. *Phys. Rev. Lett.*, 118:247402, 2017.

[80] B. Gaveau, A. Lesne, and L. S. Schulman. Spectral signatures of hierarchical relaxation. *Phys. Lett. A*, 258(4):222–228, 1999.

[81] B. Olmos, I. Lesanovsky, and J. P. Garrahan. Out-of-equilibrium evolution of kinetically constrained many-body quantum systems under purely dissipative dynamics. *Phys. Rev. E*, 90:042147, 2014.

[82] J. P. Garrahan, A. D. Armour, and I. Lesanovsky. Quantum trajectory phase transitions in the micromaser. *Phys. Rev. E*, 84:021115, 2011.

[83] Federico Carollo, Juan P. Garrahan, Igor Lesanovsky, and Carlos Pérez-Espigares. Making rare events typical in Markovian open quantum systems. *Phys. Rev. A*, 98:010103, 2018.

[84] J. Jäckle and S. Eisinger. A hierarchically constrained kinetic Ising model. *Z. Phys. B*, 84(1):115–124, 1991.

[85] P. Sollich and M. R. Evans. Glassy Time-Scale Divergence and Anomalous Coarsening in a Kinetically Constrained Spin Chain. *Phys. Rev. Lett.*, 83:3238–3241, 1999.

[86] J. P. Garrahan and D. Chandler. Geometrical Explanation and Scaling of Dynamical Heterogeneities in Glass Forming Systems. *Phys. Rev. Lett.*, 89:035704, 2002.

[87] P. Sollich and M. R. Evans. Glassy dynamics in the asymmetrically constrained kinetic Ising chain. *Phys. Rev. E*, 68:031504, 2003.

[88] D. S. Rokhsar and S. A. Kivelson. Superconductivity and the Quantum Hard-Core Dimer Gas. *Phys. Rev. Lett.*, 61:2376–2379, 1988.

[89] C. L. Henley. From classical to quantum dynamics at Rokhsar–Kivelson points. *J. Phys. Cond. Mat.*, 16(11), 2004.

[90] M. van Horssen, E. Levi, and J. P. Garrahan. Dynamics of many-body localization in a translation-invariant quantum glass model. *Phys. Rev. B*, 92:100305, 2015.

[91] J. M. Hickey, S. Genway, and J. P. Garrahan. Signatures of many-body localisation in a system without disorder and the relation to a glass transition. *J. Stat. Mech.*, 2016(5):054047, 2016.

[92] Zhihao Lan, Merlijn van Horssen, Stephen Powell, and Juan P. Garrahan. Quantum Slow Relaxation and Metastability due to Dynamical Constraints. *Phys. Rev. Lett.*, 121:040603, 2018.

[93] Dominic C. Rose, Katarzyna Macieszczak, Igor Lesanovsky, and Juan P. Garrahan. Classical metastability in open quantum systems. *In preparation*, 2019.

[94] Bernhard Baumgartner and Heide Narnhofer. Analysis of quantum semigroups with GKS–Lindblad generators: II. General. *J. Phys. A*, 41(39):395303, 2008.

[95] Paolo Zanardi. Dissipative dynamics in a quantum register. *Phys. Rev. A*, 56:4445–4451, 1997.

[96] P. Zanardi and M. Rasetti. Noiseless Quantum Codes. *Phys. Rev. Lett.*, 79(17):3306–3309, 1997.

[97] D. A. Lidar, I. L. Chuang, and K. B. Whaley. Decoherence-Free Subspaces for Quantum Computation. *Phys. Rev. Lett.*, 81(12):2594–2597, 1998.

[98] Emanuel Knill, Raymond Laflamme, and Lorenza Viola. Theory of Quantum Error Correction for General Noise. *Phys. Rev. Lett.*, 84(11):2525–2528, 2000.

[99] Paolo Zanardi. Stabilizing quantum information. *Phys. Rev. A*, 63:012301, 2000.

[100] Xiaoting Wang, Mark Byrd, and Kurt Jacobs. Numerical method for finding decoherence-free subspaces and its applications. *Phys. Rev. A*, 87:012338, 2013.

[101] Da-Jian Zhang, Xiao-Dong Yu, Hua-Lin Huang, and D. M. Tong. General approach to find steady-state manifolds in Markovian and non-Markovian systems. *Phys. Rev. A*, 94:052132, 2016.

[102] C. Ingemar Bengtsson and Karol Życzkowski. *Geometry of Quantum States: An Introduction to Quantum Entanglement*. Cambridge University Press, 2006.

[103] Tosio Kato. *Perturbation Theory for Linear Operators*. Springer, 1995.

[104] K. Macieszczak, M. Guta, I. Lesanovsky, and J. P. Garrahan. Dynamical phase transitions as a resource for quantum enhanced metrology. *Phys. Rev. A*, 93:022103, 2016.

[105] O. Bénichou, C. Loverdo, M. Moreau, and R. Voituriez. Intermittent search strategies. *Rev. Mod. Phys.*, 83:81–129, 2011.

[106] Martin R. Evans and Satya N. Majumdar. Diffusion with stochastic resetting. *Phys. Rev. Lett.*, 106(16):1–4, 2011.

[107] Martin R. Evans and Satya N. Majumdar. Diffusion with optimal resetting. *J. Phys. A*, 44(43):435001, 2011.

[108] M. R. Evans, S. N. Majumdar, and K. Mallick. Optimal diffusive search: Nonequilibrium resetting versus equilibrium dynamics. *J. Phys. A*, 46(18):185001, 2013.

[109] M. R. Evans and S. N. Majumdar. Diffusion with resetting in arbitrary spatial dimension. *J. Phys. A*, 47(28):285001, 2014.

[110] S. Reuveni. Optimal stochastic restart renders fluctuations in first passage times universal. *Phys. Rev. Lett.*, 116:170601, 2016.

[111] Arnab Pal and Shlomi Reuveni. First Passage under Restart. *Phys. Rev. Lett.*, 118(3):030603, 2017.

[112] Susanna C. Manrubia and Damián H. Zanette. Stochastic multiplicative processes with reset events. *Phys. Rev. E*, 59(5):4945–4948, 1999.

[113] S. Gupta, S. N. Majumdar, and G. Schehr. Fluctuating Interfaces Subject to Stochastic Resetting. *Phys. Rev. Lett.*, 112:220601, 2014.

[114] E. Roldán, A. Lisica, D. Sánchez-Taltavull, and S. W. Grill. Stochastic resetting in backtrack recovery by RNA polymerases. *Phys. Rev. E*, 93:062411, 2016.

[115] S. Eule and J. J. Metzger. Non-equilibrium steady states of stochastic processes with intermittent resetting. *New J. Phys.*, 18(3):033006, 2016.

[116] S. N. Majumdar, S. Sabhapandit, and G. Schehr. Random walk with random resetting to the maximum position. *Phys. Rev. E*, 92:052126, 2015.

[117] Lukasz Kusmierz, Satya N. Majumdar, Sanjib Sabhapandit, and Grégory Schehr. First order transition for the optimal search time of lévy flights with resetting. *Phys. Rev. Lett.*, 113(22):1–5, 2014.

[118] Janusz M. Meylahn, Sanjib Sabhapandit, and Hugo Touchette. Large deviations for Markov processes with resetting. *Phys. Rev. E*, 92(6):062148, 2015.

[119] Rosemary J. Harris and Hugo Touchette. Phase transitions in large deviations of reset processes. *J. Phys. A*, 50(10), 2017.

[120] F. den Hollander, S. N. Majumdar, J. M. Meylahn, and H. Touchette. Properties of additive functionals of Brownian motion with resetting. *arXiv:1801.09909*, 2018.

[121] P. J. Brockwell, J. Gani, and S. I. Resnick. Birth, Immigration and Catastrophe Processes. *Adv. in Appl. Prob.*, 14(4):709–731, 1982.

[122] M. Luby, A. Sinclair, and D. Zuckerman. Optimal speedup of Las Vegas algorithms. *Info. Proc. Lett.*, 47(4):173–180, 1993.

[123] A. G. Pakes. Killing and resurrection of Markov processes. *Comm. Stat. Stoch. Models*, 13(2):255–269, 1997.

[124] B. K. Kumar and D. Arivudainambi. Transient solution of an M/M/1 queue with catastrophes. *Comp. & Math. with Appl.*, 40(10–11):1233–1240, 2000.

[125] B. Cairns and P. K. Pollett. Extinction times for a general birth, death and catastrophe process. *J. Appl. Prob.*, 41:1211–1218, 2004.

[126] S. Janson and Y. Peres. Hitting Times for Random Walks with Restarts. *SIAM J. Discrete Math.*, 26(2):537–547, 2012.

[127] Konstantin Avrachenkov, Alexey Piunovskiy, and Yi Zhang. Markov Processes with Restart. *J. Appl. Prob.*, 50(4):960–968, 2013.

[128] Selvamuthu Dharmaraja, Antonio Di Crescenzo, Virginia Giorno, and Amelia G. Nobile. A Continuous-Time Ehrenfest Model with Catastrophes and Its Jump-Diffusion Approximation. *J. Stat. Phys.*, 161(2):326–345, 2015.

[129] Miquel Montero, Axel Masó-Puigdellosas, and Javier Villarroel. Continuous-time random walks with reset events: Historical background and new perspectives. *Eur. Phys. J. B*, 90(9):176, 2017.

[130] Arnab Pal. Diffusion in a potential landscape with stochastic resetting. *Phys. Rev. E*, 91(1):012113, 2015.

[131] Felix Thiel, Eli Barkai, and David A. Kessler. First Detected Arrival of a Quantum Walker on an Infinite Line. *Phys. Rev. Lett.*, 120:040502, 2018.

[132] H. Friedman, D. A. Kessler, and E. Barkai. Quantum renewal equation for the first detection time of a quantum walk. *J. Phys. A*, 50(4), 2017.

[133] M. Saffman, T. G. Walker, and K. Mølmer. Quantum information with Rydberg atoms. *Rev. Mod. Phys.*, 82:2313–2363, 2010.

[134] M. Viteau, M. G. Bason, J. Radogostowicz, N. Malossi, D. Ciampini, O. Morsch, and E. Arimondo. Rydberg Excitations in Bose-Einstein Condensates in Quasi-One-Dimensional Potentials and Optical Lattices. *Phys. Rev. Lett.*, 107:060402, 2011.

[135] B. Mukherjee, K. Sengupta, and Satya N. Majumdar. Quantum dynamics with stochastic reset. *Phys. Rev. B*, 98:104309, 2018.